TÉCNICO LISBOA

Scaled UAV Prototyping and Control.

João Luís Câmara Ornelas

Thesis to obtain the Master of Science Degree in

Aerospace Engineering

Supervisors: Prof. Fernando José Parracho Lau
Dr. Francisco Fernandes Castro Rego

Examination Committee

Chairperson: Prof. Filipe Szolnoky Ramos Pinto Cunha
Supervisor: Prof. Fernando José Parracho Lau
Member of the Committee: Prof. Pedro Vieira Gamboa

October 2021

”If your regime is not strong enough to handle a joke, then you don’t have a regime.”

Jon Stewart

Acknowledgments

I would like to thank my parents for all the support they have given me. Without them, I would not be able to complete my studies and have as many opportunities in my life.

I want to thank Professor Fernando José Parracho Lau for all the dedication and availability necessary to complete this project and Doctor Francisco Fernandes Castro Rego for all the help given whenever a doubt arose.

Additionally, a huge thank you to the colleagues and friends that have crossed paths on this journey and especially to every person that participated in this project, including Doctor Simão Santos Rodrigues, Doctor Frederico José Prata Rente Reis Afonso, Luís Eusébio and Pedro Pinto.

And finally, a special thank you to the project Flexcraft — Flexible Aircraft (Portugal 2020 funding, reference POCI-01-0247-FEDER-017805 and LISBOA-01-0247-FEDER-017805) for allowing this investigation and study to take place.

Resumo

O projeto Flexcraft em que este trabalho está inserido, visa projetar uma aeronave modular com uma fuselagem removível, numa colaboração entre o Instituto Superior Técnico e várias empresas entre as quais, AlmaDesign, SETsa, Embraer Portugal e a INEGI.

Foi então construído e testado um aeromodelo à escala de um para dez, de modo a averiguar as potenciais vantagens e desvantagens da configuração escolhida e ao mesmo tempo, ganhar mais experiência neste tipo de aeronaves não convencionais.

Adicionalmente, este trabalho propõe a implementação de um sistema de controlo no veículo não tripulado, para isso a configuração do sistema de controlo é desenhado a partir dos parâmetros determinados através de simulação e de medições experimentais. Este processo consiste na modelação da aeronave F02, tendo usado ferramentas como o MATLAB e SIMULINK. O sistema de controlo é também modelado no mesmo software e os ganhos da configuração do controlador são obtidos através de aplicação de técnicas de controlo linear por retroação Proportional–Integral–Derivative (PID) ao modelo linearizado da aeronave e são testados no modelo não linear.

Por fim, um voo foi efetuado para averiguar qual o comportamento do protótipo real, retirar conclusões sobre a viabilidade desta configuração e perceber que trabalho futuro poderá ser efetuado utilizando o protótipo construído como plataforma de testes.

Palavras-chave: Veículo Aéreo Não-Tripulado, Modelação Dinâmica, PID, Projeto de Construção.

Abstract

The Flexcraft project, in which this thesis is included, aims to design a modular aircraft with a removable fuselage, in collaboration between Instituto Superior Técnico and several companies including AlmaDesign, SETsa, Embraer Portugal and INEGI.

A model aircraft was then built and tested with a scale factor of one to ten to investigate the potential advantages and disadvantages of the chosen configuration and gain more experience in this type of non-conventional aircraft configuration.

Additionally, this work proposes implementing a control system in the scaled unmanned aerial vehicle with the tuning of the control system based on parameters determined through simulation and experimental measurements. This process starts with modelling the F02 aircraft using tools such as MATLAB and SIMULINK, then using the same software, the modelling of the control system is also done. Furthermore, the controller gains are obtained by applying PID feedback linear control techniques to the linearised aircraft model and tested on the non-linear model.

Finally, a flight test was performed to measure the behaviour of the actual prototype, to draw conclusions about the feasibility of this configuration and to understand what future work can be done using the prototype built as a test platform.

Keywords: Unmanned Aerial Vehicle, Dynamic Modelling, PID Control, Manufacturing Project.

Contents

List of Tables

List of Figures

Nomenclature

Greek symbols

α	Angle of attack
β	Angle of side-slip
Γ	Wing Dihedral Angle
δ_a	Aileron deflection
δ_e	Elevator deflection
δ_f	Flap deflection
δ_r	Rudder deflection
δ_{Ti}	Rotor i input signal
θ	Pitch angle
Λ	Wing Sweep
λ	Taper ratio
ρ	Density
ϕ	Roll angle
ψ	Yaw Angle
Ω	Rotational Speed of the propeller
ω	Angular velocity

Roman symbols

Re	Reynolds number
C	Coordinates transformation matrix
f	Force vector
I	Inertia matrix

m	Moments vector
p	UAV Position vector
q	Quaternion vector
v	UAV linear velocity vector
A	Horizontal distance between the two vertical wires on the Yaw Inertia Rig
A_f	Frontal Area of the Fuselage
A_{gear}	Frontal Area of the Landing Gear
AB	width of the the front landing gear
AC	Distance between front and rear landing gear
AR	Aspect Ratio of the wing in question
b	Wingspan
C_P	Coefficient of power
C_T	Coefficient of thrust
C_{D_0}	Drag coefficient for α=0
C_{D_q}	Drag coefficient variation with pitch rate
$C_{D0fuselage}$	Drag Coefficient of the Fuselage
C_{D0gear}	Drag Coefficient of the Landing Gear
C_{D_α}	Drag coefficient variation with α
$C_{D_{\delta_e}}$	Drag coefficient variation with elevator deflection
$C_{D_{\delta_f}}$	Drag coefficient variation with flap deflection
C_{L_0}	Lift coefficient for α=0
C_{l_β}	Roll coefficient variation with β
C_{l_p}	Roll coefficient variation with roll rate
C_{L_q}	Lift coefficient variation with pitch rate
C_{l_r}	Roll coefficient variation with yaw rate
C_{L_α}	Lift coefficient variation with α
$C_{l_{\delta_a}}$	Roll coefficient variation with aileron deflection
$C_{L_{\delta_e}}$	Lift coefficient variation with elevator deflection

$C_{L_{\delta_f}}$ Lift coefficient variation with flap deflection

$C_{l_{\delta_r}}$ Roll coefficient variation with rudder deflection

$C_{L_{max}}$ Maximum lift coefficient

C_{m_0} Pitch coefficient for α=0

C_{m_q} Pitch coefficient variation with pitch rate

C_{m_α} Pitch coefficient variation with α

$C_{m_{\delta_e}}$ Pitch coefficient variation with elevator deflection

$C_{m_{\delta_f}}$ Pitch coefficient variation with flap deflection

C_{n_β} Yaw coefficient variation with β

C_{n_p} Yaw coefficient variation with roll rate

C_{n_r} Yaw coefficient variation with yaw rate

$C_{n_{\delta_a}}$ Yaw coefficient variation with aileron deflection

$C_{n_{\delta_r}}$ Yaw coefficient variation with rudder deflection

C_{P_0} Coefficient of power at zero free-stream velocity

C_{P_M} is the Coefficient of Power at $J = J_M$

c_{root} Root Chord

C_{T_0} Coefficient of thrust at zero free-stream velocity

c_{tip} Tip Chord of the wing in question

C_{Y_β} Lateral force coefficient variation with β

C_{Y_p} Lateral force coefficient variation with roll rate

C_{Y_r} Lateral force coefficient variation with yaw rate

$C_{Y_{\delta_a}}$ Lateral force coefficient variation with aileron deflection

$C_{Y_{\delta_r}}$ Lateral force coefficient variation with rudder deflection

CD width of the the rear landing gear

d Propeller's Diameter

Er_i Energy consumed by rotor i

$F_{N1}, F_{N2}, F_{N3}, F_{N4}$ Normal Force exerted in the load cell

g gravity constant

I_{ij} Moment and Products of inertia ($i, j = (x, y, z)$)

J Advance ratio

J_M Advance ratio of zero thrust

L Length of the two vertical wires on the Yaw Inertia Rig separated by a horizontal distance A

l, m, n Moments components

m Aircraft mass

MAC Mean aerodynamic chord

$MTOW$ Maximum Tak-off Weight

N, E, D Position Components in the earth axes

p, q, r Angular Velocity components

q_1, q_2, q_3, q_4 quaternions components

S Wing area

t time or Period

T_i Thrust from rotor i

U, V, W Linear Velocity components

V_T Velocity of trimming

V_{flow} Velocity of the incoming flow

V_{stall} Velocity at Stall

$V_{Takeoff}$ Velocity at Take-off

W' Weight

X_{cm}, Y_{cm}, Z_{cm} Position components of the center of mass

x_{pi}, y_{pi}, z_{pi} Position components of the propeller

Subscripts

a Aerodynamics component

b Body frame

CM Center of mass

E Earth frame

g Gravity component

model	UAV model
p	Propulsion component
struc	Structure of Inertia Rig

Superscripts

b	Body frame
E	Earth frame

Glossary

ESC Electronic Speed Controller.

FRF Frequency Response Function.

GPS Global Positioning System.

IMU Inertial Measurement Unit.

INEGI Instituto de Ciência e Inovação em Engenharia Mecânica e Engenharia Industrial.

IST Instituto Superior Técnico.

MDF Medium-density fibreboard.

MTOW maximum takeoff weight.

NACA National Advisory Committee for Aeronautics.

NASA National Aeronautics and Space Administration.

NED North-East-North.

PID Proportional–Integral–Derivative.

PLA polylactic acid.

PWM Pulse Width Modulation.

RC Radio Control.

RPM Revolutions per minute.

SETsa Sociedade de Engenharia e Transformação S.A.

STOL Short Take Off and Landing.

TECS Total Energy Control System.

UAV Unmanned aerial vehicle.

VLM Vortex lattice method.

VTOL Vertical takeoff and landing airplane.

XPS Extruded polystyrene.

Chapter 1

Introduction

1.1 Motivation

An increased call for more environmentally friendly aircraft, especially in civil aviation, has been on the rise for several years due to the overall impact of the aeronautical sector on climate change, therefore, many companies have started prototyping or designing new greener aircraft [1] [2] [3]. Following this trend, a new aircraft is proposed in this project, with hybrid propulsion and a removable fuselage to allow several missions to be accomplished by the same aircraft [4], thus reducing the number of vehicles needed to be built.

Furthermore, advances in aeronautical engineering have been continually assisted with the development of better analysis and design tools that have been used in the early design stages of a new aircraft [5]. These methods have provided data and understanding of the physical phenomena involved and enabled designers to predict, analyze, and change the characteristics of new vehicles to more suitable and advantageous ones. The creation of extremely powerful digital computers have been one of these tools with the capability of assisting with the design processes and giving the engineer new design insights [5].

One of these tools has been creating extremely powerful digital computer hardware and software capable of assisting with the design processes and giving the engineer new design capabilities [5].

But arguably, one of the most useful tools since the earliest flights, has been testing on a sub-scale model. The first individuals to use this tool were Leonardo da Vinci, George Cayley, and the Wright brothers to better understand and design their flying machines. Models are now frequently used as a key element in new aerospace research and development programs for many applications and roles, including aerodynamic data gathering in wind tunnel investigations, to analyse full-scale aircraft design or proof-of-concept demonstrators for radical aeronautical concepts [5].

Many examples can be found in the works of prestigious agencies, like the National Aeronautics and Space Administration (NASA), when looking into the dynamics and possible advantages or disadvantages of unusual configurations like the use of an oblique wing, figure 1.1(a), or to obtain predictions from dynamic model tests that are then correlated with results from aircraft flight-testing, as in classic

NASA studies of spinning characteristics of general-aviation configurations figure 1.1(b). Moreover, in 2019, Airbus has built a scaled model denominated AlbatrossONE that successfully proved that freely flapping wing-tips could alleviate wing loads and avoid tip stall (Figure 1.1(c)). The final example in this text is the Lockheed Martin X-56, flown in 2013, to research active flutter suppression and gust-load alleviation technologies (Figure1.1(d).

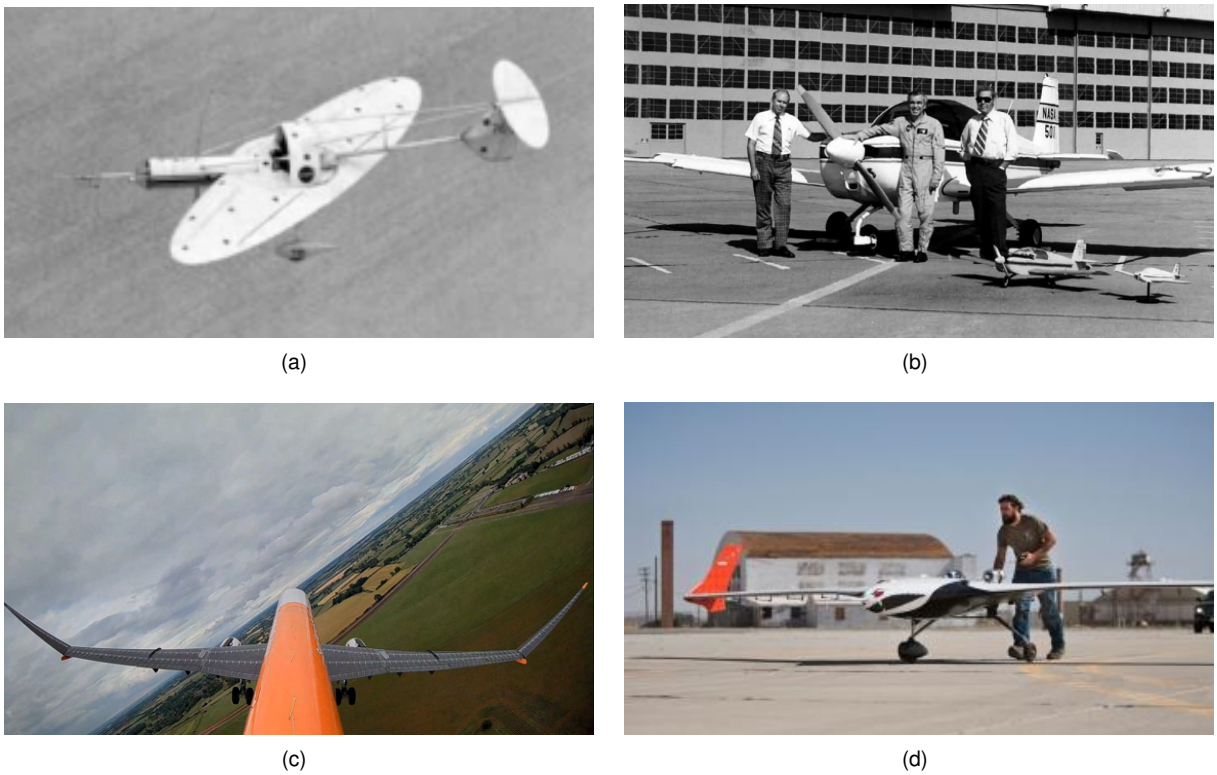

(a) (b)

(c) (d)

Figure 1.1: Scaled models, right to left: (a) Oblique wing research vehicle [5]; (b) scaled models where tests were conducted with, right to left: a spin tunnel model, a radio-controlled model, and the full-scale aircraft [5]; (c) *AlbatrossONE* demonstrator, a small-scale, remote-controlled aircraft demonstrator, which features "semi-aeroelastic" hinged wing-tips [6]; and (d) *Lockheed Martin X-56* intended to research active flutter suppression and gust-load alleviation technologies [7].

With this information in mind, a scaled Unmanned Aerial Vehicle (UAV) is built to be used as a test platform to research the viability of the proposed aircraft by the *Flexcraft* project with an electric propulsion system to emulate its hybrid system. The use of these tools can dramatically reduce risk and cost of the final product, increasing the marketability and safety of new aircraft, especially in the case of new and unusual configurations, such as in this case.

On one hand, these UAV's are flown and navigated by onboard computers that can be operated by a human pilot from different distances depending on the communication structure. On the other hand, an autopilot can be implemented, where the operator on the ground does not fly the UAV but can change the mission plan by sending those changes to the autopilot via a wireless communication link. These two approaches will be attempted since they are proposed for the aircraft.

Finally, we note that improvements in aeromodelling have made these kinds of projects more affordable and accessible to the general public, namely in the area of autopilots, where the price of an embedded system capable of providing this functionality has decreased in several orders of magnitude,

especially with the existing new open-source [1] hardware and software available in the market. For example, the *Pixhawk's* boards used in this project and shown in Figure 1.2, are an inexpensive solution, with the possibility to expand the source code to new control algorithms without the need to build the entire autopilot from scratch, saving time and resources.

Figure 1.2: *Pixhawk* used in the Flexcraft Project.

1.2 Project *Flexcraft*

Beginning in December 2016, the project *Flexcraft*, as part of the framework program *Compete 2020* and financed by *Portugal 2020*, consists of a consortium of various companies and Portuguese institutions (which logos are illustrated in Figure 1.3) to demonstrate the country's capacity for the implementation and development of an innovative system and its future application in the aeronautical sector. The consortium consists of five entities: *AlmaDesign*; *Sociedade de Engenharia e Transformção S.A.* (*SETsa*); *Embraer Portugal - Estruturas em Compósitos S.A.*; Institute of Science and Innovation in Mechanical Engineering and Industrial Engineering (*INEGI*); and *Instituto Superior Técnico* (IST) [8].

Figure 1.3: Entities involved in the Flexcraft project.

In the context of a successful future application of this aircraft in the aeronautical market, a study of macro trends was carried out to solidify the project, as a response: to the congestion of the air space (mainly from airports); to the increase in emissions of polluting gases; to the variations in the oil

[1] Open source is a source code that is made freely available for possible modification and redistribution.

price and an ageing population, the need to develop new aircraft configurations (interior and exterior), including modular/flexible cabins and new propulsion concepts, is emphasised. In this way, enabled with the ability to adapt its configuration, the Flexcraft platform aims to satisfy the fulfilment of different missions, namely:

- Passenger air taxi (between 4 to 6);
- Forest surveillance, supporting rescue operations, surveillance and fire extinguishing;
- Logistic company, with cargo stored in standardised modules;
- Civil protection, for flood scenarios or avalanches;
- Private use, as personal and/or family transport or even as a professional tool in agriculture.

The designation attributed to the aircraft, Flexcraft, as the name implies, aims to represent its adaptability for a wide spectrum of differentiated missions in an expeditious and flexible way. The Flexcraft concept represents a modular utility[2] aircraft that enables the characteristics of a utility aircraft illustrated in Figure 1.4, developed in the *NewFace* project, to provide solutions of flexibility and modularity. The Flexcraft platform aims to compete with the current and future rotorcrafts in the global market. To this end, this aircraft requires greater speed, range and load capacity than conventional helicopters. The various operational requirements that guarantee a smooth and competitive application of Flexcraft in the market are set out below and were studied in [9–12]:

- Transport up to 10 passengers or a total load between 500 and 1500 kg;
- STOL (Short Take-Off and Landing) capability, in order to take off and land on short-runways;
- VTOL (Vertical Take-Off and Landing) capability, in order to increase the versatility of operation for difficult places access, in future iterations of the aircraft;
- Range variation between 500 and 1500 km, depending on the maximum load configuration at maximum range, respectively;
- Endurance of 4 hours;
- Ability of modularity with the detachable wing of the fuselage, allowing the reconfiguration of different cabin modules for different missions;
- Incorporation of a hybrid or, if possible, fully electric propulsion system;
- Subsonic cruising speed set at 400 km/h;
- Maximum speed set at 450 km/h;
- Cruising altitude equal to 8000 feet for passenger transport and 16000 feet for cargo transport;
- External noise constraint generated to a maximum value of 77 dB(A).

[2] A utility aircraft is a general-purpose light aeroplane or helicopter, usually used for transporting people, freight or other supplies, but is also used for other duties when more specialised aircraft are not required or available.

Figure 1.4: *NewFace* aircraft mock-up.

The project is divided into three lines of development which are ”Flight and Operation”, ”Versatility and Usability”, and ”Materials and Production Processes”. These research lines will be validated through three evolutionary demonstrators, namely, with the construction of two UAVs, one on a scale 1 by 10 and one 1 by 15, a scalar mock-up and demonstrators of materials and production processes [9] [10].

This thesis was developed in the scope of the *Flexcraft* project, where the author has been involved in the construction of two scaled models and in the making of three avionics systems, on two 1:10 scaled models (F-01 and F-02) and one 1:15 scaled model. These models are depicted in Figure 1.5.

(a) F-01 (b) F-02 (c) F-03

Figure 1.5: Scaled models, right to left: (a) 1:10 first scaled model (F-01); (b) 1:15 scaled model; and (c) 1:10 second scaled model (F-02).

The main focus of this thesis is on the study, design, control and construction of the 1 by 10 scale models of the original aircraft.

1.3 Objectives

From all this work, this thesis intends to accomplish the following goals:

1. Build and test a scaled model with a scale ratio of 1:10, as a proof of concept of the proposed aircraft.

2. Build a computational model of the scaled model, and estimate or measure the required parameters of the said model as best as possible with the tools available in the institution or build tools to accomplish the same effect.

3. Calculate the gains of a linear controller and test the linear control algorithm.

4. Gain experience in the area of modelling flight as a tool for testing for the analysis of full-scale aircraft design.

1.4 Thesis Outline

This thesis is divided into six major chapters:

- Chapter 1 provides the motivation for this work and its contextualization in the scope of Flexcraft project;
- Chapter 2 describes the aircraft dynamic model;
- Chapter 3 describes the developed linear controller;
- Chapter 4 describes the construction of the UAV models and the implementation of all the avionics and control software needed to make all the necessary tests;
- Chapter 5 presents the experimental tests performed and discusses the obtained results;
- Chapter 6 concludes this work and suggests some directions for further investigation.

Each chapter begins with a brief introduction of the concepts used and a description of the developed work. The appendixes and the online repository [13] provides complementary information to the subjects discussed throughout this text.

Chapter 2

Nonlinear UAV Model

Throughout this chapter, a computational model of the UAV in question is developed to simulate its behaviour and help design its control algorithms. We aim for a model with a low complexity whenever possible, since more complexity implies more coefficients that need to be measured or estimated, with the possibility of not even being able to properly calculate or estimate them due to the lack of proper equipment available.

For this project, the chosen computational tools are MATLAB and SIMULINK. We chose these tools because of previous experience using said software and its simplicity to build complex systems with its graphic interface. The software already includes a predefined package for aircraft modelling (Aerosim and Aerospace), this package offers a generic and very complex model, so to better fit our needs, and avoid unnecessary parameters and better understand the aircraft dynamic equations, the computational model will be build from scratch using simple block diagrams in the SIMULINK environment.

2.1 Introduction

The purpose of this section is to determine the equations that govern the motion of a rigid aircraft, vector analysis of classical mechanics will be used to construct the equations of motion and linear transformations to change to each of the different coordinate systems that exist in this model. This aircraft has four propellers mounted along a trapezoidal wing which provide thrust and whose backward driven flow (otherwise known as slipstream) interacts with the free-stream flow resulting from the aircraft motion, creating aerodynamic forces and moments. The set of available aircraft actuators are:

- Rotors - the aircraft has four propellers, two mounted on each foreside of the wing whose main purpose is to provide thrust.
- Ailerons - that provides roll control by creating a roll moment in the main wing;
- Flaps - provide additional lift to the main wing;
- Rudders - there are two rudders located aft of both the vertical stabilisers and provides lateral control;

- Elevator - it is located aft of the horizontal stabilizer and provides pitch control.

The motors, aerodynamic and gravity forces are all accounted for when describing the vehicle dynamics and kinematics, which are introduced in Sections 2.3 and 2.4. The UAV nonlinear model introduced in these sections represents the following UAV given by Figure 2.2 (F-02) with system state variables $\mathbf{X} \in R^{20}$ and actuators input variables $\mathbf{U} \in R^{8}$. The standard aircraft dynamics nomenclature described in [14] is employed in both state and input variables in table 2.1.

$$\mathbf{X} = [U, V, W, p, q, r, \phi, \theta, \psi, N, E, D, T_1, T_2, T_3, T_4, Er_1, Er_2, Er_3, Er_4]^T \tag{2.1}$$

$$\mathbf{U} = [\delta_e, \delta_f, \delta_a, \delta_r, \delta_{T1}, \delta_{T2}, \delta_{T3}, \delta_{T4}]^T \tag{2.2}$$

Figure 2.1: First UAV prototype built (F-01).

Figure 2.2: Second UAV prototype built (F-02).

Table 2.1: States and Inputs description

Variable	Units	Description
θ	rad	Pitch angle.
ϕ	rad	Roll angle.
ψ	rad	Yaw Angle.
$\mathbf{p} = \begin{bmatrix} N & E & D \end{bmatrix}^T$	m	UAV's Position.
$\mathbf{v} = \begin{bmatrix} U & V & W \end{bmatrix}^T$	m/s	UAV's linear velocity.
$\mathbf{w} = \begin{bmatrix} p & q & r \end{bmatrix}^T$	rad/s	UAV's angular velocity.
δ_a	rad	Aileron deflection.
δ_e	rad	Elevator deflection.
δ_r	rad	Rudder deflection.
δ_f	rad	Flap deflection.
T_i	N	Thrust from rotor i
Er_i	Joule	Energy consumed by rotor i.
δ_{Ti}	-	Motor i input signal.

2.2 Notation

Due to the large number of symbols representing the parameters included in the aircraft model equations, a set of rules is required to improve their clarity. These rules are presented in this section.

- Scalar values or functions are represented by either uppercase and lowercase letters (example: α and A);
- Vectors are represented by boldface lowercase letters (example: **v**);
- Matrices are represented by boldface uppercase letters (example: **I**);
- Derivatives with respect to time will be represented by Newton's notation for differentiation, also called the dot notation (example: $\dot{\theta}$);
- Subscripts are used in two different ways to identify the source of a certain variable; for example, $\mathbf{v}_{CM}$, is the velocity of the center of mass. They can also be used in a variable to indicate in which coordinate frame it is being calculated; for example, $\mathbf{v}_{CM/E}$, is the velocity of the center of mass calculated in relation to the inertial frame NED.
- Superscripts, identify the vector's coordinate frame (example: $\mathbf{v}^b$ is a vector with components described in the body frame).

2.3 Kinematics

Kinematics represents the study of motion, discarding the causes of said motion. A three-dimensional vector then describes the representation of the motion of the rigid body in relation to a given reference frame, and it is necessary to define at least two coordinate references, the inertial frame and the body frame, seen in Figure 2.3.

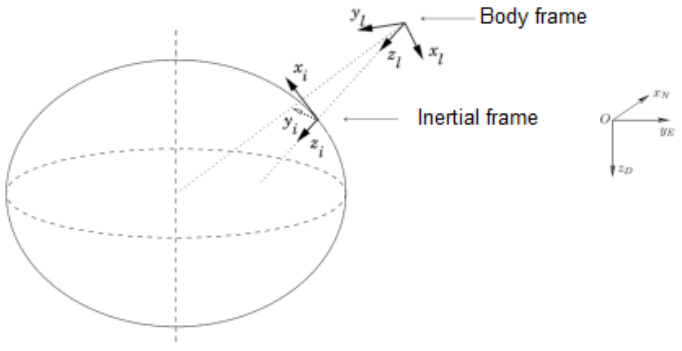

Figure 2.3: Representation of the inertial and body frames.

It was defined as an inertial frame, one where its origin is on the Earth's surface, in the initial position of the body before its motion, this frame is called the North-East-Down (NED) frame, with the x-axis pointing to the North, the y-axis to the East, and the z to the interior of the Earth (Down). It is worth noting that we can assume this is an inertial reference because the solid body has a maximum speed well below the Earth's rotational speed, the same can not be ignored for long duration or high-velocity flights.

The body frame normally used for this type of vehicle has the x-axis pointing forward in relation to the vehicle, aligned with its plane of symmetry. The y-axis is perpendicular to it, pointing to the right side of the vehicle. Finally, the z-axis points downward to satisfy the right-hand rule, as seen in Figure 2.4.

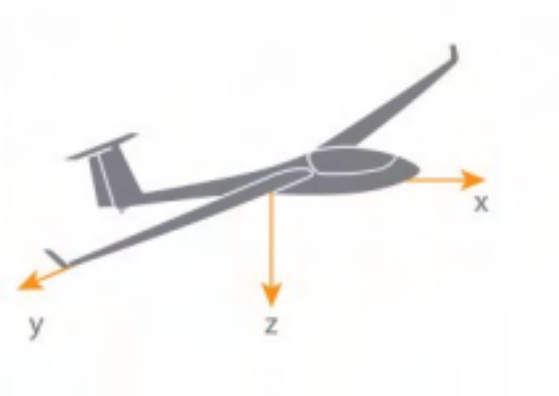

Figure 2.4: Body Frame.

2.3.1 Coordinate system transformation

Since we now have two coordinate systems to use, we need to define a transformation between them. This operation is usually performed using Euler or Quaternion angles. Using Euler angles, this operation is described with three successive rotations, represented by each Euler angle. Mathematically, the NED to body coordinate system is transformed through the following matrix multiplication:

$$\mathbf{u}^b = \mathbf{C}_{bE}\mathbf{u}^E \tag{2.3}$$

Where:

- $\mathbf{u}^b$, a generic three-dimensional vector in the body frame.
- $\mathbf{u}^E$, a generic three-dimensional vector, in the NED frame.
- $\mathbf{C}_{bE}$, the rotation matrix of the NED frame to the body frame.

The matrix will be described in the following equation where *c*, *s* and *t*, represent cosine, sine and tangent function, respectively. In addition, the order in which the rotations are performed, is first with a yaw rotation (around the z-axis), followed by a pitch rotation (around the y-axis), and lastly by a roll rotation (around the x-axis):

$$\mathbf{C}_{bE} = \mathbf{C}(\phi)\mathbf{C}(\theta)\mathbf{C}(\psi) = \begin{bmatrix} c\theta c\psi & c\theta s\psi & -s\theta \\ (-c\phi s\psi + s\phi s\theta c\psi) & (c\phi c\psi + s\phi s\theta s\psi) & s\phi c\theta \\ (s\phi s\psi + c\phi s\theta c\psi) & (-s\phi c\psi + c\phi s\theta s\psi) & c\phi c\theta \end{bmatrix} \tag{2.4}$$

The rotation matrix from the body coordinate system to the NED frame will be the inverse matrix of $\mathbf{C}_{bE}$, called $\mathbf{C}_{Eb}$. Furthermore, in the simulation, the evolution of Euler angles over time will be calculated

by integrating their respective derivatives, which are calculated using the following equation 2.5, where *p*, *q* and *r* are the respective angular velocities in the body axis.

$$\begin{bmatrix} \dot{\phi} \\ \dot{\theta} \\ \dot{\psi} \end{bmatrix} = \begin{bmatrix} 1 & t\theta s\phi & t\theta c\phi \\ 0 & c\phi & -s\phi \\ 0 & s\phi/c\theta & c\phi/c\theta \end{bmatrix} \begin{bmatrix} p \\ q \\ r \end{bmatrix} \tag{2.5}$$

It should be noted that this method includes a discontinuity when the value of θ equals $\pi/2$. Hence for simulation calculations, it will be more robust to use quaternions. Quaternions represent a rotation around a vector to represent the change in coordinate systems. This method does not present any discontinuity but is less intuitive. Still, like Euler's angles, the rotation operations on the components of a generic vector are performed through matrix operations, and that is why we were able to obtain a matrix $\mathbf{C}_{bE}$:

$$\mathbf{C}_{bE} = \begin{bmatrix} (q_0^2 + q_1^2 - q_2^2 - q_3^2) & 2(q_1q_2 + q_0q_3) & 2(q_1q_3 - q_0q_2) \\ 2(q_1q_2 - q_0q_3) & (q_0^2 - q_1^2 + q_2^2 - q_3^2) & 2(q_2q_3 + q_0q_1) \\ 2(q_1q_3 + q_0q_2) & 2(q_2q_3 - q_0q_1) & (q_0^2 - q_1^2 - q_2^2 + q_3^2) \end{bmatrix} \tag{2.6}$$

It should be noted that the quaternions will be used in the non-linear model simulation. Still, in the linearized model used for linear control, we will use Euler angles due to their extensive use in control theory. Since this kind of control only works close to the linearization point, this discontinuity will not be a problem.

In addition, due to its easier interpretation, it will be useful to use the relationship between the quaternions and Euler angles in equation 2.7 and 2.8 for visualisation and initialisation of quaternions values through Euler angles:

$$\begin{bmatrix} q_0 \\ q_1 \\ q_2 \\ q_3 \end{bmatrix} = \begin{bmatrix} (c\frac{\phi}{2}c\frac{\theta}{2}c\frac{\psi}{2} + s\frac{\phi}{2}s\frac{\theta}{2}s\frac{\psi}{2}) \\ (s\frac{\phi}{2}c\frac{\theta}{2}c\frac{\psi}{2} + c\frac{\phi}{2}s\frac{\theta}{2}s\frac{\psi}{2}) \\ (c\frac{\phi}{2}s\frac{\theta}{2}c\frac{\psi}{2} + s\frac{\phi}{2}c\frac{\theta}{2}s\frac{\psi}{2}) \\ (c\frac{\phi}{2}c\frac{\theta}{2}s\frac{\psi}{2} + s\frac{\phi}{2}s\frac{\theta}{2}c\frac{\psi}{2}) \end{bmatrix} \tag{2.7}$$

$$\begin{bmatrix} \phi \\ \theta \\ \psi \end{bmatrix} = \begin{bmatrix} atan2(\frac{2(q_0q_1+q_2q_3)}{1-2(q_1^2+q_2^2)}) \\ asin(2(q_0q_2 - q_3q_1)) \\ atan2(\frac{2(q_0q_3+q_1q_2)}{1-2(q_2^2+q_3^2)}) \end{bmatrix} \tag{2.8}$$

Finally, when using quaternions, we will have to update its values through the integration of their derivatives that are obtained from the angular velocities measured in the aircraft body reference, using the following expression 2.9:

$$\dot{\mathbf{q}} = H(w_{CM/E}^b)\mathbf{q} \tag{2.9}$$

which corresponds to the following expression in expanded form in equation 2.10:

$$\begin{bmatrix} \dot{q_0} \\ \dot{q_1} \\ \dot{q_2} \\ \dot{q_3} \end{bmatrix} = \frac{1}{2} \begin{bmatrix} 0 & -p & -q & -r \\ p & 0 & r & -q \\ q & -r & 0 & p \\ r & q & -p & 0 \end{bmatrix} \begin{bmatrix} q_0 \\ q_1 \\ q_2 \\ q_3 \end{bmatrix} \tag{2.10}$$

2.3.2 Navigation

With the rotations between frames already described in the previous subsection, we can now proceed to formulate the equations that govern the aircraft position in the NED framework, which will allow us to carry out Navigation between reference points using equation 2.11.
To obtain the position of the center of mass, we will integrate the aircraft's speed after converting its components into the NED frame. Hence we get the following expression:

$$\mathbf{p}_{CM}^{E} = \int \mathbf{C}_{Eb} \mathbf{v}_{CM/E}^{b} \tag{2.11}$$

where $\mathbf{v}_{CM/E}^{b}$ is the speed of the center of mass in relation to the NED frame with components described in the body frame. Finally, it is important to include the speed of the incoming flow and wind and its relationship with the body's ground speed:

$$\mathbf{v}_{CM/E}^{b} = \mathbf{v}_{rel/E}^{b} + \mathbf{C}_{bE} \mathbf{v}_{wind/E}^{E} \tag{2.12}$$

where $\mathbf{v}_{rel/E}^{b}$ the speed of the flow relative to the vehicle and $\mathbf{v}_{wind/E}^{E}$ the wind speed in relation to the NED frame with components described in the NED frame. If there is no wind, the airspeed will be equal to the aircraft speed in the body frame. It should also be noted that the wind will be positive when it is a tailwind and negative when it is a nose wind.

2.4 Dynamics

Using classical mechanics, the dynamics of the aircraft can be represented using a model of six degrees of freedom from the following vector equations, assuming that the NED frame is an inertial frame:

$$\dot{\mathbf{v}}_{CM/E}^{b} = \frac{\mathbf{f}_{T}^{b}}{m} - \mathbf{w}_{CM/E}^{b} \times \mathbf{v}_{CM/E}^{b} \tag{2.13}$$

$$\dot{\mathbf{w}}_{CM/E}^{b} = (\mathbf{I}^{b})^{-1} [\mathbf{m}_{T}^{b} - \mathbf{w}_{CM/E}^{b} \times \mathbf{I}^{b} \mathbf{w}_{CM/E}^{b}] \tag{2.14}$$

where:

- $\mathbf{v}_{CM/E}^{b}$, the aircraft's speed in relation to the NED frame in the body frame
- $\dot{\mathbf{v}}_{CM/E}^{b}$, the aircraft's acceleration relative to the NED frame in the body frame

- m, the total mass of the aircraft.
- $\mathbf{f}_T^b$, the total contribution of all forces acting on this vehicle, whether gravity, aerodynamic or propulsion forces. These forces will be explored in future sections.
- $\mathbf{m}_T^b$, the total contribution of all moments that act in this vehicle, whether aerodynamic or from propulsion moments. These moments will be explored in future sections.
- $\mathbf{w}_{CM/E}^b$, angular speed of the aircraft body frame in the body frame.
- $\dot{\mathbf{w}}_{CM/E}^b$, angular acceleration of the aircraft body frame in the body frame.
- $\mathbf{I} = \begin{bmatrix} I_{xx} & I_{xy} & I_{xz} \\ I_{yx} & I_{yy} & I_{yz} \\ I_{zx} & I_{zy} & I_{zz} \end{bmatrix}$, the vehicle's inertia matrix, which will be measured experimentally.

The propulsion loads, aerodynamic loads and gravity produce the forces and moments which affect the aircraft's behaviour and are described by the equations 2.15 and 2.16:

$$\mathbf{f}_T^b = \mathbf{f}_g^b + \mathbf{f}_p^b + \mathbf{f}_a^b \tag{2.15}$$

$$\mathbf{m}_T^b = \mathbf{m}_p^b + \mathbf{m}_a^b + \mathbf{m}_g^b \tag{2.16}$$

The subscripts *g*, *p* and *a* stand for gravity, propulsion and aerodynamic forces or moments, respectively, which are discussed in the following subsections.

Inertia data

In table 2.2 a list of the main parameters for the dynamics portion of this model is listed. In section 5.1 and 5.2 more information about the estimation of these parameters is provided. The position of the center of mass is measured in relation to the point of intersection between the plane of symmetry of the UAV and the leading edge of the wing.

Table 2.2: Summary of the inertia parameters necessary for the 6 degree of freedom dynamics model.

Inertia Parameters F-02							
UAV without fuselage				UAV with fuselage			
$I_{xx}[kgm^2]$	0.782	$m[kg]$	6.409	$I_{xx}[kgm^2]$	0.798	$m[kg]$	7.435
$I_{yy}[kgm^2]$	0.218	$g[m/s^2]$	9.806	$I_{yy}[kgm^2]$	0.307	$g[m/s^2]$	9.806
$I_{zz}[kgm^2]$	1.070	$X_{cm}[m]$	-0.094	$I_{zz}[kgm^2]$	1.107	$X_{cm}[m]$	-0.089
$I_{xy} = I_{yx}[kgm^2]$	0.000	$Y_{cm}[m]$	0.000	$I_{xy} = I_{yx}[kgm^2]$	0.000	$Y_{cm}[m]$	0.000
$I_{xz} = I_{zx}[kgm^2]$	0.024	$Z_{cm}[m]$	0.003	$I_{xz} = I_{zx}[kgm^2]$	0.275	$Z_{cm}[m]$	0.016
$I_{yz} = I_{zy}[kgm^2]$	0.000			$I_{yz} = I_{zy}[kgm^2]$	0.000		

2.4.1 Gravity

In this section we will expand the term $\mathbf{f}_g^b$ of equation 2.15 and $\mathbf{m}_g^b$ of equation 2.16. We first have to define the center of mass, which is the point at which the distribution of mass is equal in all directions,

and does not depend on the gravitational field. And the center of gravity, which is the point at which the distribution of weight is equal in all directions, and so does depend on the gravitational field. For applications such as UAV motion control the gravitational field can be assumed to be uniform and so the center of gravity and mass are located in the same point leading to $\mathbf{m}_g$ equal to zero.

The force $\mathbf{f}_g$ can be easily defined in the NED coordinate frame with only a z component equal to the gravity constant of the earth at its surface times the mass of the object in question as defined in equation 2.17. The gravity force can then be described in the body frame using the transformation matrices defined in subsection 2.3, and so we finally get equation 2.18.

$$\mathbf{f}_g^E = \begin{bmatrix} 0 & 0 & mg \end{bmatrix}^T \tag{2.17}$$

$$\mathbf{f}_g^b = \mathbf{C}_{bE}\mathbf{f}_g^E \tag{2.18}$$

2.4.2 Propulsion

This section will address the model of the aircraft's propulsion, which includes four electric rotors (four motors + four propellers) that are powered by four batteries due to physical constraints. The propeller and motors used are in the following Figures 2.5 2.6.

Figure 2.5: Carbon Propeller 13x8.

Figure 2.6: Brushless motor Turnigy outrunner d3548/4.

Furthermore, the motors are brushless electric motors that need to be controlled by an Electronic Speed Controller (ESC), which sends the appropriate modulated signal to the motors and receive a signal, in this case from the Pixhawk autopilot board, that will translate it into a certain rotational speed. Additionally, the rotational speed will also vary depending on the incoming airflow since these ESC's do not have a rotation speed feedback loop that can correct their speed in relation to the effects caused by the incoming airflow. The ESC used can be seen in Figure 2.7.

Figure 2.7: Electronic Speed Controllers (ESC) Hobbywing-SkyWalker-60UBEC.

For each rotor we will model a static response from the propeller model and a first order response to model the transient response of the electric motor; these models will have δ_{Ti} as an input and T_i, M_i and P_i as outputs.

Static forces and moments created by the propeller

A propeller is a device with a rotating hub and radiating blades set at a pitch to form a helical spiral. It transforms rotational power into linear thrust by acting upon a fluid, such as air in this case. A given mass of the working fluid is accelerated in one direction and the aircraft moves in the opposite direction. In more advanced systems, the pitch can be changed at different flight conditions maximising efficiency, which is not the case for this or most small UAV's.

The most common way to model a propeller is to define its behaviour using the Coefficient of Thrust (C_T) and Coefficient of Power (C_p) which depend on the propeller geometry, Reynolds number (Re) and Advance Ratio (J), using the following equations 2.19, 2.20 and 2.21 [15]:

$$C_T = C_T(Re, J, shape), \tag{2.19}$$

$$C_P = C_P(Re, J, shape), \tag{2.20}$$

$$J = \frac{u}{\Omega d} \tag{2.21}$$

where:

- u, the free-stream velocity normal to the propeller's plane(yOz in the body frame),
- Ω, propeller's rotation speed,
- d, propeller's diameter.

Following the approximation described in [15], the influence of the Reynolds Number will be neglected, in order to simplify this complex behaviour and we get the following equation for C_T and C_P:

$$C_T = C_{T_0}\left(1 - \frac{J}{J_M}\right) \tag{2.22}$$

$$C_P = C_{P_0} + \left(\frac{J}{J_M}\right)^2 (C_{P_M} - C_{P_0}) \tag{2.23}$$

Where:

- C_{T_0}, is the Coefficient of Thrust at zero free-stream velocity.
- C_{P_0}, is the Coefficient of Power at zero free-stream velocity.
- J_M, is the advance ratio of zero thrust.
- C_{P_M} is the Coefficient of Power at $J = J_M$.

With these coefficients defined, we can model the thrust, power and moments created by each rotor with the following equations, with ρ being the atmospheric density.

$$T = \rho\Omega^2 d^4 C_T(J) \tag{2.24}$$

$$P = \rho\Omega^3 d^5 C_P(J) \tag{2.25}$$

$$M = \pm\frac{\rho\Omega^2 d^5 C_P(J)}{2\pi} \tag{2.26}$$

With this model, we use the data retrieved from the propulsion tests described in section 5.3, and by fitting the equations that represent the Thrust and Power Coefficients that characterise this model to the data, we get the results in the following Figure 2.8.

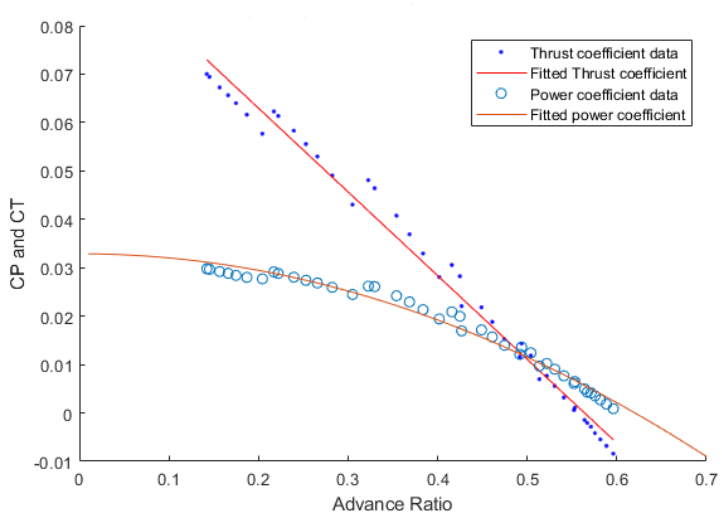

Figure 2.8: Thrust and power coefficient versus advance ratio for 13x6 propeller

While this model does provide a good approximation for the output of the propeller, we can not set with precision the rotational speed of the propeller since the only input we can manipulate is the Pulse Width Modulation (PWM) signal that the ESC receives, which will make the propeller rotate at different speeds depending on the incoming airflow.

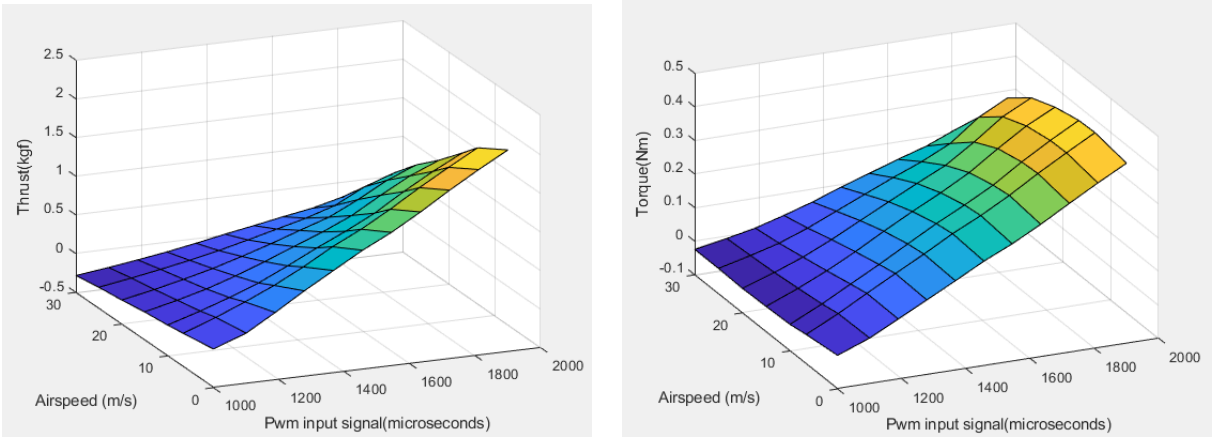

(a) (b)

Figure 2.9: Measured Rotor Static Response (a) Static Thrust and (b) Static Torque of the propeller 13x8.

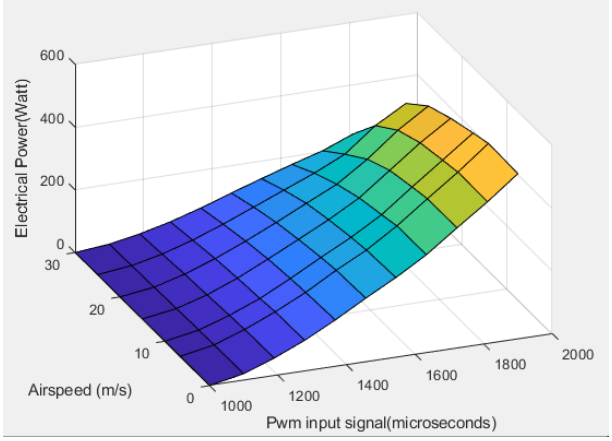

Figure 2.10: Measured Static Electrical Power of the propeller 13x8

So we propose a data-driven model instead, by fitting the data to a model with two inputs, the incoming airflow (u) and the rotational speed of the propeller (Ω). The fitting will be done using a lookup table with a linear interpolation between points for the thrust parameter and quadratic interpolations between points for the torque and electrical power parameters. This approach results on the graphs in Figures 2.9 (a), 2.9 (b) and 2.10, for the propeller with a diameter of 13 inches with a pitch of 8 inches per single revolution of the engine. This kind of model makes it harder to manipulate mathematically but in this case provides more accurate results. In Appendix A.3, it is possible to observe the data for all propellers tested.

Transient Response

For the Transient Response it is assumed an instantaneous response of torque and electrical power since its response is faster than the aircraft dynamics. Since the thrust depends directly on the rotor speed and does not change as fast as the torque and electrical power, we approximate the motor thrust transient response by a first order system with a certain time constant and a delay:

$$G(s) = \frac{Y(s)}{U(s)} = \frac{K}{K_T s + 1} e^{-t_d s} \tag{2.27}$$

which will correspond in the time domain to the following equation:

$$\dot{T}(t) = \frac{K T_i (t - t_d) - T(t)}{K_T} \tag{2.28}$$

where T is the Thrust and T_i is the steady-state value of the Thrust for a certain PWM input and incoming airflow (u), given by the propeller model, which serves as the input for the first order model. See section 5.3 for more information about how these values were measured, assumptions made and conclusions obtained from the propulsion tests.

Table 2.3: Final Models of the Time Response of the Rotor output

Thrust Model		Torque Model		Electrical Power Model	
Pole	-12.81	Pole	-	Pole	-
Time Constant	0.078	Time Constant	-	Time Constant	-
Static Gain	1	Static Gain	1	Static Gain	1
delay	0.0576 s	delay	0	delay	0

Forces and moments represented in the center of mass

Having calculated the individual forces and moments from each rotor produced at the propeller, now we need to translate them into the center of mass. To accomplish this task, we first measure their locations in relation to the same reference point as the center of mass, which corresponds to the point of intersection between the plane of symmetry of the UAV and the leading edge, resulting in Table 2.4

Table 2.4: Static response error

Rotor location related to reference point							
Rotor 1		Rotor 2		Rotor 3		Rotor 4	
$x_{p1}[m]$	0.132	$x_{p2}[m]$	0.132	$x_{p3}[m]$	0.132	$x_{p4}[m]$	0.132
$y_{p1}[m]$	0.750	$y_{p2}[m]$	0.200	$y_{p3}[m]$	-0.200	$y_{p4}[m]$	-0.750
$z_{p1}[m]$	0.000	$z_{p2}[m]$	0.000	$z_{p3}[m]$	0.000	$z_{p4}[m]$	0.000

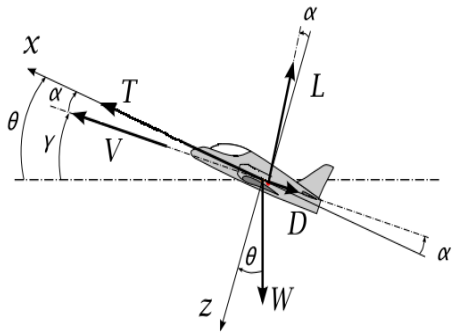

Figure 2.11: Representation of the body frame and forces in xOz plane

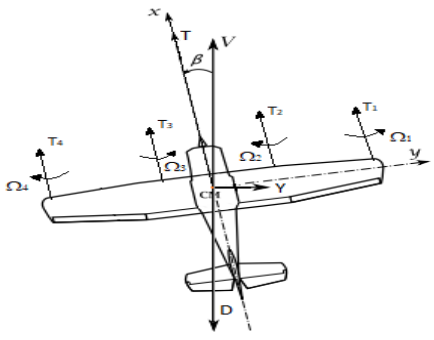

Figure 2.12: Representation of the body frame and forces in xOy

As represented in figures 2.11, 2.12, one can translate the forces and moments resulting from the action of the four rotors to the body coordinate system origin at the center of mass by using the following expressions:

$$\mathbf{m}_p = \begin{bmatrix} -M_1 + M_2 - M_3 + M_4 \\ (T_1 + T_2 + T_3 + T_4) z_p \\ (T_3 y_{p3} + T_4 y_{p4}) - (T_1 y_{p1} + T_2 y_{p2}) \end{bmatrix} \tag{2.29}$$

$$\mathbf{f}_p = \begin{bmatrix} (T_1 + T_2 + T_3 + T_4) \\ 0 \\ 0 \end{bmatrix} \tag{2.30}$$

We have to note that we assume that all the four rotors are colinear with the x-axis in this UAV.

2.4.3 Aerodynamics

This section will address one of the most important models and usually the hardest, with great importance to achieve a reliable model. The work presented in this section is based on [16] and [14], as a reference. First of all, to correctly represent aerodynamic forces and moments, two axes and two angles will have to be established to be used to describe these forces as a function of these variables, α and β.

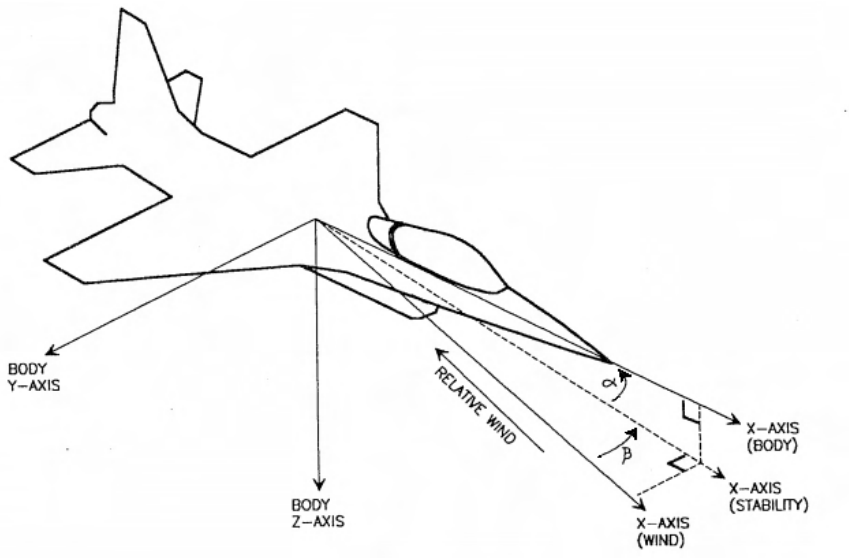

Figure 2.13: Definition of aerodynamics's axis and angles.

In Figure 2.13, an aircraft with a flow with a relative direction off-center with the body axis is represented. The approximation flow vector is the same but in the opposite direction to the velocity vector $\mathbf{v}^b_{rel/E}$ used in the equations of motion. The skid (β) and attack angles (α) are then obtained by rotating around x and z so that the x-axis is aligned with the defined body axis.

The first rotation defines the stability axis and with the second rotation, we find the body axis. Therefore, we define the angle of attack as the angle between the body's x-axis and the stability x-axis and

the skid angle, the angle between the wind axis and the stability axis. It should be noted that the skid is positive when the rotation on the body axis is negative, as can be seen in the figure 2.13.

As previously performed, the rotation matrices between the axes mentioned are defined as:

$$\begin{bmatrix} x \\ y \\ z \end{bmatrix}_{stab} = \begin{bmatrix} c(\beta) & -s(\beta) & 0 \\ s(\beta) & c(\beta) & 0 \\ 0 & 0 & 1 \end{bmatrix} \begin{bmatrix} x \\ y \\ z \end{bmatrix}_{wind} \tag{2.31}$$

$$\begin{bmatrix} x \\ y \\ z \end{bmatrix}_{body} = \begin{bmatrix} c(\alpha) & 0 & -s(\alpha) \\ 0 & 1 & 0 \\ s(\alpha) & 0 & c(\alpha) \end{bmatrix} \begin{bmatrix} x \\ y \\ z \end{bmatrix}_{stab} \tag{2.32}$$

$$\mathbf{C}_{bw} = \mathbf{C}_{bs}\mathbf{C}_{sw} = \begin{bmatrix} c(\alpha)c(\beta) & -c(\alpha)s(\beta) & -s(\alpha) \\ s(\beta) & c(\beta) & 0 \\ s(\alpha)c(\beta) & -s(\alpha)s(\beta) & c(\alpha) \end{bmatrix} \tag{2.33}$$

These concepts will be used to obtain the equations that describe the aerodynamic forces and moments. To obtain these variables, we assume that the components of the relative velocity of the airflow are defined as, $\mathbf{v}_{rel/E} = [U \quad V \quad W]$, in the body frame:

$$tan(\alpha) = \frac{W}{U} \tag{2.34}$$

$$sin(\beta) = \frac{V}{|\mathbf{v}_{rel/E}|} \tag{2.35}$$

$$|\mathbf{v}_{rel/E}| = \sqrt{U^2 + V^2 + W^2} = V_{flow} \tag{2.36}$$

It should be noted that it is often difficult to measure all the flow components, especially with the presence of wind and turbulence.

We can now define a function for the aerodynamic forces that are represented in figures 2.14 and 2.15, but since the lift, drag and lateral forces are defined in the wind axis, we need to make a conversion from equation 2.37 to the body frame since it is in this axis that the dynamics of the aircraft is calculated and so, using the rotation matrix in the expression 2.33, we achieve the desired result in the equation 2.38.

$$\mathbf{f}_A^w = [-Drag \quad YForce \quad -Lift]^T \tag{2.37}$$

$$\mathbf{f}_A^b = \mathbf{C}_{bw}\mathbf{f}_A^w \tag{2.38}$$

These forces are functions of α, β, the deflections of the control surfaces, but also on the Mach and Reynolds numbers, since the aircraft will fly at very low Mach numbers, its influence will be assumed to

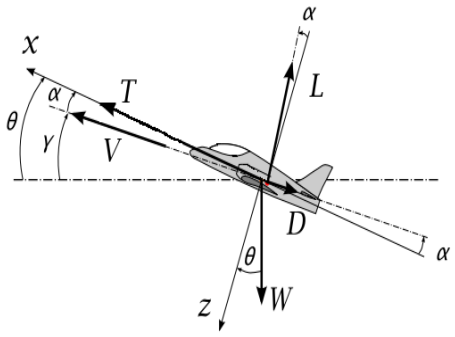

Figure 2.14: Representation of the aerodynamic forces and angles in a side view

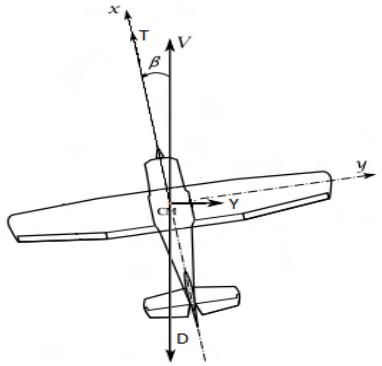

Figure 2.15: Representation of the aerodynamic forces and angles in a top view

be negligible. On the other hand, the Reynolds number will depend on the flight condition assuming an operation between 15 m/s and 30 m/s corresponding to a Reynolds number around 340000 and 680000 (assuming air at room temperature of $20°$).

In addition, the aircraft has a flexible structure that can be deformed, changing its aerodynamic behaviour. However, in the interest of simplifying the computational model, it will not be counted as it should be a small contribution to the missions that will be carried out [17].

Additionally, these forces are defined according to their dimensionless aerodynamic coefficients. These aerodynamic coefficients are a function of the previous variables and the nondimensionalization is done using the dynamic pressure and a characteristic length of the aircraft depending on the force in question.

To take some complexity out of the problem, we will assume that the aircraft works in the linear region of the curves that describe the coefficients as a function of the aerodynamic angles, resulting in aerodynamic derivatives. This simplification can be done with a reduced error for small angles. In this way, we obtain the following equations:

$$Lift = \left(C_{L_0} + C_{L_\alpha}\alpha + C_{L_q}Q\frac{c}{2V_{flow}} + C_{L_{\delta_e}}\delta_e + C_{L_{\delta_f}}\delta_f\right)\frac{\rho V_{flow}^2 S}{2} \tag{2.39}$$

$$Drag = \left(C_{D_0} + C_{D_\alpha}\alpha + C_{D_q}Q\frac{c}{2V_{flow}} + C_{D_{\delta_e}}\delta_e + C_{D_{\delta_f}}\delta_f\right)\frac{\rho V_{flow}^2 S}{2} \tag{2.40}$$

$$YForce = \left(C_{Y_\beta}\beta + (C_{Y_p}P + C_{Y_r}R)\frac{b}{2V_{flow}} + C_{Y_{\delta_a}}\delta_a + C_{Y_{\delta_r}}\delta_r\right)\frac{\rho V_{flow}^2 S}{2} \tag{2.41}$$

The aerodynamic moments are defined in the body axes and are positive according to the right hand rule:

$$M_A^b = [l \quad m \quad n]^T \tag{2.42}$$

As in the case of the aerodynamic forces, the aerodynamic moments are written as a function of dimensionless aerodynamic coefficients, depending on the same variables and using the same as-

sumptions. We thus obtain the following expressions:

$$l = \left(C_{l_\beta}\beta + (C_{l_p}P + C_{l_r}R)\frac{b}{2V_{flow}} + C_{l_{\delta_a}}\delta_a + C_{l_{\delta_r}}\delta_r\right)\frac{\rho V_{flow}^2 Sb}{2} \tag{2.43}$$

$$m = \left(C_{m_0} + C_{m_\alpha}\alpha + (C_{m_q}Q)\frac{\bar{c}}{2V_{flow}} + C_{m_{\delta_e}}\delta_e + C_{m_{\delta_f}}\delta f\right)\frac{\rho V_{flow}^2 S\bar{c}}{2} \tag{2.44}$$

$$n = \left(C_{n_\beta}\beta + (C_{n_p}P + C_{n_r}R)\frac{b}{2V_{flow}} + C_{n_{\delta_a}}\delta_a + C_{n_{\delta_r}}\delta_r\right)\frac{\rho V_{flow}^2 Sb}{2} \tag{2.45}$$

Aerodynamic Data Estimation

Due to difficulties and the lack of equipment to directly measure all the necessary aerodynamics parameters in the UAV prototypes, we need to estimate them using computational tools, in this case the $XFLR5$ software. $XFLR5$ is a program developed by André Deperrois based on the "classical" Vortex lattice method (VLM) analysis that assumes a purely inviscid flow around lifting bodies; it is therefore unrealistic for the Reynolds numbers used by the model aircraft and so must be complemented with a viscid analysis by postulating that the viscous and inviscid contributions to aerodynamic forces are linearly independent, so that an inviscid VLM output may be complemented by a viscous XFoil analysis to get a more realistic mathematical model. This assumption is not supported by a theoretical model, and so XFLR5 results need to be considered preliminary and experimental; nevertheless it has shown promise and some precision especially for longitudinal variables and slow periodic modes [18] [19].

XFLR5 makes use of both a geometrical model of the lifting surfaces to be analysed in Figure 2.16 and a set of polars derived from viscous analysis of the adopted airfoils in Figures 2.17, 2.18 and 2.19 , for a range of Reynolds numbers and lift coefficients broad enough to cover all flying conditions.

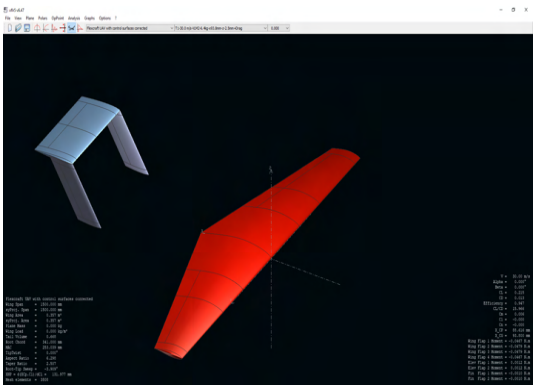

Figure 2.16: Aircraft geometrical aerodynamic model.

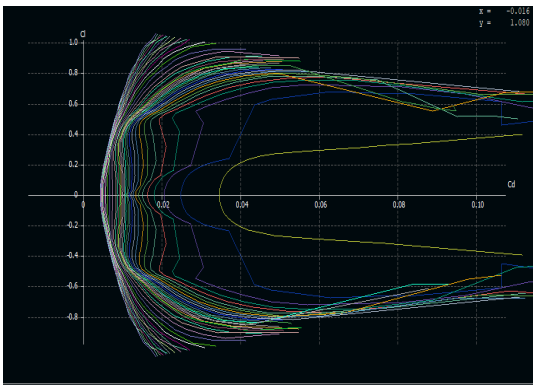

Figure 2.17: Polar diagram for the NACA0009 airfoil.

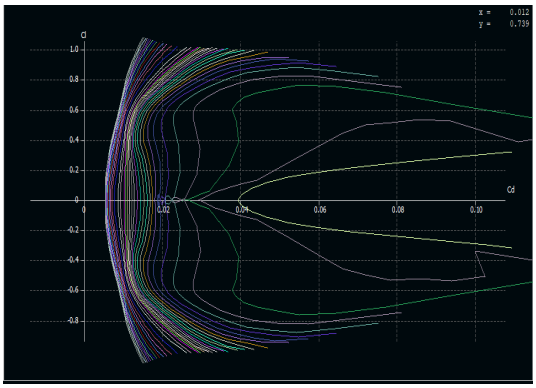

Figure 2.18: Polar diagram for the NACA0012 airfoil.

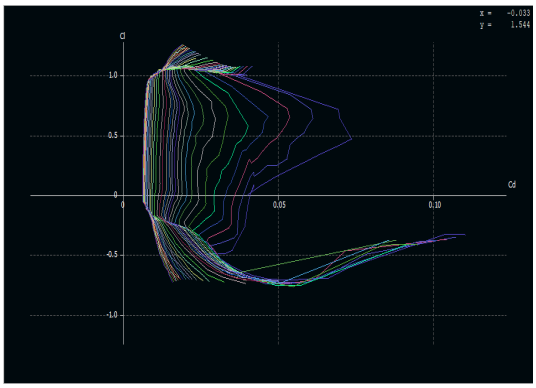

Figure 2.19: Polar diagram for the NACA64a415 airfoil.

To make use of this software we first need to gather all the geometric dimensions of the proposed aircraft by scaling by a factor of 1:10; all the aforementioned values can be seen in table 2.5:

Table 2.5: Scaled dimensions for the UAV with a scaled factor of 1:10.

	Main Wing		**Horizontal Stabiliser**		**Vertical Stabiliser**	
	Original	1:10	Original	1:10	Original	1:10
Wing Surface S [m^2]	35.800	0.358	7.440	0.074	2.280	0.023
Wingspan b [m]	15.000	1.500	4.000	0.400	2.000	0.200
Aspect Ratio AR[-]	6.300	6.300	2.150	2.150	1.760	1.760
Dihedral Angle Γ [º]	0.000	0.000	0.000	0.000	0.000	0.000
Sweep Λ [º]	0.000	0.000	0.000	0.000	35.000	35.000
Root Chord [m]	3.410	0.341	1.86	0.186	1.140	0.114
Tip Chord [m]	1.360	0.136	1.86	0.186	1.140	0.114
Taper Ratio λ[-]	0.400	0.400	1.000	1.000	1.000	10.000
MAC [m]	2.53	0.253	1.860	0.186	1.140	0.114

In addition to the dimensional parameters referred in 2.5, it is important to state some adimensional variables important to characterise the shape of the wing and tails of the aircraft, such as the MAC (Mean Aerodynamic Chord), which can be obtained by equation 2.46, the taper ratio (λ), which is the ratio between the chord of the tip of the wing and the chord at the root of the said wing, as observed in equation 2.48, the aspect ratio (AR), which is calculated by dividing the wingspan squared by the wing's surface in equation 2.47, which plays a direct influence on the performance and aircraft stability, the dihedral angle (Γ), the upward angle from horizontal of the wings of a fixed-wing aircraft and finally the sweep (Λ) corresponding to the angle formed by the leading edge in relation to the central axis of the aircraft, influencing the aerodynamic performance through the reduction of effective wing speed.

$$MAC = \frac{2}{3} c_{root} \left(\frac{1 + \lambda + \lambda^2}{1 + \lambda} \right) \tag{2.46}$$

$$AR = \frac{b^2}{S} \tag{2.47}$$

$$\lambda = \frac{c_{tip}}{c_{root}} \tag{2.48}$$

Having now defined the dimensions of all the lifting surfaces, we will now present the different National Advisory Committee for Aeronautics (NACA) wing airfoils of each lifting surface, in table 2.6, that were previously selected for the original aircraft. On a note, the wing profile of the main wing was chosen due to its thickness maximum thickness of 15% of the chord that allows easier allocation of all the components inside [12]; for the tail stabilisers typical wing profiles of general aviation were chosen [12][20].

Table 2.6: NACA denominations of the several airfoils on the Flexcraft aircraft

Wing	Airfoil
Main Wing	NACA 64A415
Horizontal stabiliser	NACA 0009
Vertical stabiliser	NACA 0012

Furthermore, we need to know where the stabiliser will be located in this configuration and by scaling it from the original designed aircraft, we reach the following distances between the main wing leading edge and the horizontal and vertical stabilisers.

Table 2.7: Vertical and horizontal stabilisers leading edges locations in relation to main wing leading edge

Coordinate	Main Wing	Right Vertical Tail	Left Vertical Tail	Horizontal Tail
X [mm]	0.000	710.500	710.500	850.500
Y [mm]	0.000	200.000	-200.000	0.000
Z [mm]	0.000	0.000	0.000	-209.000

Additionally, control surfaces and high lift devices are present in this modular concept, the Flexcraft aircraft has a total of seven movable surfaces along its wing surfaces, namely two flaps (Figure 2.20, n^{o}1 blue), two flaperons (Figure 2.20, n^{o}2 green), two rudders (Figure 2.20, n^{o}3 red color) and an elevator (Figure 2.20, n^{o}4 yellow color). In addition, in table 2.8, some parameters related to the mobile devices of the control and high lift devices are represented, namely the deflection angles in the stages of runoff, take-off or manoeuvres and the percentage of the wing area and chord [10]. These parameters were established for the original aircraft. However, as the Reynolds numbers are much lower for the scaled model we will try and use smaller deflections whenever is possible. Finnally, a saturation to their deflection speed is imposed to simulate the physical limitations of the servos. In Table 2.8 the corresponding saturation rates for each different control surfaces are presented, since in this case two different servos are used due to physical constraint due to the smaller size of these two airfoils.

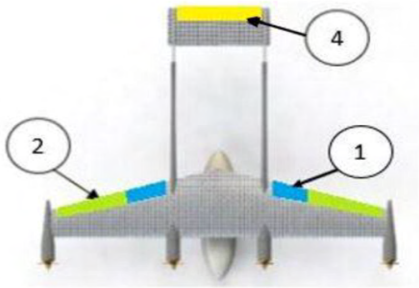

Figure 2.20: Control surfaces, top view

Figure 2.21: Control surfaces, side view

Table 2.8: Control and high lift surfaces dimensions and deflections. ($*$ maximum deflection in maneuvers)

	Flap	**Ailerons/Flaperons**	**Rudders**	**Elevator**
Wing Area $[\%]$	23.0	32.0	44.5	12.5
Hinge Chord $[\%]$	25.0	25.0	35.0	25.0
Max. Deflection at Landing [°]	40.0	40.0	30.0 $*$	30.0 $*$
Max. Deflection at Take-off [°]	35.0	35.0	30.0 $*$	30.0 $*$
Deflection Rate Saturation $[rad/s]$	4.55	4.55	8.72	8.72

Finally, we need a way to add the influence on the aerodynamics from the landing gear and the detachable fuselage. Unfortunately, the XFRL5 does not recommend adding these components directly in the analysis and instead recommends adding them as an extra drag coefficient ($C_{D_{0fus}}$ $C_{D_{0gear}}$) with their respective frontal area.

In the case of the landing gear, equation 2.49 allows us to obtain a rough estimate of the value of the aerodynamic resistance coefficient caused by their presence. The variable A_{gear} corresponding to the frontal area of the landing in table 2.9. On the other hand, the variable S refers to the wing area and the maximum takeoff weight (MTOW) value was arbitrated to 6.4 kg. The value obtained is explicit in table 2.9. As for the fuselage, we can get a drag coefficient from [4]. A summary of values concerning the landing gear and fuselage can be seen in table 2.9. With all the necessary inputs, we can now use $XFRL5$ stability analysis to estimate the aerodynamic coefficients (Table 2.10).

$$C_{D_{0gear}} = 3.23\sqrt{MTOW}\frac{A_{gear}}{S} \tag{2.49}$$

Table 2.9: Fuselage values

Fuselage		Landing Gear (1:10)			
$C_{D_{0fus}}$	A_f $[m^2]$	MTOW $[kg]$	$A_{gear}[m^2]$	S$[m^2]$	$C_{D_{0gear}}$
0.005	0.025	6.409	0.005	0.358	0.114

Table 2.10: Aerodynamics derivatives for the longitudinal and lateral dynamics.

Longitudinal aerodynamics derivatives			Lateral aerodynamics derivatives		
Symbol	Value	Value (with fuselage)	Symbol	Value	Value (with fuselage)
C_{L_0}	0.215	0.215	C_{Y_β}	-0.359	-0.386
C_{L_α}	4.804	4.804	C_{Y_p}	0.000	0.000
C_{L_q}	7.993	8.0577	C_{Y_r}	0.345	0.352
$C_{L_{\delta_e}}$	0.389	0.389	$C_{Y_{\delta_a}}$	0.029	0.029
$C_{L_{\delta_f}}$	0.535	0.538	$C_{Y_{\delta_r}}$	0.198	0.198
C_{D_0}	0.015	0.015	C_{l_β}	-0.040	-0.039
C_{D_α}	0.052	0.052	C_{l_p}	-0.420	-0.420
C_{D_q}	0.000	0.000	C_{l_r}	0.126	0.133
$C_{D_{\delta_e}}$	0.036	0.036	$C_{l_{\delta_a}}$	-0.229	-0.229
$C_{D_{\delta_f}}$	0.0165	0.0165	$C_{l_{\delta_r}}$	0.009	0.011
C_{m_0}	0.007	0.003	C_{n_β}	0.158	0.159
C_{m_α}	-0.741	-0.8634	C_{n_p}	-0.096	-0.096
C_{m_q}	-15.330	-15.538	C_{n_r}	-0.155	-0.1625
$C_{m_{\delta_e}}$	-1.283	-1.292	$C_{n_{\delta_a}}$	-0.014	-0.014
$C_{m_{\delta_f}}$	-0.055	-0.0645	$C_{n_{\delta_r}}$	-0.098	-0.099

2.4.4 Numerical implementation in MATLAB/SIMULINK

Using the MATLAB / SIMULINK environment, we can implement the set of ordinary differential equations obtained in the previous sections, and it is now possible for us to build the nonlinear model of the aircraft to be used within the scope of this work, with the following block diagrams:

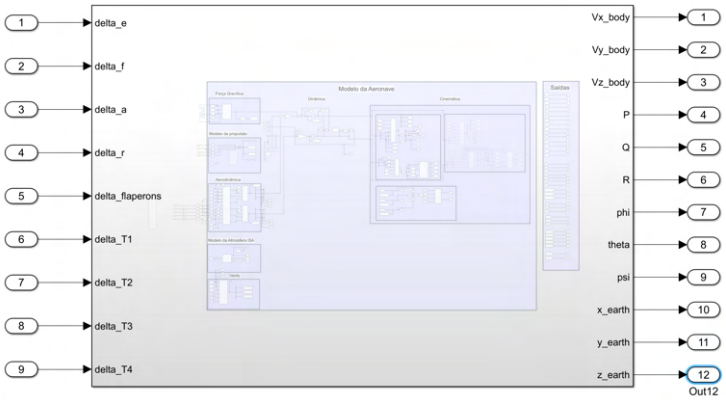

Figure 2.22: Implementation of the full nonlinear aircraft model in SIMULINK.

In this way, it is possible to carry out various types of simulations, being only necessary, to introduce an initial flight condition desired by the user and observe the behaviour of the output variables when subjected to a certain control or disturbance. The code can be found in a GitHub repository [13].

Chapter 3

Linear Control

This chapter describes the linear control design techniques that are going to be employed in this project. To do so, we need first to derive a linear model from the derived nonlinear model in the previous section by linearizing said model around a trimming flight condition that has a great dependency on the airspeed. We will take advantage of this dependency to create an airspeed gain scheduling, a design approach that constructs a nonlinear controller for a nonlinear plant by patching together a collection of linear controllers. These linear controllers will be blended by interpolation, which can be easily implemented using the available autopilot hardware and software.

3.1 Steady-State Trimming

First, before we can linearize a nonlinear model to derive the desired linear model, a trimming of the model is necessary to reach a certain flight condition where that linearization can be properly performed. This flight condition will be defined as a state where the aircraft maintains a steady wing levelled flight, which leads to constant forces and moments in the body-fixed coordinate system, with fixed controls making α, β and angular angles also constant, and therefore their derivatives equal to zero.

Assuming that the UAV flies at a constant altitude and velocity, V_T, we can draw the following conditions:

$$\begin{bmatrix} U = V_T cos(\alpha) cos(\beta) \\ V = V_T sin(\beta) \\ W = V_T sin(\alpha) cos(\beta) \end{bmatrix} \begin{bmatrix} p = 0 \\ q = 0 \\ r = 0 \end{bmatrix} \begin{bmatrix} \phi = 0 \\ \theta = ? \\ \psi = * \end{bmatrix} \begin{bmatrix} N = * \\ E = * \\ D = * \end{bmatrix} \tag{3.1}$$

$$\begin{bmatrix} \dot{U} = 0 \\ \dot{V} = 0 \\ \dot{W} = 0 \end{bmatrix} \begin{bmatrix} \dot{P} = 0 \\ \dot{Q} = 0 \\ \dot{R} = 0 \end{bmatrix} \begin{bmatrix} \dot{\phi} = 0 \\ \dot{\theta} = 0 \\ \dot{\psi} = 0 \end{bmatrix} \begin{bmatrix} \dot{N} = * \\ \dot{E} = * \\ \dot{D} = 0 \end{bmatrix} \tag{3.2}$$

where, (*) indicates that any value inside the flight envelope is possible to be used, and (?) indicates a trim variable. Furthermore we need to trim the input vector 3.3, where δ_e, δ_a, δ_r, δ_{T1}, δ_{T2}, δ_{T3}, δ_{T4}, are trim inputs and δ_f can be imposed depending on the flight phase.

$$\mathbf{U} = [\delta_e = ?; \quad \delta_f = *; \quad \delta_a = ?; \quad \delta_r = ?; \quad \delta_{T1} = ?; \quad \delta_{T2} = ?; \quad \delta_{T3} = ?; \quad \delta_{T4} = ?] \tag{3.3}$$

The values for the airspeed (V_T) will differ depending on the flight phase, so we will make several linearizations between the take-off speed and the maximum speed (30 m/s). The take-off speed will calculated with the following equation 3.4:

$$V_{Take-off} = 1.2V_{Stall} = 1.2\sqrt{\frac{2W}{S\rho C_{Lmax}}} \tag{3.4}$$

To calculate the value of the take-off speed, we need to calculate the maximum lift coefficient using the XFRL5 software previously described. We can obtain two estimated values for the two cases, one with no flaps, one with flaps deflected at 20º. The table 3.1, shows a summary of the conditions at which the nonlinear model is trimmed.

Table 3.1: Speed used for trimming with different flap deflection at take-off.

	V_T no fuselage	V_T with fuselage	δ_f	C_{Lmax}
	17.145	18.467	0	1.404
Take-off	16.091	17.331	20	1.594
Intermediate Speed	20	20	0	-
Intermediate Speed	25	25	0	-
Max. Speed	30	30	0	-

3.1.1 Algebraic Trim

With the conditions defined in 3.1 and 3.2, we can perform an algebraic trim to confirm the results obtained with the numerical trim in the next section and work as initial input for the same numerical trim. Due to the existence of a even number of rotors that rotate at opposite directions, which balances the roll moments created by each motor individually without the assistance of control surfaces, we can make an algebraic trim considering only the longitudinal mode.

The throttle deflection variable is replaced by the needed thrust to fulfil the trim conditions. Considering equations 2.15, 2.16, 2.39, 2.40, 2.43, 2.44, 2.45, the flight equations become:

$$C_{m_0} + C_{m_\alpha}\alpha + C_{m_{\delta_e}}\delta_e + C_{m_{\delta_f}}\delta_f + C_{m_{\delta_{fa}}}\delta_{fa} = 0 \tag{3.5}$$

$$-mg\sin\alpha - Drag\cos\alpha + Lift\sin\alpha + T = 0 \tag{3.6}$$

$$mg\cos\alpha - Lift\cos\alpha + Drag\sin\alpha = 0 \tag{3.7}$$

Equations 3.5 to 3.7, simplify the conditions for steady state flight, where:

$$Lift = (C_{L_0} + C_{L_\alpha}\alpha + C_{L_{\delta_e}}\delta_e + C_{L_{\delta_f}}\delta_f)\frac{\rho V_T^2 S}{2} \tag{3.8}$$

$$Drag = (C_{D_0} + C_{D_\alpha}\alpha + C_{D_{\delta_e}}\delta_e + C_{D_{\delta_f}}\delta_f)\frac{\rho V_T^2 S}{2} \tag{3.9}$$

We can make a system of three equations to determine θ, δ_e and T because δ_f values are predefined, considering each trimming speed. Note that in this case, θ equals α. With this solution, we can validate the numerical trim routines and obtain the results shown in Table 3.2 for the UAV without fuselage and Table 3.3 for the UAV with fuselage.

Table 3.2: Steady-state flight algebraic trim results for the UAV without the fuselage.

V_T [m/s]	δ_f[°]	U [m/s]	W [m/s]	θ [°]	δ_e[°]	T[N]
17.145	0	16.915	2.796	9.3849	-5.1193	4.198
16.091	20	16.091	2.457	8.7825	-5.6225	3.710
20	0	19.882	2.166	6.2182	-3.2903	3.657
25	0	24.965	1.318	3.0213	-1.4440	3.546
30	0	29.993	0.667	1.2747	-0.4352	4.039

Table 3.3: Steady-state flight algebraic trim results for the UAV with the fuselage.

V_T [m/s]	δ_f[°]	U [m/s]	W [m/s]	θ [°]	δ_e[°]	T[N]
18.467	0	18.215	3.039	9.471	-6.197	4.908
17.331	20	17.124	2.674	8.8755	-6.7979	4.333
20	0	19.819	2.681	7.7024	-5.0155	4.521
25	0	24.939	1.735	3.9792	-2.5275	4.093
30	0	29.983	1.016	1.9402	-1.1648	4.429

3.1.2 Numerical Trim

The other way to trim a nonlinear model is to trim numerically using the tools available in MATLAB/SIMULINK simulation environment. This numerical trim consists of a non-linear minimisation problem. Mathematically, it tries to find a trim point where the system's state derivatives equal zero. Trimming starts from an initial point and searches, using a sequential quadratic programming algorithm (SQP) [21], until it finds the nearest trim point. Furthermore, MATLAB provides a function that can find trim points that meet specific input, output, or state conditions. It can even find points where the system's state derivatives equal specific nonzero values. In this case, the idea is to find the variable input values for the MATLAB aircraft model that produces the minimum value at the conditioned outputs, and this will assure the verification in equation 3.2. The input vector is built according to equations 3.1 and 3.3. Trim data from this method is presented in Table 3.4 without fuselage and in Table 3.4 with fuselage.

Table 3.4: Steady-state flight numerical trim results for the UAV without the fuselage.

δ_f [°]	U [m/s]	W [m/s]	θ [°]	β [°]	δ_e [°]	δ_a [°]	δ_r [°]	δ_{Ti}	T_i[N]
0	16.9	2.8	9.400	0	-5.30	0	0	0.254	1.050
20	15.9	2.45	8.766	0	-5.94	0	0	0.284	1.658
0	19.9	2.17	6.245	0	-3.40	0	0	0.293	0.912
0	25	1.32	3.037	0	-1.51	0	0	0.401	0.886
0	30	0.668	1.272	0	-0.491	0	0	0.573	1.010

Table 3.5: Steady-state flight numerical trim results for the UAV with the fuselage.

δ_f [°]	U [m/s]	W [m/s]	θ [°]	β [°]	δ_e [°]	δ_a [°]	δ_r [°]	δ_{Ti}	T_i[N]
0	18.200	3.030	9.454	0	-5.200	0	0	0.289	1.226
20	17.000	2.660	8.881	0	-5.730	0	0	0.321	1.923
0	19.800	2.670	7.678	0	-4.170	0	0	0.309	1.128
0	24.900	1.730	3.982	0	-2.010	0	0	0.411	1.010
0	29.900	1.010	1.942	0	-0.829	0	0	0.579	1.089

3.2 Model Linearization

To linearize a non-linear model, we need to determine a set of first order differential equations, that represent the system around a steady state flight condition, where a numerical method is going to be used to achieve the representation of each individual model, using the tools available in MATLAB. The aircraft equations can be written as a continuous-time state-space model, that result in the following state equation 3.10 and output equation 3.11:

$$\dot{\mathbf{X}} = f(\mathbf{X}, \mathbf{U}, \mathbf{W}) \quad \mathbf{X}(n \times 1), \quad \mathbf{U}(m \times 1) \tag{3.10}$$

$$\mathbf{Y} = g(X, U), \quad \mathbf{Y}(n \times 1) \tag{3.11}$$

where **X** is the state vector, **U** is the control surface vector and **W** is the disturbance vector. The existence of the output equation is justified by the fact that not all the state variables are directly accessible.

With equations 3.10, 3.11 and considering a steady-state trimmed flight condition, we can expand this non-linear state equations in a Taylor series about the equilibrium point ($\mathbf{X}_T$, $\mathbf{U}_T$), keeping only the first order term:

$$f(\mathbf{X}, \mathbf{U}) = f(\mathbf{X}_T, \mathbf{U}_T) + \frac{\partial f}{\partial X}(\mathbf{X} - \mathbf{X}_T) + \frac{\partial f}{\partial \mathbf{U}}(\mathbf{U} - \mathbf{U}_T) = \mathbf{A}(\mathbf{X} - \mathbf{X}_T) + \mathbf{B}(\mathbf{U} - \mathbf{U}_T) \tag{3.12}$$

The partial derivatives can be numerically approximated:

$$\frac{\partial f}{\partial \mathbf{X}} = \frac{f(\mathbf{X}_T + \mathbf{x}_i, \mathbf{U}_T) - f(\mathbf{X}_T, \mathbf{U}_T)}{\mathbf{x}_i} \tag{3.13}$$

$$\frac{\partial f}{\partial \mathbf{U}} = \frac{f(\mathbf{X}_T, \mathbf{U}_T + \mathbf{u}_i) - f(\mathbf{X}_T, \mathbf{U}_T)}{\mathbf{u}i} \tag{3.14}$$

These expressions are obtained using MATLAB routine $linearize$. In this routine, the dynamics and control matrix are filled with the respective ratio between state variation at the output and the perturbation by applying a small perturbation to the trim conditions to each state and control input, resulting in the following results for the model flying at 30m/s in equations 3.15 and 3.16.

$$\mathbf{A} = \left[\begin{array}{cccc|cccc|cccc|ccc}
-12.81 & 0 & 0 & 0 & -0.432 & -0.010 & 0 & 0 & 0 & 0 & 0 & 0 & 0 & 0 & 0 \\
0 & -12.81 & 0 & 0 & -0.432 & -0.010 & 0 & 0 & 0 & 0 & 0 & 0 & 0 & 0 & 0 \\
0 & 0 & -12.81 & 0 & -0.432 & -0.010 & 0 & 0 & 0 & 0 & 0 & 0 & 0 & 0 & 0 \\
0 & 0 & 0 & -12.81 & -0.432 & -0.010 & 0 & 0 & 0 & 0 & 0 & 0 & 0 & 0 & 0 \\
\hline
1.53 & 1.53 & 1.530 & 1.530 & -0.033 & 0.270 & -0.645 & -9.804 & 0 & 0 & 0 & 0 & 0 & 0 & 0 \\
0 & 0 & 0 & 0 & -0.543 & -4.949 & 28.975 & -0.218 & 0 & 0 & 0 & 0 & 0 & 0 & 0 \\
-0.697 & -0.697 & -0.697 & -0.697 & 0.145 & -5.644 & -14.777 & 0 & 0 & 0 & 0 & 0 & 0 & 0 & 0 \\
0 & 0 & 0 & 0 & 0 & 0 & 1 & 0 & 0 & 0 & 0 & 0 & 0 & 0 & 0 \\
\hline
0 & 0 & 0 & 0 & 0 & 0 & 0 & 0 & -0.389 & 0.668 & -29.745 & 9.803 & 0 & 0 & 0 \\
0.209 & 0.056 & -0.056 & -0.209 & 0 & 0 & 0 & 0 & -0.595 & -3.926 & 1.257 & 0 & 0 & 0 & 0 \\
-6.877 & -1.834 & 1.834 & 6.878 & 0 & 0 & 0 & 0 & 1.455 & -0.637 & -1.077 & 0 & 0 & 0 & 0 \\
0 & 0 & 0 & 0 & 0 & 0 & 0 & 0 & 0 & 1 & 0.022 & 0 & 0 & 0 & 0 \\
0 & 0 & 0 & 0 & 0 & 0 & 0 & 0 & 0 & 0 & 1.0002 & 0 & 0 & 0 & 0 \\
\hline
0 & 0 & 0 & 0 & 0.999 & 0.022 & 0 & 0 & 0 & 0 & 0 & 0 & 0 & 0 & 0 \\
0 & 0 & 0 & 0 & 0 & 0 & 0 & 0 & 1 & 0 & 0 & -0.668 & 30.018 & 0 & 0 & 0 \\
0 & 0 & 0 & 0 & -0.022 & 0.999 & 0 & -30.018 & 0 & 0 & 0 & 0 & 0 & 0 & 0 & 0
\end{array}\right] \tag{3.15}$$

$$\mathbf{B} = \begin{bmatrix}
0 & 0 & 0 & 0 & 9.913 \\
0 & 0 & 0 & 0 & 9.913 \\
0 & 0 & 0 & 0 & 9.913 \\
0 & 0 & 0 & 0 & 9.913 \\
-0.849 & -4.711 & 0 & 0 & 0 \\
-11.976 & -16.565 & 0 & 0 & 0 \\
-293.423 & -12.487 & 0 & 0 & 0 \\
0 & 0 & 0 & 0 & 0 \\
0 & 0 & 0.882 & 6.090 & 0 \\
0 & 0 & -86.305 & 5.015 & 0 \\
0 & 0 & -3.323 & -27.146 & 0 \\
0 & 0 & 0 & 0 & 0 \\
0 & 0 & 0 & 0 & 0 \\
0 & 0 & 0 & 0 & 0 \\
0 & 0 & 0 & 0 & 0 \\
0 & 0 & 0 & 0 & 0
\end{bmatrix} \tag{3.16}$$

These dynamic and control matrix will have its states and control inputs rearranged in their order, given by equations 3.17 and 3.18, to make it easier to visualise and isolate the longitudinal and lateral modes:

$$\mathbf{X} = [T_1, T_2, T_3, T_4, u, w, q, \theta, v, p, r, \phi, \psi, N, E, D] \tag{3.17}$$

$$\mathbf{U} = [\delta_e, \delta_f, \delta_a, \delta_r, \delta_T] \tag{3.18}$$

In this linearized model the rotors input are merged into a single input, since for now no differential thrust will be used. The dynamics and control matrix can be divided in four major groups, according to

the lines in equation 3.15. The first four columns and four lines represents the motor dynamics. From lines 5 to 8 and columns 5 to 8, represents the longitudinal mode. From lines 9 to 13 and columns 9 to 13, represents the lateral mode. Lastly the last 3 lines represent the navigation dynamics.

For later sections, the rotors dynamics are eliminated assuming instantaneous response; the results obtained will then be applied to the completed model to assure that the controllers maintain its stability and performance.

The intersections between this groups of rows and second group of columns, along with the intersection between the second group of rows and first group of columns are the coupling modes. The existing values in those areas are quite small hence can be neglected; this will reduce the complexity of the controller design, because the lateral and longitudinal modes will be tuned separately.

3.2.1 Longitudinal modes

The longitudinal modes will only consider the state and inputs vectors illustrated in 3.19 and 3.20, a simplified motor dynamics by assuming that all three motor outputs have an instantaneous responses, and finally neglecting the influence of small differences of airspeed will have in its thrust output;

$$\mathbf{X} = [u, w, q, \theta] \tag{3.19}$$

$$\mathbf{U} = [\delta_e, \delta_T] \tag{3.20}$$

Since the coupling modes are residual, the dynamics matrix is extracted from matrices **A** and **B** for a speed of 30 m/s, that take in account the simplifications made, obtaining the following dynamic matrices:

$$\mathbf{A}_{long} = \begin{bmatrix} -0.2402 & 0.2658 & -0.6447 & -9.8036 \\ -0.543 & -4.9495 & 28.9750 & -0.2181 \\ 0.2389 & -5.6416 & -14.7770 & 0 \\ 0 & 0 & 1 & 0 \end{bmatrix} \tag{3.21}$$

$$\mathbf{B}_{long} = \begin{bmatrix} -0.849 & 4.736 \\ -11.977 & 0 \\ -293.423 & -2.158 \\ 0 & 0 \end{bmatrix} \tag{3.22}$$

Using damp, a MATLAB routine, we can display the damping ratio, natural frequency and poles of the linear model, shown in Table 3.6. We can see that all eigenvalues are complex numbers with negative real parts and so the aircraft is said to be dynamically stable, since all its poles are located on the left side of the imaginary axis in the complex plane. Also, the lowest frequency pole is associated with the phugoid mode and the other pair which is stable and fast is associated with the short period.

Table 3.6: Longitudinal mode poles

Poles	Damping	Frequency(rad/s)
-0.122+0.4i	0.291	4.180
-0.122-0.4i	0.291	4.180
-9.862+11.808i	0.641	15.385
-9.862-11.808i	0.641	15.385

3.2.2 Lateral modes

The lateral modes will only consider the state and inputs vectors illustrated in equations 3.23 and 3.24, a simplified motor dynamics by assuming that all three motor outputs have an instantaneous responses, and finally neglecting the influence of small differences of airspeed will have in its thrust output;

$$\mathbf{X} = [v, p, r, \phi, \psi] \tag{3.23}$$

$$\mathbf{U} = [\delta_a, \delta_r] \tag{3.24}$$

Since the coupling modes are residual, the dynamics matrix is extracted from matrices **A** and **B** for a speed of 30 m/s, that take in account the simplifications made, obtaining the following dynamic matrices:

$$\mathbf{A}_{lat} = \begin{bmatrix} -0.389 & 0.668 & -29.745 & 9.804 & 0 \\ -0.595 & -3.926 & 1.2567 & 0 & 0 \\ 1.455 & -0.637 & -1.077 & 0 & 0 \\ 0 & 1 & 0.022 & 0 & 0 \\ 0 & 0 & 1.0002 & 0 & 0 \end{bmatrix} \tag{3.25}$$

$$\mathbf{B}_{lat} = \begin{bmatrix} 0.882 & 6.090 \\ -86.305 & 5.015 \\ -3.323 & -27.146 \\ 0 & 0 \\ 0 & 0 \end{bmatrix} \tag{3.26}$$

Using again the MATLAB routine damp, we can display the damping ratio, natural frequency and poles of the linear model, shown in Table 3.7. We can see that most eigenvalues are real and negative, or complex with negative real parts except for a pole in the origin which corresponds to the integration of the yaw rate and a positive real pole that correspond to the spiral that is unstable, as it is usual in most aircraft. In conclusion, the aircraft maintains reasonable levels of dynamic stability. Also, the lowest frequency stable pole is associated with the roll mode and the other pair of complex poles associated with the dutch roll.

Table 3.7: Lateral mode poles

Poles	Damping	Frequency(rad/s)
0	-1	0
0.0678	-1	0.068
-4.187	1	4.187
-0.636+6.729i	0.094	6.759
-0.636-6.729i	0.094	6.759

3.3 Ardupilot control implementation and modelling

This section presents the details regarding the autopilot general architecture and controller computational model, which is also based in MATLAB/SIMULINK environment, to allow its interaction with the non-linear aircraft model, and takes into consideration the description of the autopilot below.

The Ardupilot project is the leading open-source software solution regarding UAV autopilots and it is mainly written in C++, supplemented with Python utility scripts. It offers autonomous operations for several types of vehicles like fixed-wing UAVs, multi-rotors, flapping wings, ground rovers, boats, submarines and even support for antenna trackers.

The adjustability of the code to each platform that it operates has an impact on the structure of the code itself, each vehicle has specific high level methods, usually related to physical aspects of each individual platform, that in turn makes use of the same low-level code libraries, the attitude control is one of those libraries. The autopilot operates with a real-time scheduler of several tasks but before a main loop can start, a setup phase will happen that corresponds to the initialization of the autopilot, this includes telemetry, various variables and sensors states initialization and also mission plan reading. After the setup, the main loop will begin, which contains sensor data updates, supplemented by Extended Kalman filtering, flight mode, mission updates, position control logic calculations, attitude control computations and an output function for the servos. A chart representing the many real-time tasks done during the operation of the ArduPlane software is shown in Figure 3.1.

What each task performs will depend on which of the following flight mode the autopilot is on. Since one of these tasks is responsible for stabilizing the aircraft, the aircraft will behave differently on each one of them:

- MANUAL mode, corresponding to manual radio control (RC), in which there is no autonomous stabilization;
- STABILIZE mode, similar to “MANUAL” but in which the autopilot is responsible for levelling the aircraft if the control inputs are zero;
- FLBW (fly-by-wire) modes, in which the autopilot is given the task of tracking the desired pitch and roll angles from the RC controls;
- ACRO (acrobatics) mode, in which the non-zero stick inputs are interpreted as angular rate references for pitch and roll and zero inputs are interpreted by the autopilot as an attitude hold;
- AUTO mode, in which the autopilot must follow a mission and fly autonomously.

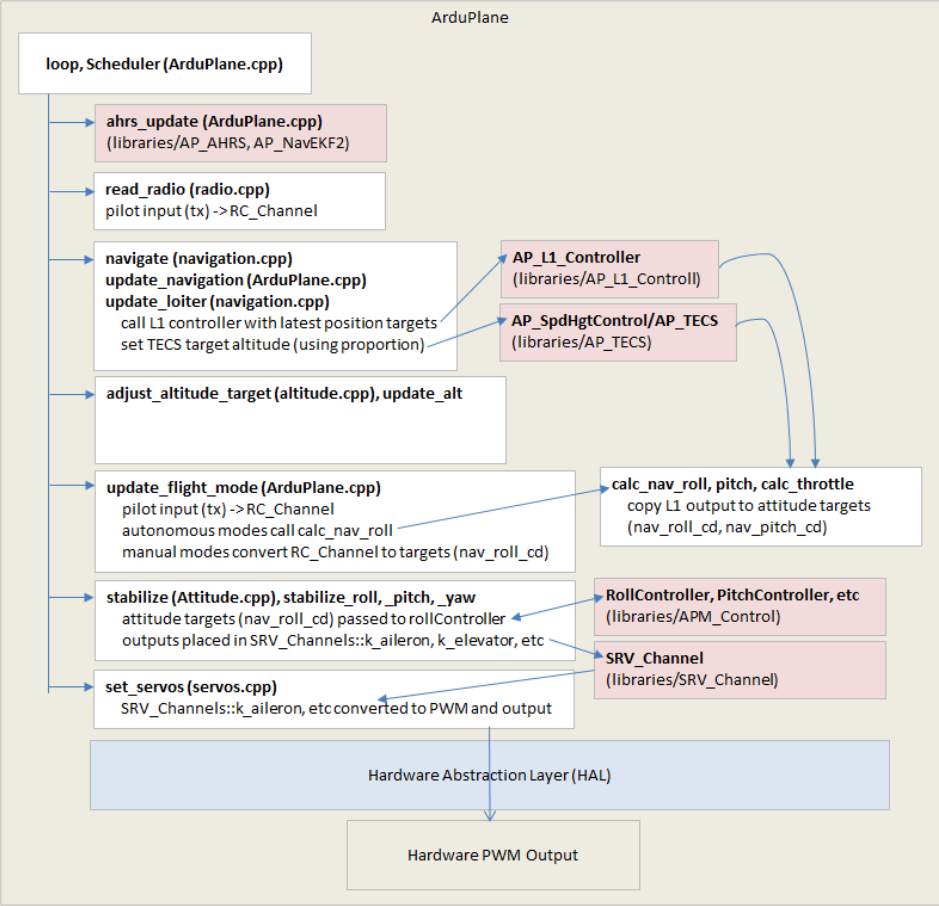

Figure 3.1: ArduPlane architecture.

The main difference between the multiple flight modes lies on the source of the references that are provided to the attitude controllers and whether or not the position control logic is bypassed. These attitude controllers are built with the use of PID algorithms. Also, the position controllers are accomplished, with a L1 algorithm responsible for lateral/directional navigation by setting the reference for the roll angle and a TECS algorithm being responsible for true airspeed and altitude control by setting the references for both the throttle and the pitch angle.

Additionally, the software includes a native software-in-the-loop (SITL) simulator that allows testing the code under development without the need for any additional hardware, the SITL environment can interface with a number of different vehicle simulators to obtain sensor data, which can be used in future works to test the code before moving from simulation to full autonomous controlled flight with more redundancy.

3.3.1 Attitude Control: Elevator Controller

In Ardupilot, the three aerodynamic control surfaces are used to control each Euler angle separately, one of them is the Elevator Controller which is ilustraded in Figure 3.2. This controller can be seen in two parts with an inner loop to increase stability and external servo-mechanism attitude control loop, which receives the pitch angle error and converts it to a pitch rate and limits it in order to reduce the chance

of stalling. This signal is added with an offset pitch rate term that is simply the pitch rate in coordinated turn [14], producing the reference pitch rate signal. This pitch rate signal is then used as input to inner loop stability augmentation PI rate controller. A feed-foward gain can also be used in the inner loop to improve the controller performance response if necessary.

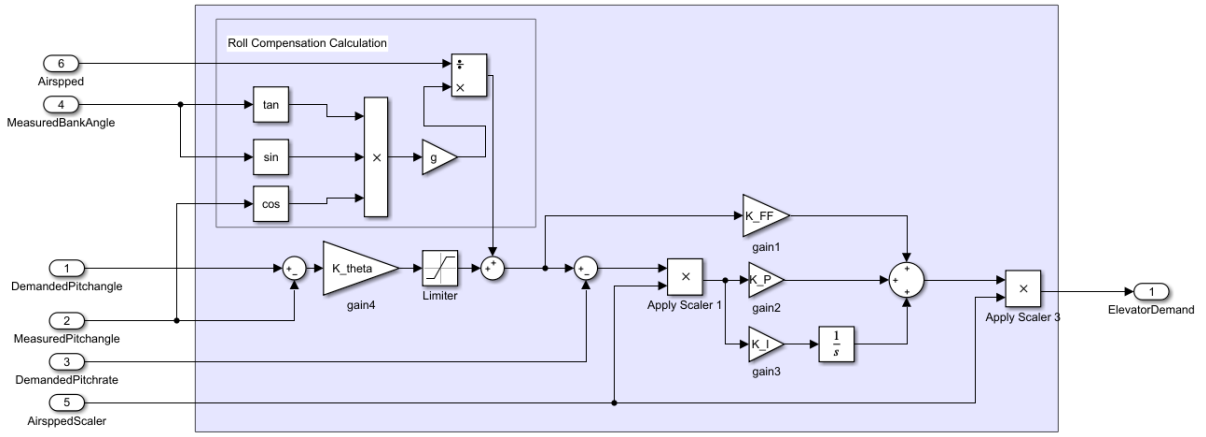

Figure 3.2: Elevator control schematic.

In Figure 3.2, the scaler blocks are used in order to extend the envelope of validity of the set of gains of the controller, they are a function of airspeed. Additionally in the code, the integrator incorporates an anti wind-up mechanism.

3.3.2 Attitude Control: Aileron Controller

The roll controller has a similar structure to the pitch controller but without the rate offset signal. As such, it consists of the same two parts with an inner ring to increase stability and external servo-mechanism attitude control ring, which receives the roll angle error and converts it to a roll rate and limits it in order to reduce the chance of stalling. This roll rate signal is then used as input to inner ring stability augmentation PI rate controller.

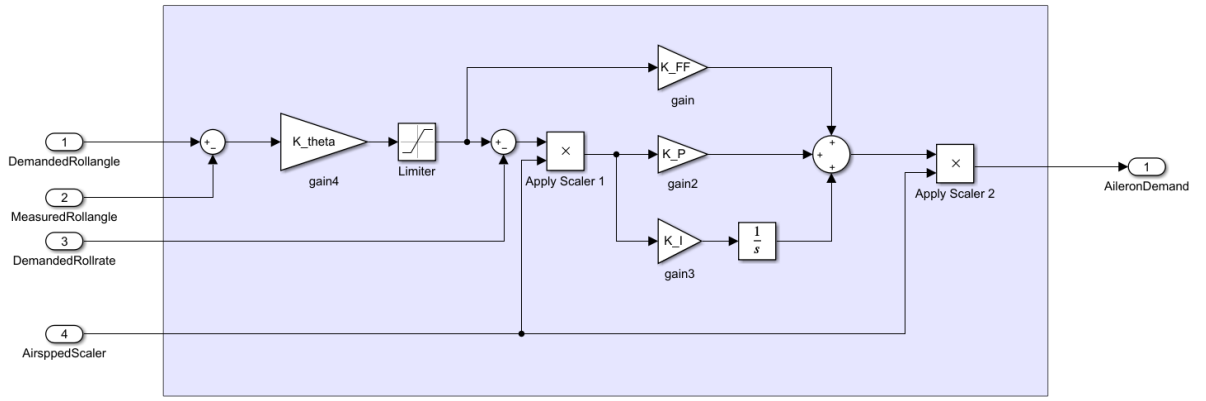

Figure 3.3: Aileron control schematic.

In the same way, the scaler blocks are used in order to extend the envelope of validity of the set of

gains of the controller, they are a function of airspeed. An wind-up mechanism is also incorporated and a feed-foward gain can also be used in the inner loop to improve the controller performance response if necessary.

3.3.3 Attitude Control: Rudder Controller

The rudder controller, shown in Figure 3.4, consists of a yaw damper system. The desired value for the yaw rate comes from coordinated flight equations and the yaw rate error is passed through a washout filter in order to correct only the dynamics and leave the stationary response in open loop.

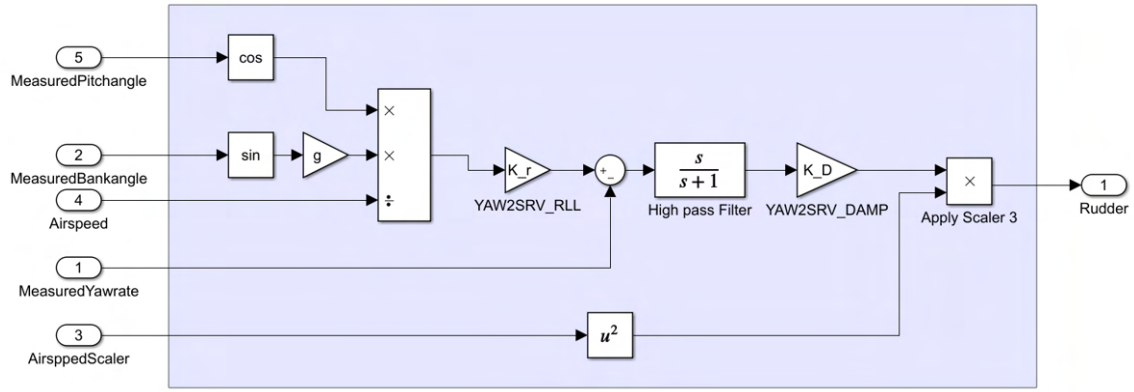

Figure 3.4: Rudder control schematic.

Additionally, lateral acceleration feedback can be used to keep tight control of the sideslip angle. However this is often neglected, because the control of side-slip uses measured lateral acceleration and it will only work for those UAV's that have enough fuselage side area to produce a measurable lateral acceleration when they side-slip, but we can still benefit from the yaw damper provided that we have a yaw rate control.

3.3.4 Position Control: TECS Controller

In these two sections, an overview of the position controllers used by Ardupilot are shown. The position control is divided in longitudinal and lateral motion. On the longitudinal plane, the Total Energy Control System (TECS) [22] is used. This algorithm was developed in the early 1980s and uses the total (mechanic) energy principles to control speed and height through throttle and pitch changes. The TECS controller aims to ensure that the total energy and energy differential of the plane is correct depending on the desired mission parameters such as altitude and velocity. The total energy, E_T is the sum of the potential and kinetic energies:

$$E_T = E_P + E_K; \quad E_P = mgh \quad E_K = \frac{1}{2}mV_T^2 \tag{3.27}$$

while, the energy difference is defined to be the potential energy minus the kinetic energy.

$$B = E_P - E_K; \tag{3.28}$$

The potential energy, E_P , is influenced by the altitude of the aircraft while the kinetic term, E_K, depends on its velocity. As a result, the algorithm has to fulfill two objectives, guarantee that the sum is correct and, on the other hand, to ensure the proportions of potential and kinetic energies are also corrected and so, the TECS acts as a height and speed controller. By monitoring the required total energy based on the mission altitude and velocity, obtained from the barometer and the airspeed sensor, it adjusts the throttle to keep the energy at the desired value. While the sum of the potential and kinetic energies can be right, individually their value can be incorrect, for example, if the aircraft is flying at low altitude but at high speed. And so, the controller tries to re-establish the balance between the two types of energies by adjusting the demanded pitch which will lead to a gain of altitude and a reducing on the velocity of the aircraft. The opposite applies if the aircraft is flying slowly but too high.

The adjustment of the gains of this controller will be set in future works either by using simulation or directly in future flight tests.

3.3.5 Position Control: L1 Controller

On the directional plane, the L1 algorithm [23] computes a roll reference signal based on waypoint positions, producing a roll angle reference, which follows two stages. First, from the current position of the aircraft and the desired heading that leads to the next waypoint, a lateral acceleration reference is computed by selecting the right L1 distance as illustrated in Figure 3.5 for a linear (or curved Figure 3.6) path to follow.

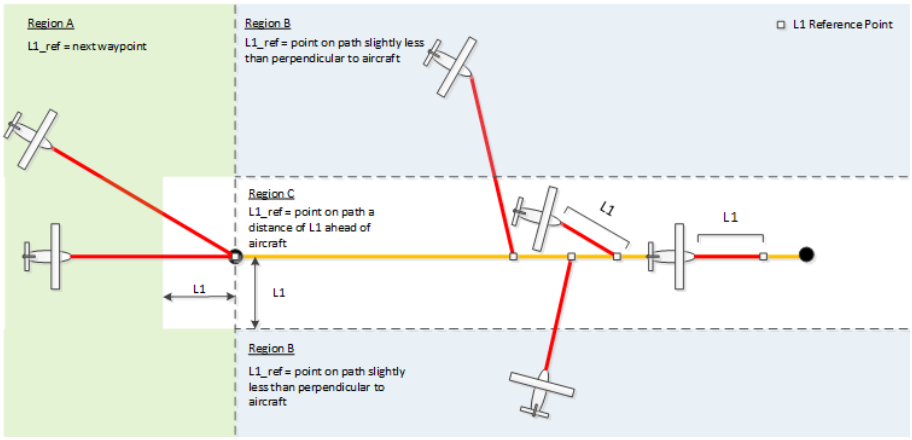

Figure 3.5: Illustration of the L1 algorithm along a linear trajectory.

The first reference is the next waypoint of the mission, afterwards, it will depend on whether the plane is far from the mission trajectory or not. If it is far from where it should be, the L1 reference point will be taken nearly perpendicular to the aircraft. If the vehicle is already in the proximity of the target, the reference point will be ahead of the plane. The same idea is used when the aircraft is in Loiter mode following circular trajectories, but with the radius error as a reference to change behaviour, when

Figure 3.6: Illustration of the L1 algorithm along a circular trajectory.

the aircraft is far from the target radius, the L1 distance points directly to the centre of target circular trajectory and when the radius error is small the reference point is ahead of the aeroplane.

Once the lateral acceleration command is obtained, a second calculation is responsible for estimating a roll reference signal that will allow to achieve the desired acceleration, using equation 3.29. And integral action is used to maintain straight flight when the error is small.

$$\psi_{cmd} = \cos\theta \arctan \frac{a_y}{g} \tag{3.29}$$

The adjustment of the gains of this controller will be set in future works either by using simulation or directly in future flight tests by flying a rectangular mission in AUTO mode and adjusting the L1 distance until we reach a desirable behaviour and a good compromise between having an UAV with aggressive turns with large oscillations and precise trajectory following.

3.4 Proposed Controller

With the Pixhawk Controller described in sections 3.3.1, 3.3.2 and 3.3.3, we could not find a solution that provided a stabilisation of the spiral mode, since the presence of the washout-filter in the yaw controller with a cut-off frequency of 0.2 rad/s would slowly create an instability since in this aircraft the

spiral mode is naturally unstable. And so we propose a controller without this filter and with some of the existing gains equal to zero, which lead to a cascaded-loop architecture with three inner P-only loops with feedback of the angular rates p,q,r to stabilise the UAV, and two outer PI loops to control the θ and ϕ orientation angles, making it compatible with the existing position controllers and making minimal changes to the existing code in order to minimise any possible accidents due to coding errors. The five proportional gains and two integral gains are all scheduled as a function of flight velocity.

3.4.1 Angular Rate Control

The inner loops are used to stabilise the UAV, with special attention to the spiral mode for each flight condition. Since the main focus will be on the spiral mode we start with a positive feedback loop of the yaw rate to the rudder input, using the following control law:

$$\delta_r = K_r(\dot{\psi}_{ref} + \dot{\psi}) \tag{3.30}$$

From the linearised model state-space matrices we can calculate the root locus for each condition. For example, for a speed of 30 m/s, is shown in figure 3.7.

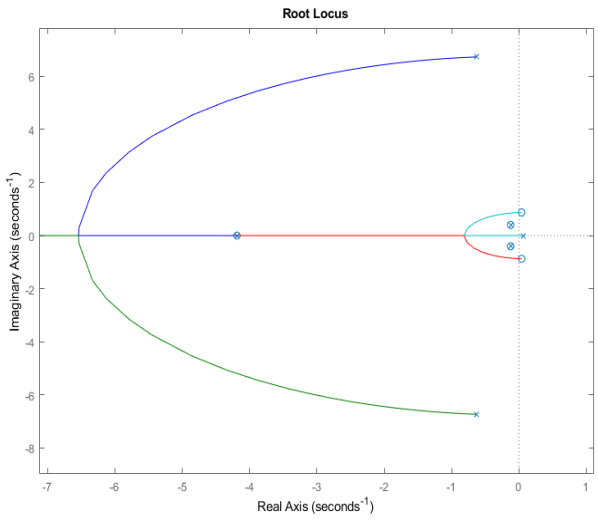

Figure 3.7: yaw rate root locus.

The influence of the gain K_r is analysed using the root-locus technique, generating the poles locations, as a function of K_r. The result of this graphical method, along with the poles of the closed loop for this particular value of K_r = 0.361 are in table 3.8.

Table 3.8: Lateral modes poles in closed loop of the inner loop.

Poles	Damping	Frequency(rad/s)
0	1	0
-0.132	1	0.132
-4.186	1	4.186
-6.288-0.1.866i	0.96	6.560
-6.288+0.1.866i	0.96	6.560

This value makes the pole associated with the spiral mode stable since it is now on the left side of the complex plane at the same time increasing the damping and frequency of the dutch roll mode and decreasing the frequency of the roll mode but still over 1 rad/s. From the lateral criteria in [24], we can confirm that the UAV still flies in level 1, the highest of these levels.

The following inner loop designed was the roll rate to aileron input with a negative feedback, resulting in the following control law:

$$\delta_a = K_p(\dot{\phi}_{ref} - \dot{\phi}) \tag{3.31}$$

From the linearised model state-space matrices we can calculate the root locus for each condition for this feedback loop and for example for a speed of 30 m/s this is shown in figure 3.8.

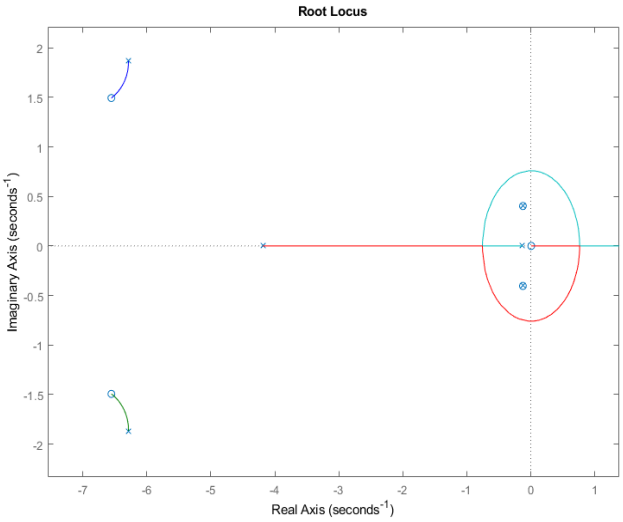

Figure 3.8: Roll rate root locus.

The influence of the gain K_p is analysed using the same root-locus technique, generating the poles locations, as a function of K_p. The result of this graphical method, along with the poles of the closed loop for this particular value of K_p = 0.0176 are in table 3.9. With this value we try to increase the frequency of the spiral mode without decreasing the frequency of the roll mode too much and without degenerating the two real poles. From the lateral criteria in [24], we can confirm that the UAV still flies in level 1, the highest of this levels.

Table 3.9: Lateral modes poles of the closed loop of the inner loop.

Poles	Damping	Frequency(rad/s)
0	1	0
-0.2792	1	0.279
-2.0315	1	2.032
-6.336-0.1.685i	0.97	6.560
-6.336+0.1.685i	0.97	6.560

We can accomplish two important lateral goals with these two feedback loops, stabilise the spiral mode and increase the damping of the dutch roll mode.

The following inner loop designed was the pitch rate to elevator input with a positive feedback, resulting in the following control law:

$$\delta_e = K_q(\dot{\theta}_{ref} + \dot{\theta}) \tag{3.32}$$

From the linearised model state-space matrices we can again calculate the root locus for each condition for this feedback loop and for example for a speed of 30 m/s this is shown in figure 3.9.

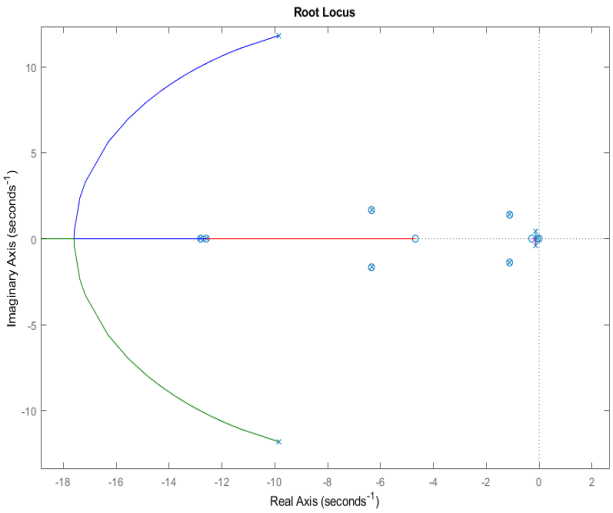

Figure 3.9: Pitch rate root locus.

The influence of the gain K_q is analysed using the same root-locus technique, generating the poles locations, as a function of K_q. The result of this graphical method, along with the poles of the closed loop for this particular value of K_q = 0.036 are in table 3.10, this gain value was chosen in order to increase the damping of the longitudinal modes. From the longitudinal criteria in [24], we can confirm that the UAV still flies in the level 1, the highest of these levels.

Table 3.10: Longitudinal mode poles of the closed loop of the inner loop.

Poles	Damping	Frequency(rad/s)
-0.1241+0.395i	0.327	0.380
-0.1241-0.395i	0.327	0.380
-15.661+6.792i	0.917	17.010
-15.661-6.792i	0.917	17.010

For all conditions, the gains vectors calculated are in equations 3.33, 3.34, 3.35:

$$K_r = [0.679 \quad 0.586 \quad 0.423 \quad 0.361] \tag{3.33}$$

$$K_p = [0.034 \quad 0.0321 \quad 0.0221 \quad 0.0176] \tag{3.34}$$

$$K_q = [0.0638 \quad 0.0459 \quad 0.0395 \quad 0.036] \tag{3.35}$$

3.4.2 Attitude Control

We will now focus on the two gain-scheduled PI loops controlling roll and pitch angles. These outer loops are given by the following control laws:

$$p_{demand} = K_\phi(\phi_{ref} - \phi) + I_\phi \int (\phi_{ref} - \phi)dt \tag{3.36}$$

$$q_{demand} = K_\theta(\theta_{ref} - \theta) + I_\theta \int (\theta_{ref} - \theta)dt \tag{3.37}$$

These loops are tuned for each flight condition using the MATLAB routine *systune* to tune the PI gains for specific goals, in this case a phase margin of 40 dB, a gain margin of 6 db and a target time response between 3 and 30 seconds.

To tune the outer loops, we close the inner loops and obtain a linearized model of the plant seen by the outer loops, but to get the correct linearization, we set tuner in such a way that the inner loop gains vary with flight velocity and this is possible with block substitution in the SIMULINK enviroment. After the automated tuning we achieve the following results:

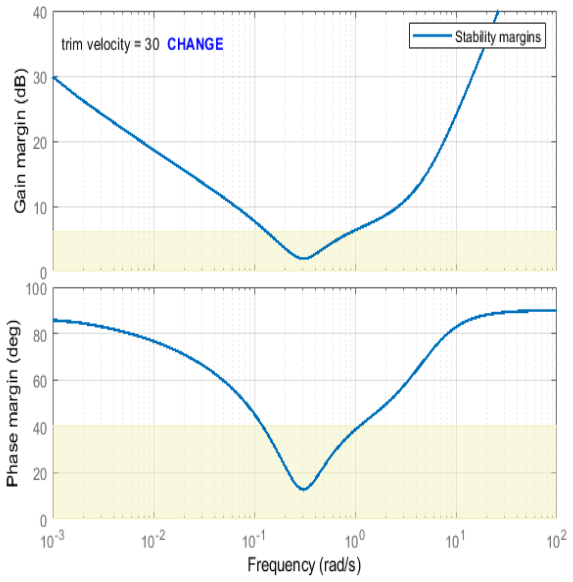

Figure 3.10: Stability Analysis Using Gain and Phase Disk Margins.

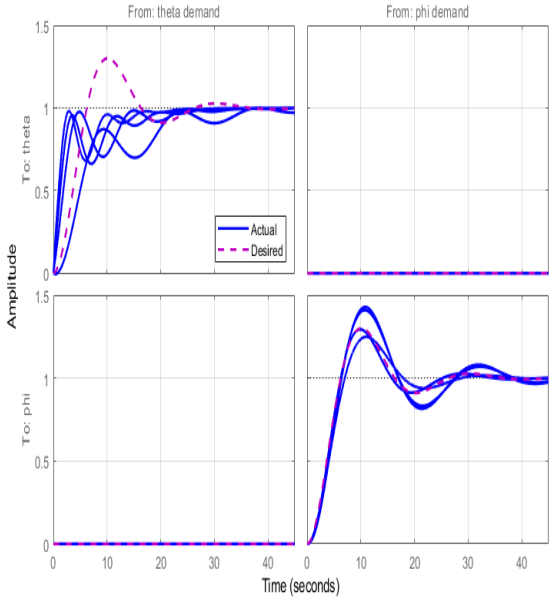

Figure 3.11: Obtained system time response.

We can conclude that the system cannot reach an adequate phase and gain disk margins around 0.3 rad/s, even with a relaxed target for the time response. And so we have to conclude that the controller design did not accomplish all its goals since it does not provide the target stability and at the same time its time response is quite slow. To end this section we present the gains obtained with this method, for different flight conditions:

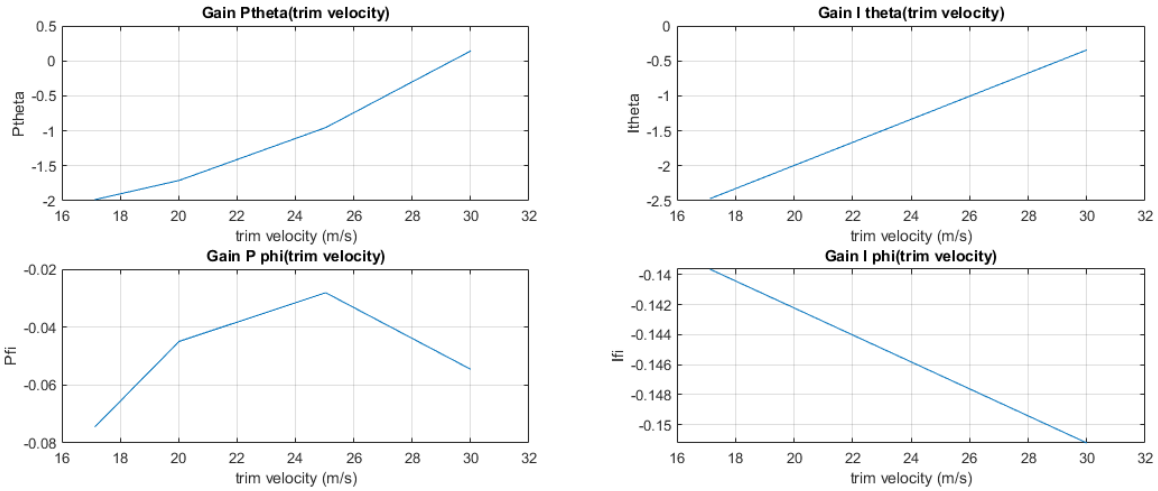

Figure 3.12: Gains obtained after tuning the outer loops.

Chapter 4

Implementation

4.1 Construction of the UAV model

Since the main objective of this project is to test the feasibility of a new proposed aircraft configuration, an UAV prototype with the physical dimensions of the scaled-down with a scale factor of 1:10 is built. This scale factor was defined by the consortium of enterprises involved in the project, with the proposed full scale aircraft having a 1.5 meter wingspan.

In this section, a summary of the construction process will be described with an overview of the avionics system mounted in the prototypes. At the beginning of the project, it was only planned to build one model (F-01), together with several partners. But after the tests on an aeromodelling runway, the decision was made to move towards constructing a new model (F-02) with a much lower wing loading. Some challenges for the FLEXCRAFT concept have been identified, such as the landing gear and longitudinal stability. The potential of the concept remained, regardless of the reduction of wing loading to facilitate and guarantee the proper safety in flight tests.

A scaled model with a scale factor of 1:15 was also developed by L. Eusébio [25], that serves as a test benchmark to the several avionics and develop further the VTOL concept envisioned for one of the configurations of this concept aircraft. The work done in this model has been thoroughly described, and the results can be seen in [25].

4.1.1 F-01 construction

The choice of materials and the definition of the internal structure of the UAV was carried out in collaboration with SETsa. Regarding the mass of the UAV, no direct scaling was applied to allow greater freedom to achieve the scaling of the CM and the static margin, which were considered more important to ascertain the airworthiness of the modular concept proposed in the project. Therefore, the mass was determined based on the defined internal structure, materials used and selected components. To demonstrate the airworthiness of the aircraft with and without a fuselage, all essential flight systems (propulsion, batteries, controllers, actuators, wiring, landing gear, avionics and electronic systems) will be integrated into the sustaining system, making it the most critical UAV system. In contrast, the fuse-

lage module can be interpreted as a representative mass (with reference to the mass of the support system) whose external geometry is staggered. Having this in consideration, the sustaining system is then divided into five parts, main wing; tail (horizontal and vertical stabilisers); front booms (where the propulsion system is integrated); rear booms (connecting structure between the main wing and the warp) and landing gear.

Different structures were initially designed for the UAV based on the existing manufacturing techniques and technologies within the consortium. However, to give robustness to the main wing, a structure composed of aluminium spars and ribs and a skin in laminated composite material was chosen. The internal aluminium structure makes it possible to form a robust metallic "skeleton" that facilitates the integration of the connection elements to the propulsive system (front booms), tail (rear booms) and landing gear using a beam (peripheral beams and the beams of the rear booms) and the integration of control surface actuators as well as other essential flight components such as batteries and flight controller.

The control surfaces (flaps and flaperons) were designed to be made of ABS with material reinforcements at the place of connection to the actuator. Access panels were planned for the composite skin to facilitate access to the wing's interior to replace some components such as actuators and batteries. In the central axis of the wing, there is an aluminium beam (central Rib) to which the fuselage will be screwed when the UAV flies with the fuselage module. Figure 4.2 and Figure 4.1 illustrate the structure of the main wing with the details mentioned above.

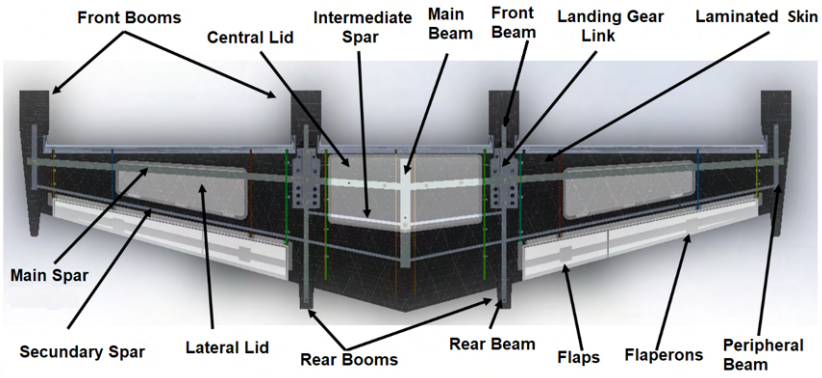

Figure 4.1: Internal Structure of the main wing of the F-01 UAV.

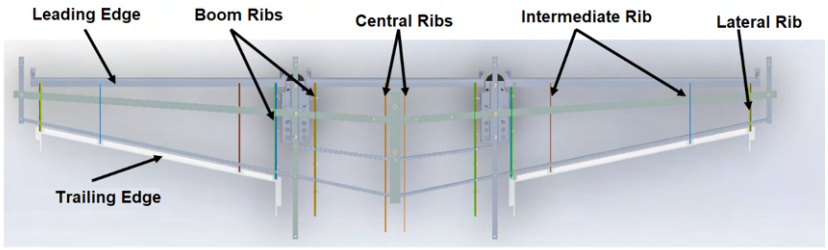

Figure 4.2: Internal Structure of the main wing of the F-01 UAV, ribs, leading and trailing edge.

The thicknesses of the internal structure (stringers and ribs) were defined such that they supported without breaking an aerodynamic load corresponding to $4.7g$, which was chosen by the consortium since

it is commonly used in general aviation.

Since the front booms are key components to support the electric propulsion system, consisting of the propeller and the electric motor, they have to be strong enough to support the forces and moments created by this system; due to the difficulties in achieving the necessary static margin, and since these components are in front of the neutral point of the sustaining system, these front booms are made of steel, as one can observe in Figure 4.7, and finally covered by the carbon composite wing skin.

The rear booms are responsible for transmitting the loads generated in the tail to the internal structure of the main wing; these were designed with an internal aluminium beam and an ABS shell. In the final iteration of this UAV prototype; they were replaced by carbon fibre tubes that provided a lighter solution.

For the horizontal and vertical tails, the same type of internal structure was followed as for the main wing, spars and ribs, although the loads to which they are subjected are lower. The struts of the vertical stabilisers were designed in aluminium and connected to the rear boom using screws, forming a robust metallic “skeleton” to which the rear landing gear is also connected. To provide a more aerodynamic shape to the connection of the horizontal stabilizer with the vertical stabilisers, without prejudice to the longitudinal stability and structural consistency, two nylon connection pieces were designed by SETsa, whose external geometry was provided by Alma Design; these were later replaced by a similar one but made out of Polylactic acid (PLA), that was designed in Instituto Superior Técnico (IST) by Pedro Pinto due to their lighter weight. These parts are connected to the side members of the horizontal stabiliser (aluminium). The actuators on the control surfaces are made of ABS using additive manufacturing and have been integrated between the main stringers. The ribs, as well as the outer shell, are also made of ABS. The figure 4.3 shows the structure of the tails with the details previously described. The same aerodynamic loads of $4.7g$ defined the tail internal structure thicknesses (stringer and ribs) .

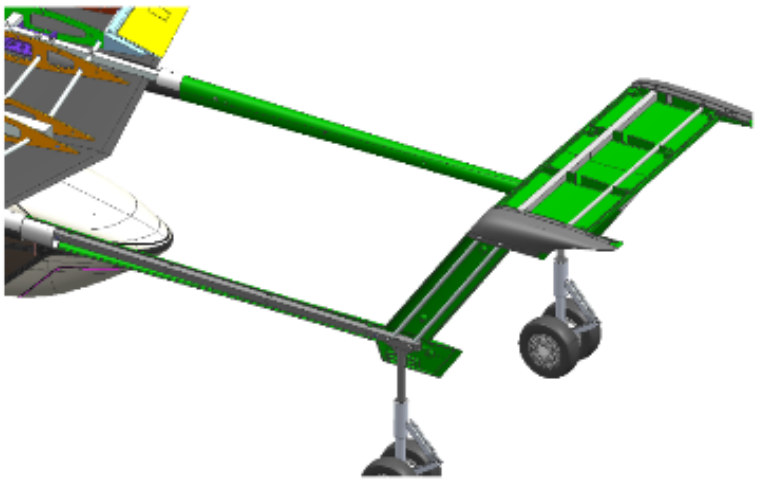

Figure 4.3: Tail Structural Design.

Both Landing gears were designed in IST, with the intention to adopt some available components in the market to the specific structure of the UAV plane. The front landing gear was bought from *Xicoy*, which was equipped with an electric brake capable of slowing down the UAV in the runway, important due to the characteristics of the aircraft. The pilot then controlled these via radio control received by

the onboard computer board. The rear landing gear was also bought from a shop specialised in radio-controlled (RC) components and both landing gears were then adapted to the structure of the UAV with some in-house built adapters manufactured by Simão Rodrigues.

Figure 4.4: Rear Landing Gear.

Figure 4.5: Front Landing Gear mounted in F-01 UAV.

The fuselage was planned to be a simple component in the UAV without essential flight systems. It was designed to be composed only of an external ABS shell (which already includes an integration zone, designed by SETsa, which facilitates its coupling with the main wing) and a hollow interior, as shown in Figure 4.6 without any paint applied. And so, with the integration of the avionics described in section 4.1.3, the UAV is complete.

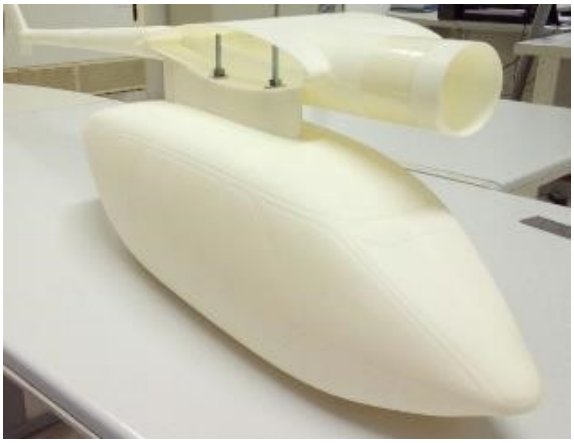

Figure 4.6: F-01 fuselage, not painted.

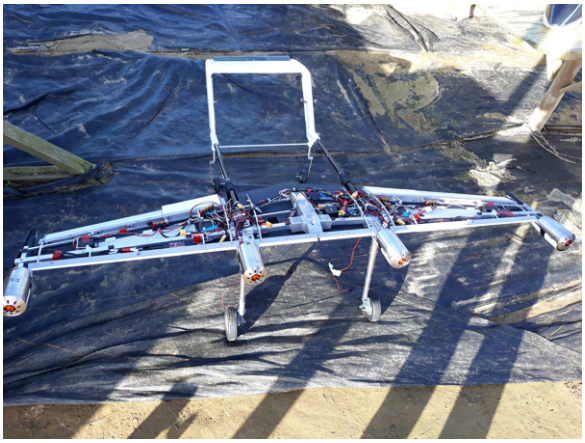

Figure 4.7: F-01 final iteration, without the upper carbon fibre shell in a aeromodeling airfield.

This kind of construction can be extremely robust, shown in the accident that occurred during the runway tests, but created several problems in terms of flight due to the low energy autonomy due to the space available for that purpose and also since it uses batteries that still at the time of writing have an extremely lower energy density in relation to fossil fuels. Also, the high weight corresponds to a higher stall speed, and so a larger runway is needed to land and take off. Finally, the higher speed will correspond to a large distance from the pilot in several moments of flight that will correlate to a lower sensibility in terms of control of the UAV. So a similar prototype was proposed with a lower wing loading with lighter materials but with similar or better stability characteristics.

4.1.2 F-02 construction

For the construction of the model with less weight and therefore less wing loading, different construction methods and materials were considered, each one with its costs and benefits. After weighing in all different options, we opted for a mixed composition of carbon fiber, balsa wood, plywood, polyurethane foam (XPS) and polylactic acid (PLA). Still, in this model, no weight direct scaling was applied to allow greater freedom to achieve the scaling of the CM and the static margin, which were considered more essential to ascertain the airworthiness and complete the construction and testing, with success, of the modular concept proposed. Furthermore, in this model, time and human resources were a lot more restricted, and so adding more objectives would be unfeasible, although it comes closer to a scaling of weight.

Again, to demonstrate the airworthiness of the aircraft with and without a fuselage, all essential flight systems (propulsion, batteries, controllers, actuators, wiring, landing gear, avionics and electronic systems) will be integrated into the lifting system while the fuselage module can be interpreted as a representative mass whose external geometry is staggered. Having this in consideration, the sustaining system is then again divided into five parts, main wing; tail (horizontal and vertical stabilisers); front booms (where the propulsion system is integrated); rear booms (connecting structure between the main wing and the warp) and landing gear.

The wing structure was constructed using tubular booms made out of carbon fiber, the ribs made of plywood using laser cutting for its manufacture (Figure 4.8), stringers made of balsa and platforms to mount and allocate several components. Balsa wood was also used for its shell, as shown in Figure 4.9 and then reinforced with carbon fiber (Figure 4.10) and/or fiberglas fiber (Figure 4.9).

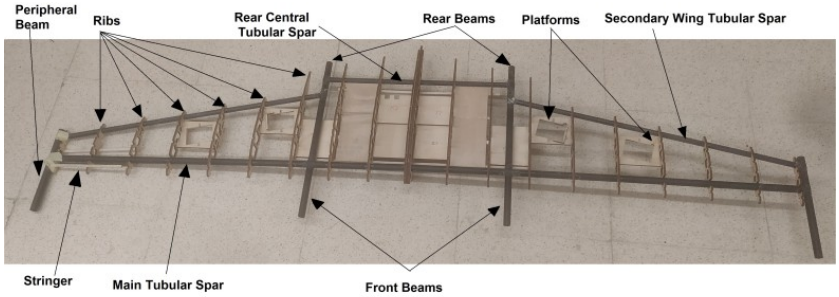

Figure 4.8: Built Internal Structure of the main wing of the F-02 UAV, tubular spars, ribs and platforms for components.

Figure 4.9: Main wing with the balsa wood skin and the lamination with glass fiber.

The internal carbon tube structure makes it possible to form a robust “skeleton” that facilitates the integration of the connection elements to the propulsive system (front booms), warping (rear booms)

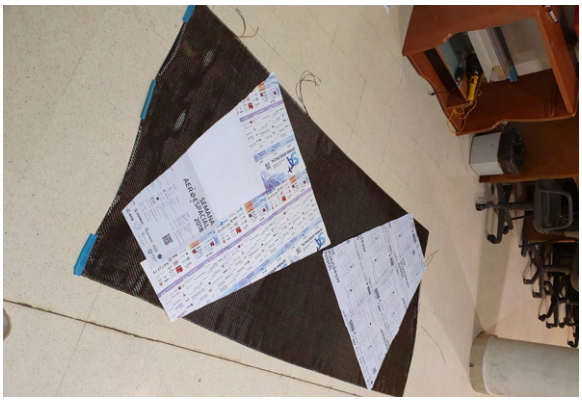

Figure 4.10: Carbon fiber templates for wing lamination

and landing gear using a beam (peripheral beams and the beams of the rear booms) and the integration of control surface actuators as well as other essential flight components such as batteries, servos and flight controller.

The control surfaces (flaps and flaperons) were designed and made by Pedro Pinto out of PLA (Figure 4.11). Concerning the tail, both the rudders and elevator were made of XPS and reinforced by carbon fiber (Figure 4.12). This main difference comes from one of the most important lessons learned in the previous iteration: the difficulty of achieving a stable static margin due to a tail design that discarded the importance of achieving the minimal possible weight due to the aircraft configuration.

Figure 4.11: Flaps and Flaperons for F-02.

Figure 4.12: XPS with carbon reinforcement elevator and rudder mounted in F-02.

The tail structure itself was manufactured using XPS using a hot wire cutting technique and laser-cut Medium-density fibreboard (MDF) templates. The horizontal tail was later reinforced with small carbon tubes inserted by making small holes that were later closed with a low-density filler. These tubes are essential to connect the horizontal tail to both the vertical tails and complete the structure of the stabiliser. Before this assembly, both tails were laminated with carbon fiber using a vacuum bag cure. The booms that connect the tail to the wing structure are made of carbon fiber composite and are inserted directly in the rear beams illustrated in Figure 4.8.

The motor supports and the nacelles that surround them were manufactured in PLA through 3D printing. These were designed to fit in the carbon booms, being later screwed but allowing the passage of the motor air as well as its cables. The nacelle consists of three parts: front, top and bottom nacelles that fit the motor mount and each other. These were printed to be able to fulfil their function with reduced weight, and so the wall thickness is configured for only 2 layers of 0.4 mm. The front part of the nacelle

covers the motor and allows it to rotate freely. The upper and lower parts are designed to fit the wing, and together, they embrace the carbon beam.

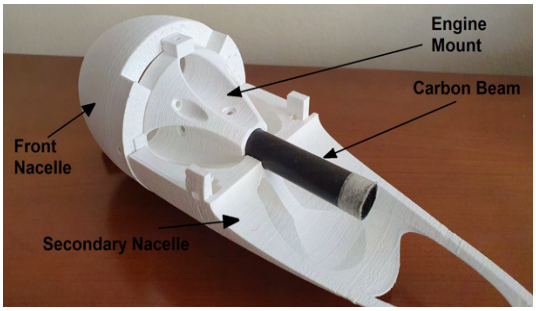

Figure 4.13: Engine mount and nacelles in PLA .

Figure 4.14: Engine mount in lateral motor and complete nacelle in central motors.

Access panels were planned to facilitate access to the wing's interior to replace some components such as actuators and batteries. The two larger central lids have several points of attachment to the structure, and at the same time, these lids have several stringers which can be fitted to several ribs that exist. Additionally, the wing has a central rib to which the fuselage will be screwed when the UAV flies with the fuselage module, and this component is reinforced with carbon and glass fiber.

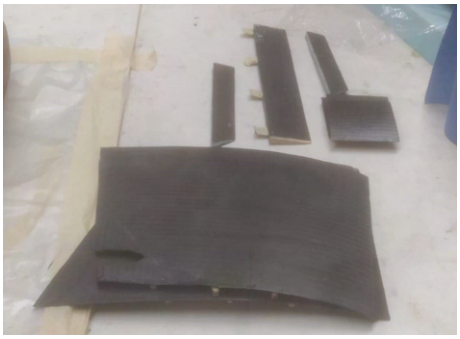

Figure 4.15: Central lid.

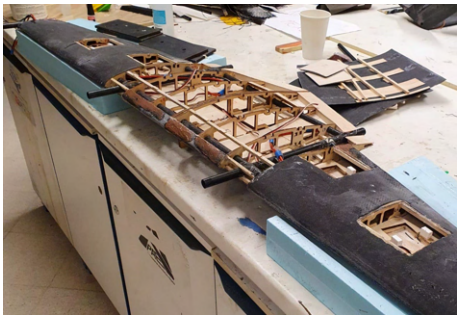

Figure 4.16: Lids

With regard to the front landing gear, a carbon fiber landing gear was purchased, which was later adapted for its installation in the UAV by clamping it to the main carbon spar using carbon clams (see Figure 4.18). The rear landing gear was made by a simple aluminium strip that was deformed to create two small but resistant skis, which is very important in the design because it leads to a very light solution in the back end of the prototype.

The fuselage will be detachable from the UAV completely to simulate the modularity of the proposed aircraft and so it needs to fly without any essential flight systems inside it. This fuselage was built using several plywood ribs and balsa wood stringers to give it the appropriate shape and then covered with a balsa skin, as shown in Figure 4.19. Additionally, 3D printing parts were used to make the complex shapes of both ends of the fuselage, and a coupling piece was designed and 3D printed to attach the fuselage to the central rib in the main wing. The final layer was reached using low-density filler and spray paint, as shown in Figure 4.20.

We have to note that the construction of this new version of the UAV was temporarily suspended due to restrictions imposed by the Covid-19 disease pandemic, which extended the building time sig-

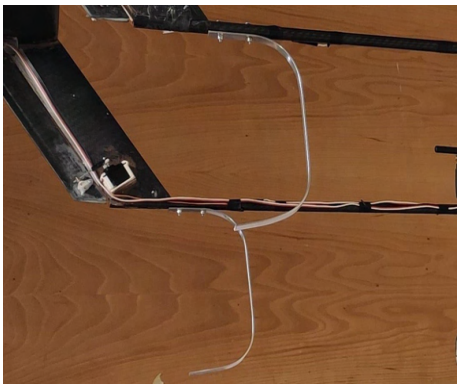

Figure 4.17: Rear Landing Gear.

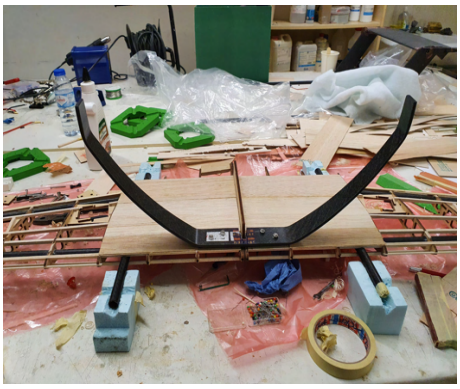

Figure 4.18: Front Landing Gear mounted in F-01 UAV.

Figure 4.19: Fuselage with applied filler and paint.

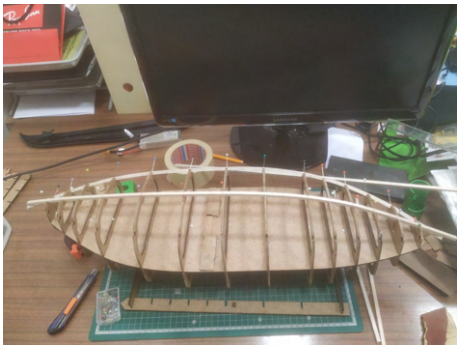

Figure 4.20: Fuselage inner structure.

nificantly. Finally, in terms of instrumentation, the new aircraft will be similar to the first UAV, with the most significant difference being the arrangement of electronic components inside the aircraft, due to differences in the internal structure, that is described in section 4.1.3.

4.1.3 Avionics

In this section, we briefly show an overview of the avionics system and its components. These components are essential to maintain a controlled, sustained flight and provide the tools and data to test and validate the work developed in this thesis.

The main component of the avionics system, responsible for the control of the aircraft is the computer board (Figure 1.2). The Pixhawk cube board is a market solution that is capable of receiving and sending the necessary data across the UAV without the need to spend a tremendous amount of time, creating an in-house solution. The board comes with several important features, listed below:

- 32bit STM32F427 Cortex-M4F core (168 MHz / 252 MIPS, 256 KB RAM, 2 MB Flash).
- 14 PWM output channels (Servo and Motor outputs).
- Abundant connectivity options for additional peripherals (UART, I2C, CAN), necessary to use an external sensor like an airspeed sensor, a Global Positioning System (GPS) and a sonar in this case, but many more can be integrated if necessary.
- External safety switch that provides a safer operation.

- MicroSD card for high-rate logging over extended periods of time.
- Three independent IMU (Inertial Measurement Unit), necessary to calculate the aircraft's attitude correctly.

This board is also compatible with the Mission planner ground station, an open-source software with several convenient tools for flight tests.

Regarding the servo actuators, they were chosen based on the estimated torque for the control surfaces (considering its dimensions and a maximum allowed deflection of 40 degrees for the flaps, 32 degrees for flaperons and 30 degrees for the elevator and rudders), resulting in an estimated torque of 3.17 kg.cm for flaps, 3.09 kg.cm for flaperons, 1.64 kg.cm for the elevator and finally 0.24 kg.cm for rudders.

Since similar values are obtained for flaps and flaperons, and to allow a greater standardisation of the equipment, the same actuator, the Futaba S3003, was chosen (see Figure 4.21), which can produce a maximum torque of 4 kgcm. On the other hand, the elevator and rudders have the same actuator as well, and so the SUMO 90 MG is used (see Figure 4.22), whose maximum torque is 1.8 kg.cm. Finally, the reason for not using a lower capacity actuator for the rudders was due to the difficulty of finding one in the market. All values are available and were retrieved from [4]. Finally, the other available actuators are the rotors, and their behaviour and description are already described in the subsection 2.4.2.

Figure 4.21: Main wing servo, used for the ailerons and the flaps.

Figure 4.22: Tail servo, used for the elevator and the rudders.

Additionally, four batteries were chosen (Tattu Bateria 2300MAH 11.1V 45C 3S1P Lipo), each one of them providing power to each motor. Lipo batteries were chosen since they provide the best energy to weight ratio available in the market and their dimensions were carefully selected since there was a restricted space available on the wing, which has to carry all the necessary electric components necessary for flight.

Using the computational model built in the previous section and simulating a levelled flight at 25 m/s at a constant altitude, we can estimate an endurance of approximately 5 minutes of flight for the F-02 prototype, which in turn provides even more reasons to build this UAV to make any test necessary. It should be noted that since the energy density of batteries (around 200 Wh/kg) are still very low compared

to gasoline (around 12,000 Wh/kg), it can be hard to make an electric UAV with considerable endurance with the space available in the wing alone.

Figure 4.23: Battery used for the F-01 and F-02 prototypes.

Since every UAV built in this project is radio-controlled, the aircraft must be able to communicate with the pilot throughout all its flight. With this requirement in mind, a test to check the range of the radio used was carried out, to verify that it would present a signal with sufficient strength for a safe operation without any loss of communications. For this test, the aircraft and the radio emitter were placed in the following locations (IST-soccer field and the *Fonte Luminosa* Monument, respectively), and the signal quality was monitored.

Figure 4.24: Long range RC (radio controller)/Telemetry transmitter and receiver (RFD868x bundle modem)

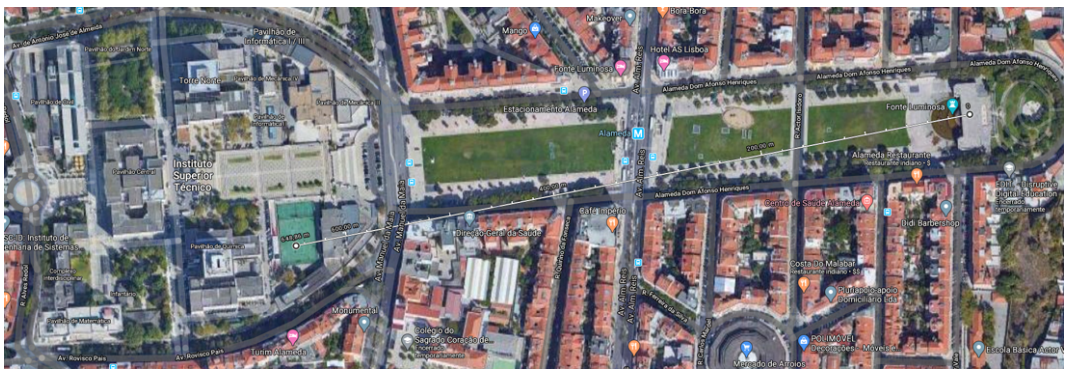

Figure 4.25: Distance between UAV and RC emitter.

It was possible to verify that all channels of the emitter and receiver were working in the correct

way and in addition to the distance of approximately 650 meters, the existence of a building blocking the emitter's field of view (see Figure 4.25), which indicates that the used emitter has the necessary characteristics for the flights in question.

Finally, the last three avionics that will be addressed are the airspeed sensor, the GPS receiver and ground station, and a sonar (see Figure 4.26). The airspeed sensor is incorporated into the plane to get the necessary information about the airspeed with a range between 0 and roughly 100 m/s (360km/s), with a digital output and I2C interface, the total error is less than 1.0% [26].

A GPS sensor is also necessary to give a localization that can be used as a reference for the navigation algorithms. To achieve this task, we use the Pixhawk GPS receiver and its GPS ground station (see Figure 4.26 (b)), achieving a very high precision for a GPS system, depending on the time that the base station surveys the reference home location. Testing shows that, in an open area, to achieve an absolute accuracy of 2 meters it takes a few minutes. To reach the absolute accuracy of less than 30 cm takes around an hour, and to reach the accuracy of 10 cm it takes a few hours [27].

Lastly, a sonar is used to get a more precise distance between the aircraft and the ground that can be used 0-7.65 meters with a 1cm resolution and is linked to the Pixhawk via an I2C communication protocol [28]. This sensor will be used in future works, in order to provide automatic landing and take-off capabilities.

(a) (b) (c)

Figure 4.26: External sensors, right to left: (a) Airspeed sensor and pitot (b) GPS receiver and ground station (c) Sonar sensor.

Chapter 5

Tests and Results

5.1 Center of mass determination

The correct location of the UAV center of mass (CM) and the measurement of the mass itself is essential for aircraft stability and, consequently, for flight safety. In order to locate the CM, one system, consisting of a four-point measurement system, is employed. In each of these points, a bar that contains a load cell is used to measure the weight. The UAV is placed on these load cells in a position such that the aircraft is upright (i.e., aircraft without pitch angle), as shown in Figure 5.1.

The load cells are connected to a microprocessor that transmits the data in real-time to a computer. Before each measurement, they are calibrated with a standardised weight, weighing 200 grams, as depicted in Figure 5.2 . With the load information applied to each cell, it is possible then to directly determine the mass of the aircraft and estimate the location of its CM.

Figure 5.1: Experimental measurement of the x and y coordinate of the center of mass.

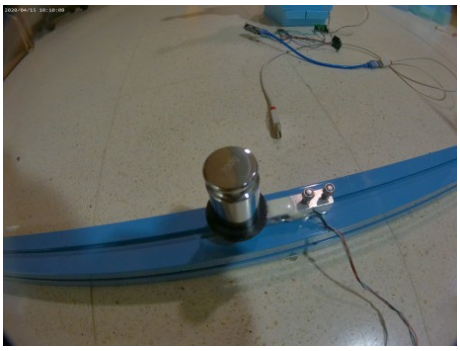

Figure 5.2: Standardised weight and load cell.

We can deduce the location of the CM by doing a static analysis on Figure 5.3 and conclude that the center of mass in relation to the point between the two measuring points F_{N1} and F_{N2} is determined by:

$$X'_{CM} = \frac{(F_{N3} + F_{N4})AC}{F_{N1} + F_{N2} + F_{N3} + F_{N4}} \tag{5.1}$$

$$Y'_{CM} = \frac{F_{N2}AB + F_{N4}CD + (\frac{AB-CD}{2})(F_{N3} + F_{N4})}{F_{N1} + F_{N2} + F_{N3} + F_{N4}} - \frac{AB}{2}\,, \tag{5.2}$$

where F_{N1}, F_{N2}, F_{N3} and F_{N4}, correspond to the load measured in the front right, front left, rear right, rear left part of the landing gear, respectively. AB, CD and AC are the width of the front landing gear, the width of the rear landing gear and the distance between the front and rear landing gears, respectively.

We will then make a translation of this measurement, which is calculated in relation to the first point of measurement, F_{N1}, to get the distance of the center of mass in relation to the generic point of reference used in this project which is the intersection between the geometric plane of symmetry and the leading edge of the UAV main wing:

$$X_{CM} = X'_{CM} - X_{ref} \tag{5.3}$$

$$Y_{CM} = Y'_{CM} - Y_{ref} \tag{5.4}$$

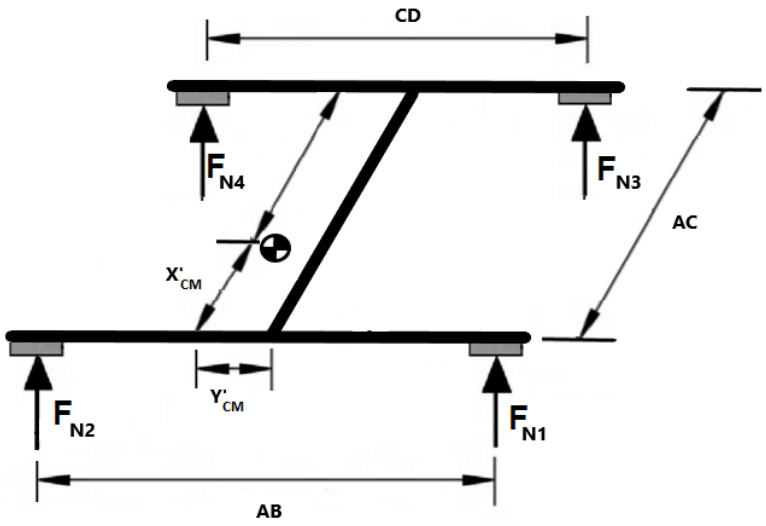

Figure 5.3: Schematic for the measurements of the center of mass

We can use the same procedure to measure the z component of the center of mass by rotating the UAV by 90 degrees and measuring the UAV in the same way with two-points measurement in the wing and two others in the front landing gear, as shown in Figure 5.4. In this case, F_{N1} and F_{N2} correspond to the load measured in left and right sections of the main wing, respectively; and F_{N3} and F_{N4} in the front left and front right part of the landing gear, respectively. AB, CD and AC denote the distance between the two points in the wing, the width of the front landing gear, and the distance between the wing and front landing gear, respectively. In this case, the variable X'_{CM} equals to Z'_{CM}. The results of the experimental measurements of both prototypes with and without fuselage can be found in Table 5.1.

We note that for the F-01 UAV prototype, measurements of the y coordinate were not registered since it was a small deviation from its central line (it was assumed to be zero) and for the z coordinate, no measurements were made. For the F-02, the measurement of the y coordinate is also negligible and so in the computational model of the UAV it is going to be assumed to be zero, while the z coordinate measurement is going to be taken into consideration, especially to see some of the influences of having

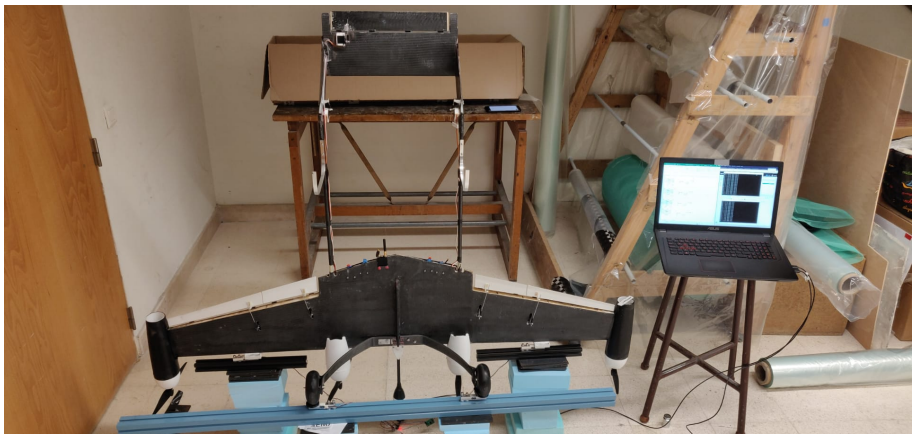

Figure 5.4: Experimental measurement of the z coordinate of the center of mass

Table 5.1: Center of mass location of both prototypes with and without fuselages.

	F-01 without fuselage	F-01 with fuselage	F-02 without fuselage	F-02 with fuselage
Mass [kg]	14.098	15.434	6.409	7.435
X_{CM} [m]	-0.110	-0.110	-0.0938	-0.0890
Y_{CM} [m]	-	-	0.00065	0.00075
Z_{CM} [m]	-	-	0.0025	0.0155

the fuselage attached to the aircraft.

With this information, it is now possible to estimate the static margin of the UAV. For this, a computational model was developed in XFLR5, [29] and we obtain a static margin for F-01 of 4.76% with the fuselage and 4.82% without a fuselage and a static margin for F-02 of 13.44% with the fuselage and 11.66% without a fuselage. We can see that a significant improvement was made in terms of weight, and it was even possible to improve the static margin of the aircraft by moving the x coordinate of the center of mass closer to the leading edge.

5.2 Inertia determination

The method of measuring the moments of inertia of the prototypes, described in [30] [31] was used in this work, which consists of using a suspended structure to allow the free pendulum movement of the aircraft. Thus, the moments of inertia of the model can be obtained by measuring the periods of the pendulum oscillation around the various axes of rotation. Initially, it is necessary to measure the moments of inertia of the support structure with the purpose of subtracting its value from the moment of inertia of the whole system (model + support structure) to obtain the inertial values of the model only.

Thus, it is possible to calculate the moments of inertia of the aircraft according to the expressions 5.5 and 5.6, where the parameters related to the moment of inertia of the structure and the moment of inertia caused by the deviation of the aircraft's center of gravity are subtracted.

$$I_{xx} \quad or \quad I_{yy} = \frac{W' t^2 z}{4\pi^2} - \frac{W'_{struc} t^2_{struc} z_{struc}}{4\pi^2} - \frac{W'_{model} z_{model}}{g} \tag{5.5}$$

$$I_{zz} = \frac{W' t^2 A^2}{16\pi^2 L} - \frac{W'_{struc} t^2_{struc} A^2}{16\pi^2 L} \tag{5.6}$$

In equations 5.5 and 5.6, W' is the total weight of both the aircraft model and the pendulum structure, W'_{model} is the weight of the aircraft model,W'_{struc} is the weight of the aircraft pendulum structure, t is the period of oscillation for both the aircraft model and the pendulum structure, t_{struc} is the period of oscillation for the pendulum structure, L is the length of the two vertical wires separated by a horizontal distance A, z is the vertical distance from the pivot to the center of gravity of the assembly, z_{struc} is the vertical distance from the pivot to the pendulum structure and z_{model} is the vertical distance from the pivot to the center of gravity of the aircraft model.

In Figures 5.5 and 5.6, it is possible to observe the assembly diagram for the measurements of I_{xx} and I_{yy} calculated using formula 5.5. For the measurement of the moment of inertia around the vertical axis, I_{zz}, a bifilar pendulum was used, as illustrated in Figure 5.7, and we used equation 5.6. It is important to note that formulas 5.5 and 5.6 are valid for small oscillation amplitudes, assuming that, $sin(\theta) = \theta$ and $tan(\theta) = \theta$ and assuming no damping due to friction on the rotating hub.

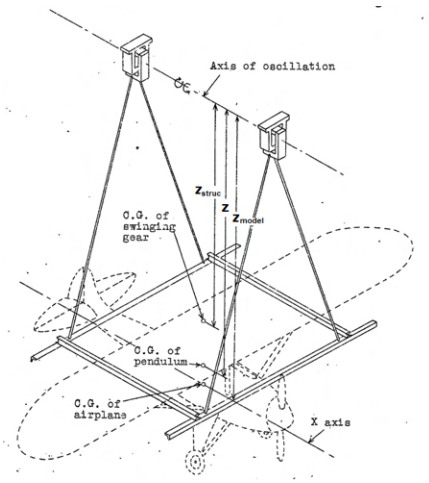

Figure 5.5: schematic of the measurement of the moment of inertia around axis x [31]

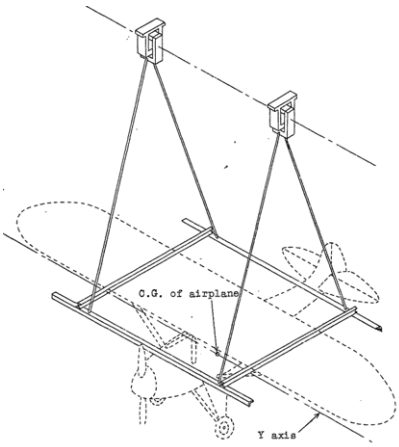

Figure 5.6: schematic of the measurement of the moment of inertia around axis y [31]

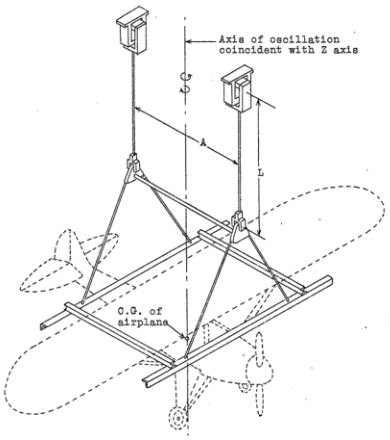

Figure 5.7: schematic of the measurement of the moment of inertia around axis z [31]

As a test to this experimental setup, the inertia properties were estimated for two bars, one made of aluminium [$1m \times 0.015m \times 0.015m$] and another made of wood [$1m \times 0.073m \times 0.073m$]. Assuming a homogeneous bar with a defined mass (m_{bar}), length (l), width (w), height (h) the inertia can be defined as:

$$I_{xx} = \frac{1}{12} m_{bar}(w^2 + h^2) \tag{5.7}$$

$$I_{yy} = \frac{1}{12} m_{bar}(l^2 + h^2) \tag{5.8}$$

$$I_{zz} = \frac{1}{12} m_{bar}(w^2 + l^2)\ . \tag{5.9}$$

It is worth noting that although the dimensions of the pendulum are somewhat governed by the dimensions of the UAV in question, it is important to keep the pendulum as short as possible so that the moment of inertia of the aeroplane about an axis through its center of gravity will be a large percentage of the total moment of inertia of the pendulum about the axis of oscillation. At the same time, the setup should have a period of oscillation reasonable to be measured, in this case, with a digital stopwatch. After several tries with the metal and wood bar, it was determined that 0.442 meters was an adequate length for the pendulum used to estimate the pitch and roll moment of inertia. It should be noted that, for the roll motion of the pendulum, the inertia of the bars are just too small to be measured using this setup leading to large errors, as shown in the table 5.2.

For the case of the bifilar pendulum it was found, as it noted in [31], that the results were more accurate when L is approximately equal to or greater to A. With this setups, we achieved the following errors of each of the oscillations:

Table 5.2: Inertia moments of test bars

		$I_{theoretical}$ [kgm^2]	I [kgm^2]	Error
Metal bar	Pitch	0.0542	0.0511	6.079%
	Roll	0.0051	0.0000230	22315%
	Yaw	0.0449	0.0511	12.028%
Wood bar	Pitch	0.3483	0.3742	6.899%
	Roll	-0.01223	0.0024	606%
	Yaw	0.3525	0.3742	5.794%

In addition, the precision of the measurement of the length of the compound pendulum depends primarily upon the accurate location of the center of gravity of the aeroplane. If it is not located accurately, the pendulum measurements will have an error even though subsequent measurements are very precise. This emphasises the necessity for extreme care in locating and checking the position of the center of gravity.

Furthermore, an accurate measurement of the period of oscillation can be found without significant difficulties by making an average of several measurements of several complete oscillations, having the required precision by using a simple stopwatch to make the observations. For future work and projects, it is suggested that a more permanent and adaptable rig solution should be built since it is a measurement of interest for all UAVs.

And so, we were able to collect, with an acceptable degree of confidence, the same data for F-02 with

and without the fuselage in tables 5.4 and 5.3, respectively. The inertia parameters were not measured for F-01 because of time constraints imposed by factors outside of the control of the author, and so those cannot be shown in this work, the data used can be seen in Appendix A.2.

Table 5.3: Inertia moments of F-02 without fuselage.

		W [kgf]	A [m]	L [m]	z_{struct} [m]	z_{model} [m]	z [m]	I [kgm^2]
Structure	Pitch	1.497	-	-	0.4420	-	0.4420	0.26572
	Roll	1.497	-	-	0.4420	-	0.4420	0.26572
	Yaw	1.479	0.4030	0.4070	-	-	-	0.06994
Structure + UAV	Pitch	7.906	-	-	0.4420	0.5020	0.4903	1.42704
	Rol	7.906	-	-	0.4420	0.5020	0.4903	1.66843
	Yaw	7.906	0.4030	0.4070	-	-	-	2.41820
UAV	Pitch	6.409	-	-	0.4420	0.5020	0.4903	0.23943
	Roll	6.409	-	-	0.4420	0.5020	0.4093	0.80318
	Yaw	6.409	0.4030	0.4070	-	-	-	1.07047

Table 5.4: Inertia moments of F-02 with the fuselage.

		W [kgf]	A [m]	L [m]	z_{struct} [m]	z_{model} [m]	z [m]	I [kgm^2]
Structure	Pitch	1.497	-	-	0.409	-	0.442	0.26572
	Roll	1.497	-	-	0.409	-	0.442	0.26572
	Yaw	1.479	0.403	0.407	-	-	-	0.06994
Structure + UAV	Pitch	8.932	-	-	0.409	0.5020	0.4903	2.56179
	Rol	8.932	-	-	0.409	0.5020	0.4903	1.65446
	Yaw	8.932	0.403	0.407	-	-	-	2.30589
UAV	Pitch	7.435	-	-	0.409	0.5020	0.4903	0.32795
	Roll	7.435	-	-	0.409	0.5020	0.4903	0.81817
	Yaw	7.435	0.403	0.407	-	-	-	1.10740

Additionally, since the aircraft has a plane of symmetry, the products of inertia I_{xy} and I_{yz} can be neglected. The product of inertia I_{xz} follows a similar procedure to the one used for the determination of the moment of inertia around I_{xx}. For the XZ-axis suspension, an inclined axis in the XZ–plane is made parallel to the oscillation axis by adding short tie rods to either the front or rear members so that the new plane is rotated about the Y-axis, as shown in Figure 5.8. The angle of inclination of the X-axis is measured using:

$$I_{xz} = \frac{I_{xx}\cos^2\theta + I_{zz}\sin^2\theta - I'_{xx}}{\sin 2\theta} \ , \tag{5.10}$$

where I'_{xx} is the moment of inertia measured around the inclined axis in the XZ–plane. Finally, the data is presented for the F-02 UAV for a measured inclination of $19\,\mathrm{deg}$ and $-20\,\mathrm{deg}$, in Table 5.5 and 5.6, obtaining an average value equal to 0.0238 kgm^2 without fuselage and 0.0275 kgm^2 with fuselage. This concludes the set of experimental measurements intended to measure the necessary inertia parameters.

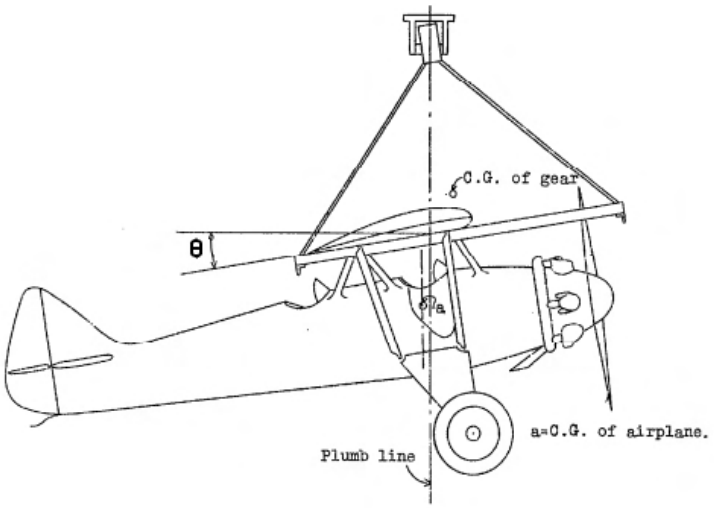

Figure 5.8: schematic of the measurement of the moment of inertia around inclined axis in the XZ–plane

Table 5.5: Product of inertia I_{xz} of F-02 without fuselage.

		W [kgf]	z_{struct} [m]	z_{model} [m]	z [m]	I'_{xx} $[kgm^2]$
Structure	Roll (+19deg)	1.497	0.432	0.492	0.480	0.2791
	Roll (-20deg)	1.497	0.432	0.492	0.480	0.2791
Structure + UAV	Roll (+19deg)	7.906	0.432	0.492	0.480	2.6337
	Roll (-20deg)	7.906	0.432	0.492	0.480	2.6569
UAV	Roll (+19deg)	6.409	0.432	0.492	0.480	0.7964
	Roll (-20deg)	6.409	0.432	0.492	0.480	0.8296
		W [kgf]	z_{struct}	z_{model}	z [m]	I_{xz} $[kgm^2]$
UAV	Roll (+19deg)	6.409	0.432	0.492	0.480	0.0258
	Roll (-20deg)	6.409	0.432	0.492	0.480	0.0219

Table 5.6: Product of inertia I_{xz} of F-02 with the fuselage.

		W [kg]	z_{struct} [m]	z_{model} [m]	z [m]	I'_{xx} $[kgm^2]$
Structure	Roll (+19deg)	1.497	0.432	0.492	0.480	0.2791
	Roll (-20deg)	1.497	0.432	0.492	0.480	0.2791
Structure + UAV	Roll (+19deg)	8.932	0.432	0.492	0.480	2.9823
	Roll (-20deg)	8.932	0.432	0.492	0.480	3.0349
UAV	Roll (+19deg)	7.435	0.432	0.492	0.480	0.8109
	Roll (-20deg)	7.435	0.432	0.492	0.480	0.8488
		W [kg]	z_{struct}	z_{model}	z [m]	I_{xz} $[kgm^2]$
UAV	Roll (+19deg)	7.435	0.432	0.492	0.480	0.0305
	Roll (-20deg)	7.435	0.432	0.492	0.480	0.0245

5.3 Brushless motor tests

The propulsive tests aim to characterise the behaviour of the motor that includes the electric motor, ESC and the propeller. In this case, different propellers will be tested to choose the best available propeller for the case in hand. The propulsion system was installed on a test bench (see Figure 5.9), and an external structure of the test bench was designed to accommodate the acquired test bench (from RCbenchmark) in the right place in the wind tunnel. The test bench includes several load cells

to measure the forces and moments generated and an optical sensor to measure the motor rotational speed.

The test bench is then connected to a battery and to a computer, which controls the signal sent to the ESC that controls the speed of the motor and acquires the data from the load cells and optical sensor. Finally, since the wind tunnel is already calibrated, we can know the relation between the rotations per minute (RPM) at which the wind tunnel's propeller rotates (which is the input we can control) and the speed of the flow that approaches our electric motor and the test setup. This relation is given in the table 5.7.

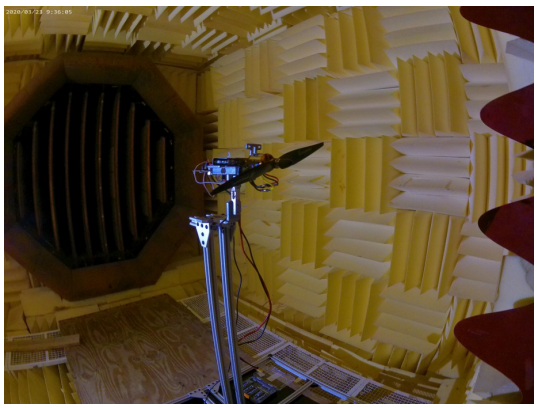

Figure 5.9: Propulsive test bench in the IST acoustic wind tunnel

Table 5.7: Relation between the rotational speed of the Wind tunnel propeller in RPM and its airflow velocity in m/s.

Wind Tunnel Motor (RPM)	Airflow speed (m/s)
150	6.6
222	10.01
331	15.02
439	20.00
549	25.02
658	30.01

Three sets of propellers were recommended by the chosen motor manufacturer, identified by their diameter and pitch: 11x5; 12x6; and 13x8. The axis that is considered here is the same as the one used for the UAV model, x-axis forward, z-axis downwards and y following the right-hand rule. For these tests, the RCbenchmark software was used. The tests were carried out following the recommendations provided by RCbenchmark and so the ESC input signal is gradually increased up to almost the limit of the current intensity allowed by the ESC (50 A). In each step, a settling time of 3 seconds is used to achieve the rotor's static response, and a sample of 100 measurements is averaged to achieve our final result for the conditions in question. Each condition will then be determined by an ESC input signal (μs) and an incoming airflow provided by the air tunnel, shown in the Table 5.7. The procedure is repeated for each propeller.

With this test setup, several parameters can be measured and recorded, including voltage (V), current intensity (A), torque (Nm), vibrations (g), revolutions per minute (RPM), ESC signal (μs) and time (s).

With these measurements, several parameters can be calculated, such as Electrical Power ($W = VA$), Thrust Coefficient with equation 2.22, Power Coefficient with equation 2.23 and Advance Ratio with equation 2.21. These results were then used to build the propulsion system model and the results can be observed in Tables 5.8, 5.9 and 5.10 for propeller 13x8 and Appendix A.3 for all propellers.

Table 5.8: Rotor Static Thrust Response measured of the propeller 13x8.

Thrust(kgf) 13x8	Incoming Airflow Velocity (m/s)						
PWM(μs)	0.00	6.60	10.01	15.02	20.00	25.02	30.10
1000	0	-0.06787	-0.1013	-0.1373	-0.1886	-0.2288	-0.2828
1100	0.15296	0.086007	0.027432	-0.038081	-0.10351	-0.16205	-0.23056
1189	0.37428	0.23988	0.15613	0.061122	-0.01841	-0.095267	-0.17832
1278	0.6077	0.40637	0.29824	0.18314	0.075412	-0.025235	-0.12134
1367	0.82388	0.59912	0.47314	0.32205	0.18519	0.055236	-0.055823
1456	1.0397	0.81368	0.65854	0.47105	0.30247	0.14637	0.016291
1544	1.2246	0.99442	0.82783	0.61385	0.42985	0.24056	0.080475
1633	1.4419	1.2075	1.0164	0.77999	0.55413	0.33531	0.14939
1722	1.6777	1.4398	1.2493	0.99685	0.73471	0.45371	0.21315
1811	1.898	1.6557	1.4633	1.2002	0.93945	0.64595	0.30588
1900	2.1055	1.8623	1.6535	1.3568	1.0916	0.77754	0.28454

Table 5.9: Rotor Static Torque Response measured of the propeller 13x8.

Torque (Nm) 13x8	Incoming Airflow Velocity (m/s)						
PWM(μs)	0.00	6.60	10.01	15.02	20.00	25.02	30.10
1000	0	-0.01252	-0.02107	-0.02426	-0.02697	-0.02436	-0.02429
1100	0.036353	0.03439	0.024656	0.014415	0.0052805	-0.0011942	-0.0068808
1189	0.079641	0.081304	0.070379	0.053093	0.037533	0.021973	0.010532
1278	0.12291	0.12681	0.11519	0.096407	0.076223	0.053532	0.034801
1367	0.16649	0.17122	0.16291	0.14399	0.11919	0.090521	0.061248
1456	0.21149	0.21859	0.20985	0.18935	0.16173	0.12738	0.092174
1544	0.24976	0.25918	0.25197	0.23158	0.20309	0.16358	0.11979
1633	0.29439	0.3057	0.29764	0.2783	0.24347	0.19751	0.14797
1722	0.34327	0.35758	0.35331	0.33623	0.29949	0.23821	0.17395
1811	0.39074	0.40573	0.40382	0.3903	0.3615	0.30294	0.20905
1900	0.43588	0.45238	0.45019	0.43279	0.40421	0.34685	0.19924

Table 5.10: Rotor Static Electrical Power Response measured of the propeller 13x8.

Power (Watt) 13x8	Incoming Airflow Velocity (m/s)						
PWM(μs)	0.00	6.60	10.01	15.02	20.00	25.02	30.10
1000	0	0	0	0	0	0	0
1100	21.4672	19.9531	19.2394	16.8646	14.5043	12.2982	10.0494
1189	56.6002	54.4286	51.3402	45.6742	41.2333	34.2203	28.0516
1278	98.2824	95.7419	90.2141	84.109	75.9916	63.9796	51.756
1367	148.214	142.9421	138.8774	130.1416	116.963	100.1281	80.8096
1456	202.9577	198.8391	191.3995	177.9878	161.5161	139.427	113.9781
1544	254.2345	248.2563	240.7791	226.2572	207.9063	178.8974	145.1783
1633	312.0449	310.4816	298.0831	280.7677	253.8412	218.4812	175.7908
1722	382.5936	382.4213	371.6216	353.7039	318.8438	263.9148	204.2415
1811	451.001	452.3811	442.5443	426.6805	396.4776	340.3274	242.85
1900	526.0878	528.9071	514.1841	490.0816	458.9158	396.0695	227.5342

5.3.1 Rotor transient response

One other aspect we want to study in this section is the time response of the rotor. To do so, we study the response to step inputs and, with this information, we can model its transient response to possible first order system candidates.

By analysing the time response, we can observe that the rotor has different behaviour when the step response starts from a zero rotational speed than it has during high speed operation; this observation

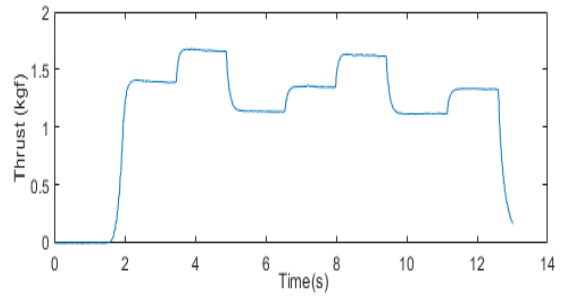

Figure 5.10: Rotor Thrust Transient Response output

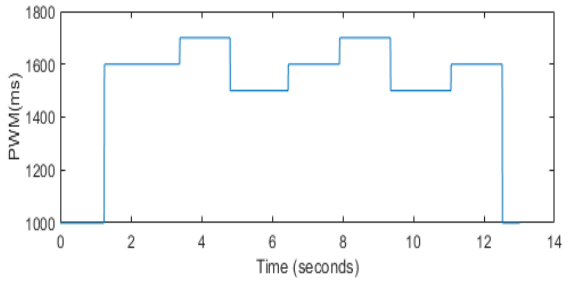

Figure 5.11: Rotor Thrust Transient Response input

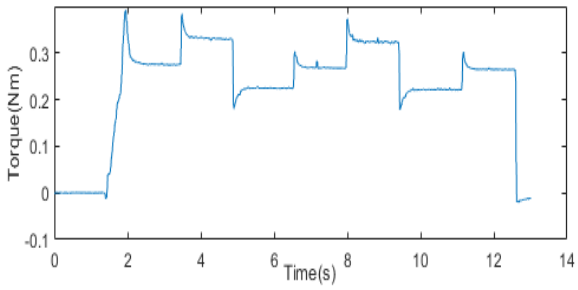

Figure 5.12: Rotor Torque Transient Response output

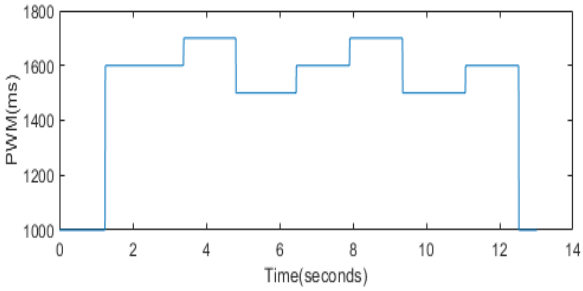

Figure 5.13: Rotor Torque Transient Response input

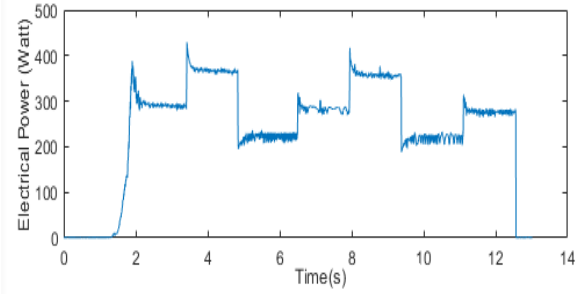

Figure 5.14: Rotor Electrical Power Transient Response output

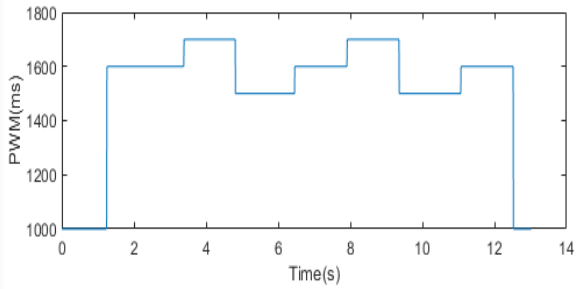

Figure 5.15: Rotor Electrical Power Transient Response input

is supported by [32]. We assume that the aircraft will not enter this region during flight, which is a reasonable assumption for the model in question.

Furthermore, it is observed that the thrust time response is clearly different from the torque and electric power time response, which have faster responses with a clear spike or possible overshoot with no fluctuations afterwards. Therefore, we concluded that it represents a non-linearity that our simple first degree system can not model. Lastly, since in our system we do not have a constant voltage input, due to the battery voltage drop caused by discharge during operation, we observed a decline in every output as the battery discharges for the same input. These phenomenon can be observed in Figures 5.16 (a),(b),(c).

The dynamics of the battery are not modelled and it is assumed as a disturbance to the system in question. Using the System Identification Toolbox of MATLAB, the data was selected for a range where

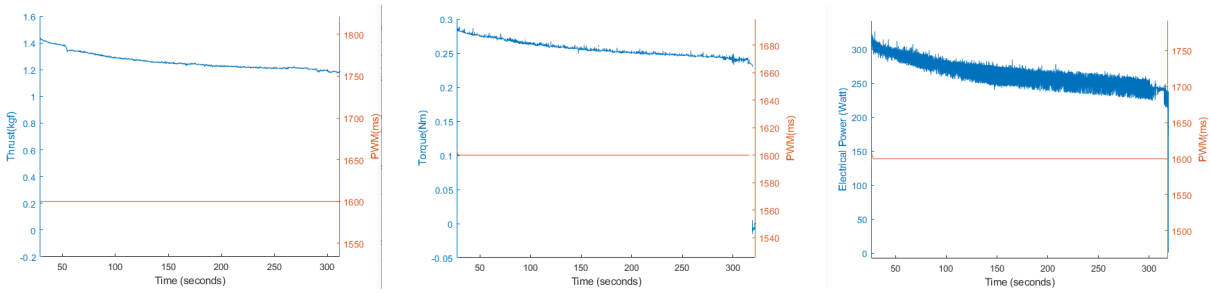

(a) (b) (c)

Figure 5.16: Rotor Response in a large time interval (a) Thrust, (b) Torque and (c) Electrical Power measured of the propeller 13x8.

the low rotational speed is eliminated since we do not want to model that region. The median value was then subtracted to model a linear model in this region and two candidates were assumed as appropriate candidates: a first order system with no delay and a first order system with a delay (since they were a good compromise between accuracy and simplicity), thus achieving the following results given in figures 5.17, 5.18, 5.19 and table 5.11.

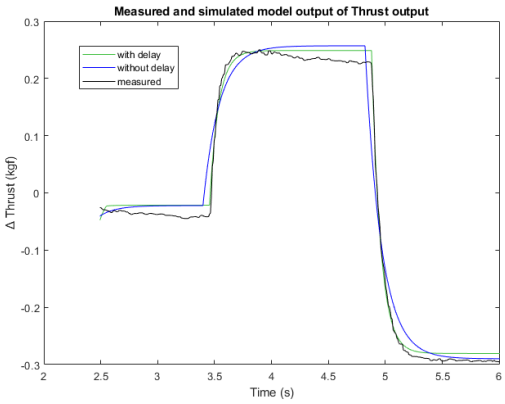

Figure 5.17: Rotor Modelled Thrust Transient Response versus Measured

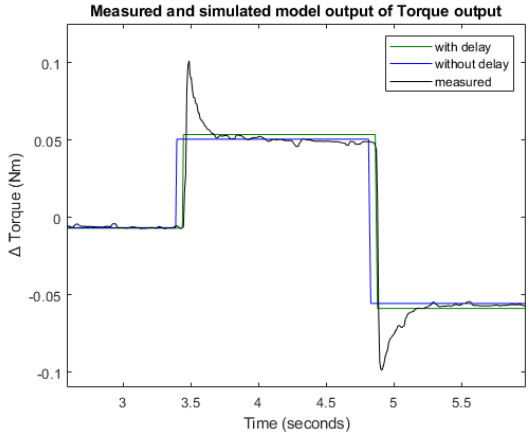

Figure 5.18: Rotor Modelled Torque Transient Response versus Measured

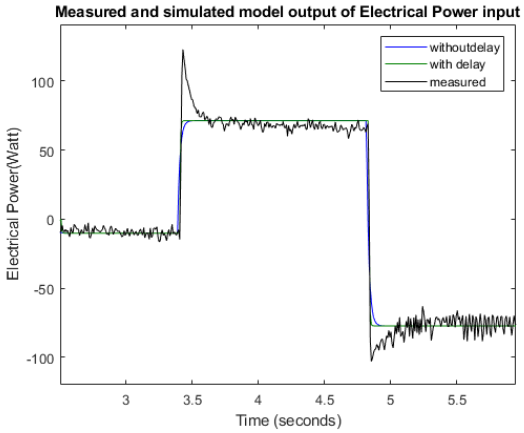

Figure 5.19: Rotor Modelled Electrical Power Transient Response versus Measured

Thrust Model		Thrust Model	
Pole	-7.032	Pole	-12.81
Static Gain	1	Static Gain	1
delay	0 s	delay	0.0576 s
Torque Model		Torque Model	
Pole	-1433	Pole	-3527
Static Gain	1	Static Gain	1
delay	0 s	delay	0.0494 s
Electrical Power Input Model		Electrical Power Input Model	
Pole	-58.28	Pole	-258.6
Static Gain	1	Static Gain	1
delay	0 s	delay	0.0165 s

Table 5.11: First Order Model of the Time Response of the Rotor output

With these results and making some assumptions to simplify our model, we come to the results in Table 5.12; The assumptions were the following:

1. The rotor only works in high rotational speeds.

2. Battery discharged voltage is not modelled.

3. The existence of four rotors; two on each side of the wing, makes it possible to achieve at all times a zero net torque, resulting from the sum of the torque produced at the rotors acting on the center of mass, by setting the rotors to rotate in pairs. With this in mind, we simplify the transient model to an instantaneous response, since we do not except to have a significant influence in the overall behaviour of the UAV.

4. The main focus of calculating the Electric Power of each rotor is to give a rough estimation of the available flight time at each speed, and so we simplify the transient response to an instantaneous one and add a safety factor to the time available for the flight tests duration.

Table 5.12: Final Models of the Time Response of the Rotor output

Thrust Model		Torque Model		Electrical Power Model	
Pole	-12.81	Pole	-	Pole	-
Time Constant	0.078	Time Constant	-	Time Constant	-
Static Gain	1	Static Gain	1	Static Gain	1
delay	0.0576 s	delay	0	delay	0

The time constant, can be calculated by using the inverse value of the pole for a first order system and for future works, a completed model should be built using for example [32] as a reference.

5.4 Ground Vibration Tests

The dynamic structural tests, also known as ground vibration tests, were carried out in IST under the supervision of Prof. Hugo Policarpo. These tests are used to analyse and test the dynamic behaviour of the structure by determining its vibration modes and corresponding frequencies. Also, it is possible to have a first impression if any critical section of the UAV needs any reinforcement or additional attention.

In order to simulate a condition closer to that which the UAV will encounter in flight (that is, in a free-flight situation), the support system was suspended by ropes, as shown in Figure 5.20. The vibration modes were excited by means of a shaker (see Figure 5.20). In the case of the F-02 UAV, two experiments were conducted using in each experiment nine measurement points (note that the point of application of the force, in this case the shaker, is at point 3 of Table 5.13 and Figure 5.22). At these points, uniaxial accelerometers were connected by cables to the data acquisition system. This system was connected to a portable computer, transferring the signal data for later post-processing, as shown in Figure 5.21.

Figure 5.20: Experimental setup of the vibration tests

Figure 5.21: PCB 208 C01 force transducer

The signal processing was carried out in a frequency range between 0 and 200 Hz, with a frequency step of 0.125 HZ, with and without fuselage. In the course of these tests, it was possible to see that every electronic component was well fixed to the structure and no incident was reported.

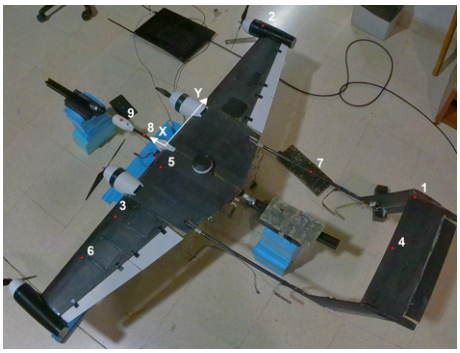

Figure 5.22: Measurement points ilustrated in the F-01 UAV

	Coordinates(m)	
Point	X	Y
1	-0.84	18.5
2	0	0.75
3	-0.04	-0.34
4	-0.84	0
5	-0.04	-0.155
6	-0.03	-0.515
7	-0.50	0.205
8	0.26	0
9	0.075	0

Table 5.13: Excitation (3) and response (1-9) points, coordinates used to obtain the experimental data.

The Frequency Response Function (FRF) from all sensors can be observed for the UAV without fuselage in Figure 5.23, and with fuselage in Figure 5.24.

It can be clearly observed the two first modes of vibration at 5.125 Hz and 8.25 Hz without a fuselage, and at 5.125 Hz and 8.00 Hz with a fuselage. These two modes are essential vibration modes in terms of control since they should not be excited by the natural frequency of any dynamic behaviour of the aircraft so as not to have a resonance that could cause damage to the structure and subsequently losing the aircraft during flight.

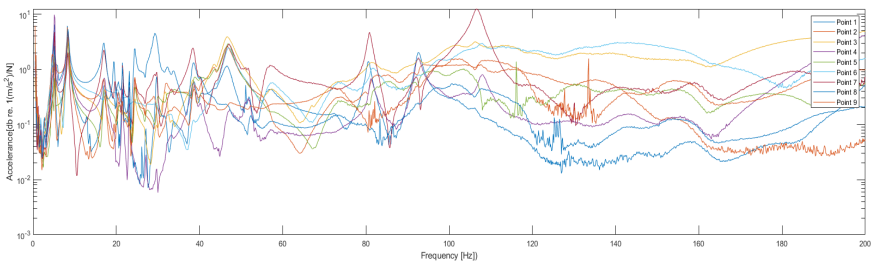

Figure 5.23: FRF's of the 9 measured points [0 – 200Hz], excited by a shaker without a fuselage

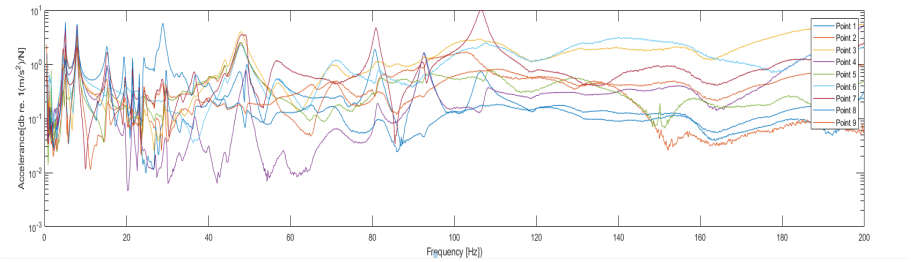

Figure 5.24: FRF's of the 9 measured points [0 – 200Hz], excited by a shaker with a fuselage

Additionally, during the tests, the booms connecting the main wing and the tail were observed to oscillate at a higher amplitude and at a lower frequency than the remaining parts of the structure. This was also observed for the F-01. For these reasons, we are led to believe that the bending of the booms is somehow part of the first vibration mode shape. However, without using a proper numerical method to identify the mode shapes, which was out of the scope of this thesis, it is not possible to say for sure.

Furthermore, two tests were conducted, where the vibration modes were excited by the motion of propellers at two different rotational speeds, 2100 RPM and 3900 RPM, to investigate if the propellers would excite the structure, especially the first two vibration modes in any critical way. The FRF that results from this experiment can be seen in the following Figures 5.25 and 5.26:

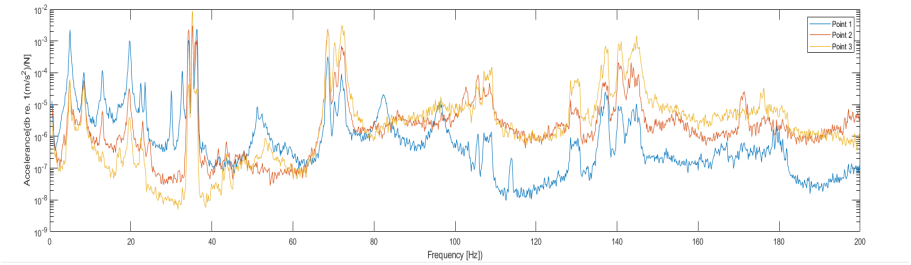

Figure 5.25: FRF's of the 9 measured points [0 – 200Hz], with a propeller rotational speed of 2100 RPM

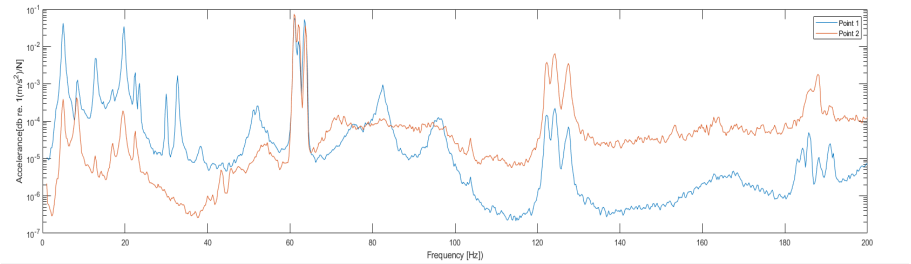

Figure 5.26: FRF's of the 9 measured points [0 – 200Hz], with a propeller rotational speed of 3750 RPM

We are able to see that it does excite the first two nodes of the structures, but it does not put the structure in any danger. We can also see the spikes related to the speed at which the propellers are spinning for the first test in Figure 5.25, around 35 Hz, 70 Hz and 140 Hz, and for the second test in Figure 5.26, around 62.5 Hz, 125 Hz. Although higher rotational speed could have been used to test for more flight conditions, for safety reasons, it was decided not to do so.

F-01 Vibration Tests Results

For the F-01 UAV, similar tests were conducted and the first 10 modes of vibration were determined with the aluminium inner structure only, as shown in Table 5.14, in terms of frequency and damping factor. It was initially planned to carry out new tests after the UAV was fully assembled and instrumented, with and without fuselage. However, due to time constraints, it was decided to proceed with the tests on the airfield at the expense of new vibration tests.

While on the F-02 only the two first frequencies are identified, in the F-01 more sensors and other software was used to give a broader analysis since there was a more focused approach to the structural aspects of the UAV.

Table 5.14: First ten modes of vibration for F-01.

Vibration Mode	Natural Frequency[Hz]	Damping Factor
1	8.26	0.85
2	13.03	0.82
3	21.83	1.84
4	26.09	2.422
5	33.58	1.73
6	36.63	1.58
7	37.44	1.88
8	43.04	2.38
9	52.04	3.53
10	60.88	2.46

From these tests, it was possible to identify a similar critical point in the structure, namely the connection between the wing and the tail. It is possible to compare the two first vibration modes and observe a decrease in their frequency, most likely related to its thinner carbon tubes used in the connection between the wing and the tail necessary to comply with the new philosophy of making the tail as light as possible, necessary to have a viable static margin without the need to add an excessive unnecessary weight to the leading edge as it was done in F-01.

5.5 Flight tests

In this section, we present the result from the flight executed with F-02 UAV. Due to time constraints in this project and with the availability of the pilot, unfortunately only one flight was possible to be conducted. Note that there was an attempt to fly the F-01 UAV that was found to be unsuccessful to achieve take-off.

The flight path recorded can be observed in Figure 5.27. The flight duration was of 2.5 minutes consuming about 40 % of the battery capacity, the pilot has flown the aircraft always in his field of vision around the flattened clay airfield. With the data recorded from the flight, we can estimate to have flown at around 25.28 m/s after climbing to a safe altitude. This estimation comes from the median value registered from the GPS speed while the UAV was performing circular turns. The data from this segment of the flight can be observed in Figure 5.29, just after a climbing phase and before landing.

Figure 5.27: Flight path measured during the first flight.

Figure 5.28: F-02 first flight

The flight unfortunately did not perform as it was intended and it was not possible to trim the aircraft in any phase of the flight. From the pilot feedback, the aircraft did not show longitudinal stability and the elevator input needed to be continuously modified in order to prevent the UAV from stalling. That trend can be seen in Figure 5.30. Additionally, when the aircraft approached the airfield and its speed was reduced in order to land, the longitudinal stability decreased even further, resulting in a rough landing, that fortunately caused minor damages. Nevertheless, one can see that lower inputs were needed to achieve lateral control in Figure 5.31.

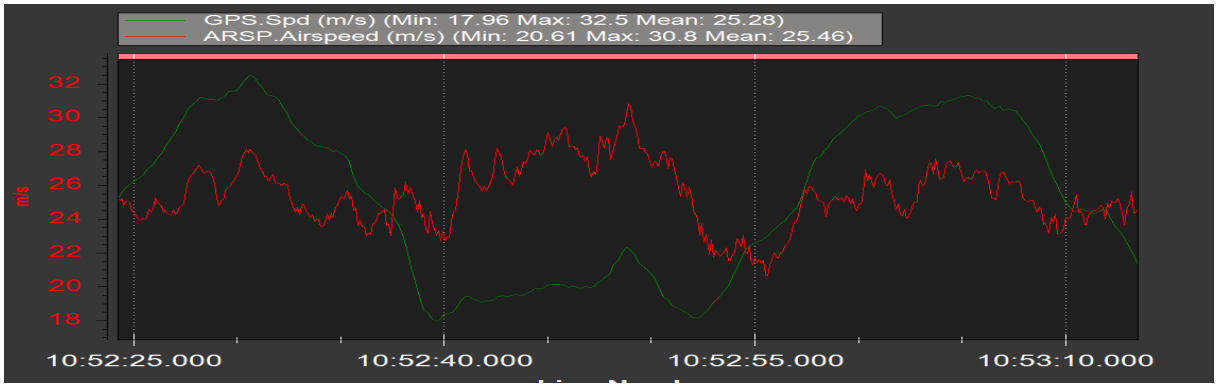

Figure 5.29: Flight data: Airspeed and Ground Speed during cruise.

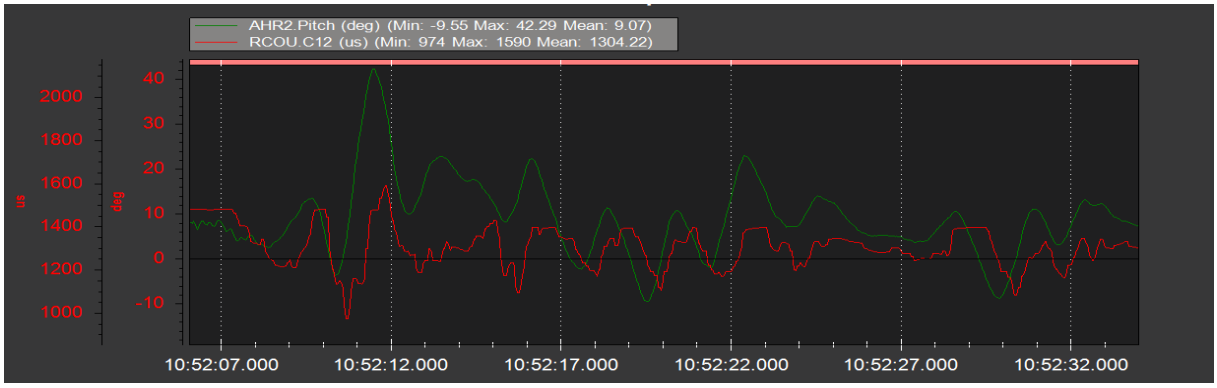

Figure 5.30: Flight data: Pitch angle and Elevator input signal (RCOU.C12), from take-off to cruise.

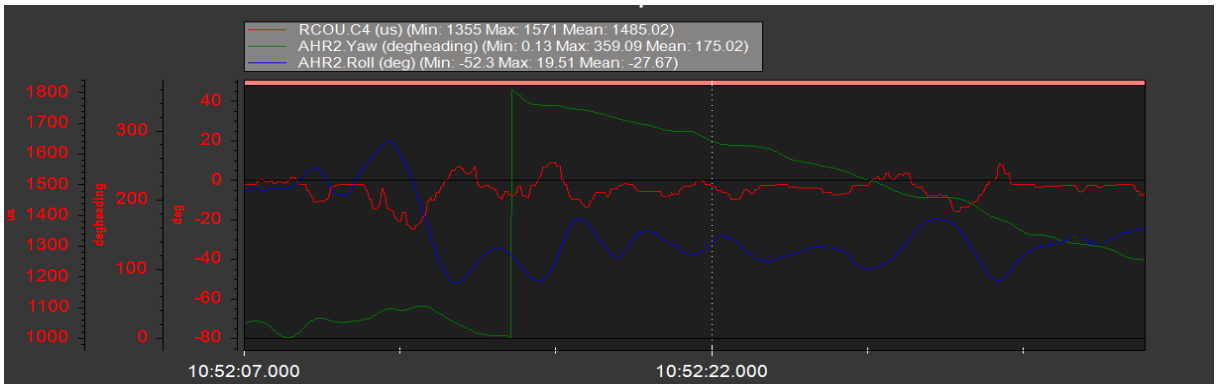

Figure 5.31: Flight data: Yaw, Roll angles and Right Aileron input signal(RCOU.C4) from take-off to cruise.

Chapter 6

Conclusions

During the execution of the thesis and project, several of the defined tasks were achieved with different degrees of success. While in the beginning, the objectives of the thesis were reserved only to design and elaborate a control algorithm that could provide an improvement on the performance of the aircraft, that rapidly was adopted due to the difficulties encountered with the construction of this type of aircraft configuration that could also fly with and without a fuselage. Taking that into consideration, considerable time and work was reserved for making improvements and iterations to arrive at the final version of the scaled UAV. We can conclude the main goal was achieved by constructing the F-02 UAV, a test platform that could fly, in order to retrieve data about its flight characteristics that could be used to validate a control algorithm. That being said, smaller improvements still need to be done to the tail structure to increase the structural rigidity of this structure to test what we think is the most probable hypothesis to explain the lack of stability during the flight. With this improvement, other tasks can be tested and completed.

The main reason to build this scaled aircraft was to draw some conclusions about the viability of this configuration for the specified mission, in that account, we have to come to terms that there is a need to revise or even change the aircraft configuration. The main drawback, from the current choice, comes down to the struggle to position the center of mass without adding a lot of dead weight on the foreside of the wing or reducing so much weight on the tail structure that it compromises its rigidity. This problem comes from the specificitions of the proposed mission, which forces the possibility of a flight without a fuselage. Usually, the existence of a fuselage helps to position the center of mass in a place that provides greater stability by positioning the wing and tail along the fuselage in an advantageous way. The reality of this configuration is that it does not provide a zone where heavier components can be placed with enough moment arm to push the center of mass to the right place to fly without a fuselage. A possible solution to this problem may be found in changing the configuration to a tandem wing, which does not come without its own issues; still, it definitely gives more freedom when it comes to the center of mass location with or without the fuselage. This is actually one of the proposals in the report [10] produced by all of the stakeholders in this project. On the other hand, the experience acquired in UAV construction, avionics, design and piloting was very enriching and will definitely be used in any future

projects in this area, so we definitely suggest that the fourth goal was achieved with success.

To accomplish the second goal of building a computational model of the scaled model, a MATLAB/SIMULINK model was made, containing the aircraft forces, moments, navigation, and cinematic differential equations. The first task accomplished in this section was achieved by creating a dynamics model assuming rigid body dynamics, where all forces and moments acted. The main forces and moments affecting the aircraft dynamics can be divided into three different classes - gravity, propeller and aerodynamics - according to their nature.

The aerodynamic forces and moments are modelled by their aerodynamic coefficient, and they can only provide reliable results in the linear region of the curves that describe the coefficients as a function of the aerodynamic angles, resulting in aerodynamic derivatives. These coefficients are estimated using computational tools, in this case, the XFLR5 software. Unfortunately, no wind tunnel with the necessary equipment was available to validate these values. The rotor model consists of two sections, a calculated static response measured in the IST wind tunnel for each propeller with two inputs, the input signal and the velocity of the incoming airflow and a transient response that consists of a first-order dynamic with a delay for the thrust and an instantaneous transient response for the power and torque. The power is also integrated to calculate the energy consumed and remaining. The kinematic equations relate the aircraft and inertial reference frame, making navigation possible, which is based on a NED system. To complement the model, the actuators dynamics are included by imposing a rate limit and deflection limits.

With the computational model, it is possible to test several missions and flight conditions, while at the same time several controllers can be tested to improve the performance of the aircraft in question that can also be altered to future UAV's to be analyzed. Since all this can be done in simulation a considerable amount of flight test time and costs can be reduced.

The last goal was partially accomplished. While a control algorithm is designed, it is still a simple control, and there is still much work to be done in this area. To achieve this control, trimming and linearization of the nonlinear equations are necessary to calculate the state-space matrices. This dynamic matrix analysis shows that the longitudinal and lateral modes are decoupled, reducing the model complexity. Also, the longitudinal and lateral modes are stable, and the only exception is the spiral model that is usually unstable.

Controller model was initially based on the Pixhawk structure but since some aspects of this controller made it difficult to stabilize the aircraft and so we propose a classical controller that uses a cascaded-loop architecture with three inner P-only loops with feedback of the angular rates p,q,r to stabilise the UAV, and two outer PI loops to control the θ and ϕ orientation angles, making compatible with the existing position controllers with the possibility of using gain scheduling.

Gains of said controller are based on the aircraft linear state space model, for each trimming velocity and then analysed in closed loop with root-locus graphical techniques for the inner loops. For the outer loop the MATLAB routine, *systune*, is used on the linearized system and by defining two goals, to reach a certain phase and gain margin, and also to have a certain time response we arrive at the final gain-scheduled gains for the controller. In the end the controller did not achieved a desirable fast time

response and work still has to be done to improve this controller. Additionally, a position controller still needs to be done to provide autonomous flight capabilities.

Finally, several experimental tests were performed to measure several parameters directly on the UAV. Inertia tests were performed with success with the construction of a test rig with this in mind, and the inertia matrix was obtained with the fuselage and without it, assuming symmetry on the xz axis which leads to I_{xy} and I_{zy} to be negligible. Another parameter measured was the location of the center of mass with the use of several load cells, which is an essential parameter to assure stability. Furthermore, with the acquisition of a propulsion test rig and the use of the wind tunnel in IST, the behaviour of the UAV was modelled with success. A more sophisticated model should be developed, such as the one in [32], but it is outside of the scope of this work. Ground vibration tests were also performed with success in two UAV's with the measurement of the vibration modes, which when comparing the two UAV's, it was found that the frequency of the first two modes of vibration decreased in the F-02 case. Lastly, a flight was performed. It was found that the longitudinal modes were most likely unstable from the pilot input and the data recorded, with a high work load from the pilot to maintain a levelled flight and a rough landing with an uncontrolled aircraft right before touch down at lower velocities.

6.1 Future Work

This last subsection will mention some proposals for future work to obtain better results in this project:

1. First of all, increase the rigidity of the tail structure to improve flight qualities. One way of doing this is by adding rigging wires to the structure.

2. Estimate the computational model parameters again, this time based on flight data obtained from remotely piloted flights, to validate the obtained computational model by performing experimental fight tests in an open loop.

3. With these tasks accomplished, improve the controller model of the PID loops, correct the control strategies for the new estimated parameters and check the non-linear model behaviour in the presence of wind and wind gusts.

4. Upload the controller to the Pixhawk board, and test it in an actual flight.

In addition, some recommendations are made for similar projects that may be elaborated in the future:

1. Start by building and testing the aircraft configuration for the mission selected, with more accessible and faster UAV constructions techniques and materials, like foamboard construction or XPS foam and only after this phase is completed, a final and more complex UAV should be built.

2. Improve the computational model by improving each subsystem individually and include other subsystems that could be helpful, for example, to simulate VTOL operations.

3. Build definitive test rigs for parameter estimation that can be easily adapted to several UAV types and sizes.

4. Learn how to fly RC planes, which can be very helpful in this industry and facilitate the flight test arrangements and it is actually a pretty interesting and useful hobby.

Bibliography

[1] Airbus. Modal analysis and experimental validation. URL https://www.airbus.com/newsroom/press-releases/en/2020/09/airbus-reveals-new-zeroemission-concept-aircraft.html. Last accessed: 2020-11-29.

[2] B. Brelje and J. Martins. Electric, hybrid, and turboelectric fixed-wing aircraft: A review of concepts, models, and design approaches. *Progress in Aerospace Sciences*, 104:1–19, 01 2019. doi: 10.1016/j.paerosci.2018.06.004.

[3] B. Lukasik and W. Wisniowski. All-electric propulsion for future business jet aircraft: A feasibility study. *Proceedings of the Institution of Mechanical Engineers, Part G: Journal of Aerospace Engineering*, 231(12):2203–2213, 2017. doi: 10.1177/0954410017727027. URL https://doi.org/10.1177/0954410017727027.

[4] H. Policarpo, F. Afonso, A. Suleman, and F. Lau. Projecto de vrp. Technical report, Flexcraft Consortium, 09 2018. PROJECTO No 17805.

[5] N. J.Chambers. *Modeling flight : the role of dynamically scaled free-flight models in support of NASA's aerospace programs*. U.S Government Printing Office, 07 2016.

[6] Airbus. Albatrossone, 2019. URL https://www.airbus.com/innovation/future-concepts/biomimicry/albatrossone.html. Last accessed: 2021-05-10.

[7] L. Martin. Lockheed martin x-56, 2013. URL https://www.lockheedmartin.com/en-us/products/X-56A.html. Last accessed:2021-05-10.

[8] SETsa. Flexcraft - modular, stol, flexível, 2019. URL http://flexcraft.pt/en/consortium_en/. Last accessed:2020-11-29.

[9] R. Reis, M. Quintiães, and M. Rodrigues. Estudos preliminares - contexto de operação, mercado e certificação. Technical report, Flexcraft Consortium, 04 2017. PROJECTO No 17805.

[10] J. Vale, F. Afonso, A. Suleman, and F. Lau. Estudos preliminares - estudo de configuração de aeronaves. Technical report, Flexcraft Consortium, 04 2017. PROJECTO No 17805.

[11] J. Vale, F. Afonso, A. Suleman, and F. Lau. Estudos preliminares - estudo aprofundado de materiais, processos de produção e estruturas primárias para o conceito de projeto utility. Technical report, Flexcraft Consortium, 04 2017. PROJECTO No 17805.

[12] R. Reis, M. Quintiães, M. Rodrigues, P. Albuquerque, L. Fartaria, F. Lau, F. Afonso, and J. Vale. Especificações técnicas - especificação de missão, utilizadores e mercado; especificações da configuracão do conceito de produto; perfis de missão, personas e mercado; configuração do conceito de produto. Technical report, Flexcraft Consortium, 09 2017. PROJECTO No 17805.

[13] J. Ornelas. Github repository for the code developed for this master thesis, 2020. URL `https://github.com/jgreenist/Tese_flexcraft`. Last accessed:2021-05-31.

[14] B. Etkin and L. D. Reid. *Dynamics of Flight - Stability and Control*. John Wiley and Sons, Inc., 07 1996.

[15] R. V. Mises. *Theory of Flight*. General Publishing Company, 1959. ISBN: 0-930403-51-7.

[16] B. L. Stevens and F. L. Lewis. *Aircraft Control and Simulation (2nd ed.)*. John Wiley and Sons, Inc., 07 2003.

[17] J. D. Anderson. *Introduction to flight (4th ed.)*. New York, NY: McGraw-Hill., 07 1999.

[18] A. Deperrois. About xflr5 calculations and experimental measurements, 2009. URL `http://www.xflr5.tech/docs/Results_vs_Prediction.pdf`. Last accessed:2021-02-19.

[19] A. Deperrois. Modal analysis and experimental validation, 2011. URL `http://www.xflr5.tech/docs/XFLR5_Mode_Measurements.pdf`. Last accessed:2021-02-19.

[20] D. P. Raymer. *Aircraft Design: A Conceptual Approach*. Education Series, 2004. ISBN: 0-930403-51-7.

[21] MATLAB. trim. URL `https://www.mathworks.com/help/simulink/slref/trim.html`. Last accessed:2021-07-5.

[22] A. A. Lambregts. *Vertical flight path and speed control autopilot design using total energy principles.* 1983.

[23] J. D. S. Park and J. P. How. A new nonlinear guidance logic for trajectory tracking. In *In AIAA guidance, navigation, and control conference and exhibit*, pages 16–19, 2004.

[24] J. R. Azinheira. Folhas da cadeira de controlo de voo, 2016.

[25] L. Eusébio. Projeto e manufatura de uma aeronave elétrica e modular não tripulada. Master's thesis, Universidade de Lisboa, 2019.

[26] drotek ELECTRONICS. Digital differential airspeed sensor kit. URL `https://store-drotek.com/793-1032-digital-differential-airspeed-sensor-kit-.html#/162-sensor-without_pitot_kit`. Last accessed:2021-05-31.

[27] A. D. Team. Here+ rtk gps. URL `https://ardupilot.org/copter/docs/common-here-plus-gps.html`. Last accessed:2021-05-31.

[28] Maxbotix. Ultrasonic range finder - xl maxbotix ez4. URL https://www.ptrobotics.com/sensor-ultrasom/1078-ultrasonic-range-finder-xl-maxbotix-ez4.html. Last accessed:2021-05-31.

[29] F. Lau, F. Afonso, A. Suleman, S. Rodrigues, J. Ornelas, P. Pinto, and H. Policarpo. Testes e validação. Technical report, Flexcraft Consortium, 04 2020. PROJECTO No 17805.

[30] C. M. M. V. F. L. de Silva Bussamra and J. C. Santos. Experimental determination of unmanned aircraft inertial properties. In *ITA – Instituto Tecnológico de Aeronáutica - 2009 Brazilian Symposium on Aerospace Eng. and Applications*, 2009.

[31] M. M. P. An accurate method of measuring the moments of inertia. Technical report, Langley Memorial Aeronautical Laboratory, 10 1930. No. 351.

[32] Y. M. Changle Xiang, Xiaoliang Wang and B. Xu. Practical modelling and comprehensive system identification of a bldc motor. *Mathematical Problems in Engineering*, 2015, 2015.

Appendix A

Model Parameters Measurements and Summary

A.1 Center of Mass Determination Data and Results

Table A.1: Data from loads cells to determine the center of mass in the XY plane (F-02 without fuselage).

#	Force at A (N)	Force at B (N)	Force at C (N)	Force at D (N)	AB (m)	AC (m)	CD (m)	X_{ref} (m)	Y_{ref} (m)	X_{CM} (m)	Y_{CM} (m)	m (kg)
1	26.538	25.676	4.743	5.733	0.512	0.553	0.517	0.001	-0.256	0.0924	0.2565	6.397
2	26.186	25.784	4.645	6.076	0.512	0.553	0.517	0.001	-0.256	0.0946	0.2602	6.397
3	26.509	25.656	4.743	5.811	0.512	0.553	0.517	0.001	-0.256	0.0931	0.2569	6.400
4	24.549	24.059	14.337	-	0.512	0.324	-	0.015	0	0.0738	-0.0019	6.423
5	23.108	23.295	16.5914	-	0.512	0.324	-	0.015	0	0.0798	0.0007	6.428

Table A.2: Data from loads cells to determine the center of mass in the XY plane (F-02 with fuselage).

#	Force at A (N)	Force at B (N)	Force at C (N)	Force at D (N)	AB (m)	AC (m)	CD (m)	X_{ref} (m)	Y_{ref}$ (m)	X'_{CM} (m)	Y'_{CM} (m)	m (kg)
1	31.772	29.341	4.714	67.99	0.512	0.553	0.517	0.001	-0.256	0.0924	0.257	7.431
2	31.713	29.655	4.518	6.879	0.512	0.553	0.517	0.001	-0.256	0.946	0.260	7.425
3	31.291	29.743	4.714	6.899	0.512	0.553	0.517	0.001	-0.256	0.0931	0.257	7.413
4	27.881	28.361	16.768	-	0.512	0.324	-	0.18	0	0.0737	-0.0019	7.450
5	28.518	28.312	16.248	-	0.512	0.324	-	0.15	0	0.0798	0.0008	7.457

Table A.3: Data from loads cells to determine the center of mass in the YZ plane (F-02 without fuselage).

#	Force at A (N)	Force at B (N)	Force at C (N)	Force at D (N)	AB (m)	AC (m)	CD (m)	Z_{ref} (m)	Z'_{CM} (m)
1	30.899	30.341	0.304	0.441	0.946	0.215	0.512	0	0.0026
2	30.596	30.831	0.441	0.317	0.946	0.215	0.512	0	0.0025

Table A.4: Data from loads cells to determine the center of mass in the YZ plane (F-02 with fuselage).

#	Force at A (N)	Force at B (N)	Force at C (N)	Force at D (N)	AB (m)	AC (m)	CD (m)	Z_{ref} (m)	Z'_{CM} (m)
1	33.643	34.035	2.136	3.316	0.946	0.215	0.512	0	0.0155
2	33.957	33.643	3.214	2.009	0.946	0.215	0.512	0	0.0154

A.2 Inertia experimental estimation data

Table A.5: Setup and results for inertia determination of metal bar.

		W[kg]	A[m]	L[m]	z_{struct}[m]	z_{model}[m]	z[m]	$I[kgm^3]$	$I_{theoretical}[kgm^3]$	Error
	Pitch	1.497	-	-	0.4420	-	0.4420	0.2657	-	-
Structure	Roll	1.497	-	-	0.4420	-	0.4420	0.2657	-	-
	Yaw	1.479	0.4030	0.4070	-	-	-	0.0699	-	-
Structure	Pitch		-	-	0.4420	0.4645	0.4485	0.4522	-	-
+	Roll		-	-	0.4420	0.4645	0.4485	0.4027	-	-
metal bar	Yaw		0.4030	0.4070	-	-	-	0.1149	-	-
	Pitch		-	-	0.4420	0.4645	0.4485	0.0542	0.0511	6.079 %
metal bar	Roll		-	-	0.4420	0.4645	0.4485	0.0051	0.00002993	22315%
	Yaw		0.4030	0.4070	-	-	-	0.0450	0.0511	12.028 %

Table A.6: Setup and results for inertia determination of wood bar.

		W[kg]	A[m]	L[m]	z_{struct}[m]	z_{model}[m]	z[m]	$I[kgm^3]$	$I_{theoretical}[kgm^3]$	Error
	Pitch	1.497	-	-	0.4420	-	0.4420	0.2657	-	-
Structure	Roll	1.497	-	-	0.4420	-	0.4420	0.2657	-	-
	Yaw	1.479	0.4030	0.4070	-	-	-	0.0699	-	-
Structure	Pitch		-	-	0.4420	0.4645	0.4485	0.4522	-	-
+	Rol		-	-	0.4420	0.4645	0.4485	0.4027	-	-
wood bar	Yaw		0.4030	0.4070	-	-	-	0.1149	-	-
	Pitch		-	-	0.4420	0.4645	0.4485	0.3483	0.3742	6.899 %
wood bar	Roll		-	-	0.4420	0.4645	0.4485	0.0122	0.0024	606 %
	Yaw		0.4030	0.4070	-	-	-	0.3525	0.3742	5.794 %

Table A.7: Data to determine the moment of inertia I_{yy}.

Pitch motion	Structure		Structure+Wood bar		Structure+Metal bar		Structure + F-02 without fuselage		Structure + F-02 with fuselage	
# of Oscillations	Time[s]	Period[s]	Time[s]	Period[s]	Time[s]	Period[s]	Time[s]	Period[s]	Time[s]	Period[s]
10	13.30	1.33	16.07	1.61	13.84	1.38	14.85	1.49	15.24	1.52
10	13.24	1.32	16.09	1.61	13.92	1.39	14.60	1.46	15.06	1.51
10	13.21	1.32	15.98	1.60	13.96	1.40	14.85	1.48	15.04	1.50
15	19.86	1.32	24.12	1.61	20.76	1.38	22.25	1.48	22.63	1.51
15	19.91	1.33	23.94	1.59	20.83	1.39	22.12	1.47	22.71	1.51
15	19.79	1.32	23.91	1.59	20.77	1.38	22.34	1.49	22.82	1.52
20	26.28	1.31	31.99	1.60	27.72	1.39	29.81	1.49	30.36	1.52
20	26.44	1.32	31.88	1.59	27.66	1.38	29.71	1.49	30.42	1.52
20	26.23	1.31	32.05	1.60	27.62	1.38	29.82	1.49	30.50	1.53
Average	-	1.32	-	1.60	-	1.39	-	1.48	-	1.52

Table A.8: Data to determine the moment of inertia I_{xx}.

Roll motion	Structure		Structure+Wood bar		Structure+Metal bar		Structure + F-02 without fuselage		Structure + F-02 with fuselage	
# of Oscillations	Time[s]	Period[s]	Time[s]	Period[s]	Time[s]	Period[s]	Time[s]	Period[s]	Time[s]	Period[s]
10	13.30	1.33	13.55	1.36	13.07	1.31	16.81	1.68	16.42	1.64
10	13.24	1.32	13.56	1.36	13.14	1.31	16.53	1.65	16.56	1.66
10	13.21	1.32	13.50	1.35	13.00	1.30	16.73	1.67	16.53	1.65
15	19.86	1.32	20.35	1.36	19.63	1.31	25.13	1.68	24.78	1.65
15	19.91	1.33	20.40	1.36	19.54	1.30	24.86	1.66	25.00	1.67
15	19.79	1.32	20.33	1.36	19.75	1.32	24.97	1.66	24.81	1.65
20	26.28	1.31	27.21	1.36	26.25	1.31	33.53	1.68	33.26	1.66
20	26.44	1.32	27.13	1.36	26.24	1.31	33.43	1.67	33.08	1.65
20	26.23	1.31	27.12	1.36	26.19	1.31	33.27	1.67	32.99	1.65
Average	-	1.32	-	1.36	-	1.31	-	1.67	-	1.65

Table A.9: Data to determine the moment of inertia I'_{xx}

Roll Motion	Structure		Structure + F-02 without fuselage $(+19^\circ)$		Structure + F-02 without fuselage $(+19^\circ)$		Structure + F-02 without fuselage $(+19^\circ)$		Structure + F-02 without fuselage $(+19^\circ)$	
# Oscilations	Time(s)	Period(s)	Time(s)	Period(s)	Time(s)	Period(s)	Time(s)	Period(s)	Time(s)	Period(s)
10	13.09	1.309	16.68	1.668	16.78	1.678	16.55	1.655	16.58	1.658
10	13.28	1.325	16.65	1.665	16.70	1.670	16.43	1.643	16.62	1.662
10	13.26	1.326	16.66	1.666	16.75	1.675	16.46	1.646	16.61	1.661
15	19.70	1.313	25.02	1.668	25.28	1.685	24.79	1.653	24.82	1.655
15	19.69	1.313	25.01	1.667	25.09	1.673	24.85	1.657	24.99	1.666
15	19.76	1.317	24.91	1.660	25.20	1.680	24.84	1.656	24.93	1.662
20	26.27	1.314	33.45	1.673	33.50	1.675	33.02	1.651	33.35	1.668
20	26.38	1.319	33.50	1.675	33.68	1.684	33.06	1.653	33.29	1.665
20	26.40	1.320	33.32	1.666	33.66	1.683	33.09	1.655	33.33	1.666
Average	-	1.317	-	1.668	-	1.678	-	1.652	-	1.662

Table A.10: Data to determine the moment of inertia I_{zz}

Yaw motion	Bifilar Structure		Bifilar Structure + Wood bar		Bifilar Structure + Metal bar		Bifilar Structure + F-02 without fuselage		Bifilar Structure + F-02 with fuselage	
# of Oscillations	Time[s]	Period[s]	Time[s]	Period[s]	Time[s]	Period[s]	Time[s]	Period[s]	Time[s]	Period[s]
10	13.75	1.38	20.03	2.00	14.53	1.45	24.38	2.44	23.01	2.30
10	13.74	1.37	20.02	2.00	14.84	1.48	24.11	2.41	23.05	2.31
10	13.82	1.38	19.93	1.99	14.67	1.46	24.28	2.43	22.99	2.30
15	20.58	1.37	30.02	2.00	22.01	1.47	36.09	2.40	34.58	2.31
15	20.51	1.37	30.01	2.00	22.18	1.48	36.11	2.41	34.35	2.29
15	20.52	1.37	29.87	1.99	22.14	1.48	36.36	2.42	34.87	2.33
20	27.49	1.37	39.82	1.99	29.63	1.48	48.24	2.41	46.11	2.31
20	27.44	1.37	39.83	1.99	29.55	1.48	48.47	2.42	46.21	2.31
20	27.40	1.37	39.99	2.00	29.42	1.47	48.28	2.41	46.24	2.31
Average	-	1.37	-	2.00	-	1.47	-	2.42	-	2.31

A.3 Propulsion Data and Results

Table A.11: Rotor Static Thrust Response measured of the propeller 13x8.

Thrust(kgf) 13x8	Incoming Airflow Velocity (m/s)						
PWM(μs)	0.00	6.60	10.01	15.02	20.00	25.02	30.10
1000	0	-0.06787	-0.1013	-0.1373	-0.1886	-0.2288	-0.2828
1100	0.15296	0.086007	0.027432	-0.038081	-0.10351	-0.16205	-0.23056
1189	0.37428	0.23988	0.15613	0.061122	-0.01841	-0.095267	-0.17832
1278	0.6077	0.40637	0.29824	0.18314	0.075412	-0.025235	-0.12134
1367	0.82388	0.59912	0.47314	0.32205	0.18519	0.055236	-0.055823
1456	1.0397	0.81368	0.65854	0.47105	0.30247	0.14637	0.016291
1544	1.2246	0.99442	0.82783	0.61385	0.42985	0.24056	0.080475
1633	1.4419	1.2075	1.0164	0.77999	0.55413	0.33531	0.14939
1722	1.6777	1.4398	1.2493	0.99685	0.73471	0.45371	0.21315
1811	1.898	1.6557	1.4633	1.2002	0.93945	0.64595	0.30588
1900	2.1055	1.8623	1.6535	1.3568	1.0916	0.77754	0.28454

Table A.12: Rotor Static Torque Response measured of the propeller 13x8.

Torque (Nm) 13x8	Incoming Airflow Velocity (m/s)						
PWM(μs)	0.00	6.60	10.01	15.02	20.00	25.02	30.10
1000	0	-0.01252	-0.02107	-0.02426	-0.02697	-0.02436	-0.02429
1100	0.036353	0.03439	0.024656	0.014415	0.0052805	-0.0011942	-0.0068808
1189	0.079641	0.081304	0.070379	0.053093	0.037533	0.021973	0.010532
1278	0.12291	0.12681	0.11519	0.096407	0.076223	0.053532	0.034801
1367	0.16649	0.17122	0.16291	0.14399	0.11919	0.090521	0.061248
1456	0.21149	0.21859	0.20985	0.18935	0.16173	0.12738	0.092174
1544	0.24976	0.25918	0.25197	0.23158	0.20309	0.16358	0.11979
1633	0.29439	0.3057	0.29764	0.2783	0.24347	0.19751	0.14797
1722	0.34327	0.35758	0.35331	0.33623	0.29949	0.23821	0.17395
1811	0.39074	0.40573	0.40382	0.3903	0.3615	0.30294	0.20905
1900	0.43588	0.45238	0.45019	0.43279	0.40421	0.34685	0.19924

Table A.13: Rotor Static Electrical Power Response measured of the propeller 13x8.

Power (Watt) 13x8	Incoming Airflow Velocity (m/s)						
PWM(μs)	0.00	6.60	10.01	15.02	20.00	25.02	30.10
1000	0	0	0	0	0	0	0
1100	21.4672	19.9531	19.2394	16.8646	14.5043	12.2982	10.0494
1189	56.6002	54.4286	51.3402	45.6742	41.2333	34.2203	28.0516
1278	98.2824	95.7419	90.2141	84.109	75.9916	63.9796	51.756
1367	148.214	142.9421	138.8774	130.1416	116.963	100.1281	80.8096
1456	202.9577	198.8391	191.3995	177.9878	161.5161	139.427	113.9781
1544	254.2345	248.2563	240.7791	226.2572	207.9063	178.8974	145.1783
1633	312.0449	310.4816	298.0831	280.7677	253.8412	218.4812	175.7908
1722	382.5936	382.4213	371.6216	353.7039	318.8438	263.9148	204.2415
1811	451.001	452.3811	442.5443	426.6805	396.4776	340.3274	242.85
1900	526.0878	528.9071	514.1841	490.0816	458.9158	396.0695	227.5342

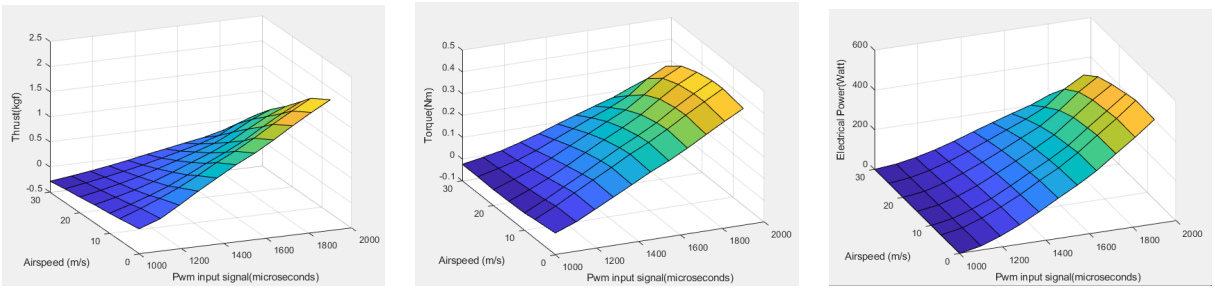

(a) F-01 (b) F-02 (c) F-03

Figure A.1: Rotor Static Response (a) Static Thrust and (b) Static Torque (c) Static Electrical Power measured of the propeller 13x8.

Table A.14: Rotor Static Thrust Response measured of the propeller 12x6.

Thrust(kgf) 12x6	Incoming Airflow Velocity (m/s)						
PWM(μs)	0.00	6.60	10.01	15.02	20.00	25.02	30.10
1000	0	-0.112	-0.1358	-0.2053	-0.2767	-0.356	-0.5068
1100	0.14377	0.047292	-0.0066505	-0.10023	-0.19302	-0.29872	-0.45787
1200	0.36452	0.20574	0.12254	0.004826	-0.10931	-0.24149	-0.40893
1300	0.60126	0.39119	0.27931	0.12348	-0.02941	-0.17312	-0.35318
1400	0.81782	0.59127	0.45402	0.25824	0.071578	-0.11087	-0.29774
1500	1.0455	0.77387	0.62115	0.38621	0.17174	-0.043008	-0.24905
1600	1.1971	0.92622	0.76669	0.51678	0.27745	0.021167	-0.19821
1700	1.3679	1.0794	0.91447	0.64487	0.37882	0.085697	-0.15191
1800	1.6081	1.2996	1.1249	0.82544	0.50215	0.14861	-0.11221
1900	1.8663	1.5416	1.3482	1.0534	0.72712	0.32393	-0.015134
2000	1.9354	1.6158	1.4313	1.129	0.81007	0.39611	0.053074

Table A.15: Rotor Static Torque Response measured of the propeller 12x6.

Torque (Nm) 12x6	Incoming Airflow Velocity (m/s)						
PWM(μs)	0.00	6.60	10.01	15.02	20.00	25.02	30.10
1000	0	-0.01514	-0.01902	-0.02802	-0.02804	-0.02663	-0.03558
1100	0.029741	0.022541	0.01637	0.0043698	-0.0039547	-0.011994	-0.023464
1200	0.067147	0.060225	0.051764	0.036763	0.020136	0.0026445	-0.01135
1300	0.10756	0.10215	0.092162	0.075497	0.049402	0.021003	0.004328
1400	0.14734	0.14319	0.13441	0.11107	0.077611	0.042836	0.01974
1500	0.17468	0.17587	0.16656	0.14114	0.10834	0.064065	0.034778
1600	0.20277	0.20238	0.19406	0.17394	0.13463	0.083723	0.048571
1700	0.23263	0.22639	0.21983	0.19917	0.15825	0.10589	0.061542
1800	0.26654	0.26857	0.26161	0.23625	0.18876	0.12595	0.07447
1900	0.30953	0.31203	0.30531	0.28606	0.2467	0.17609	0.10696
2000	0.32345	0.32594	0.31889	0.30277	0.26689	0.19618	0.12985

Table A.16: Rotor Static Electrical Power Response measured of the propeller 12x6.

Power (Watt) 11x5	Incoming Airflow Velocity (m/s)						
PWM(μs)	0.00	6.60	10.01	15.02	20.00	25.02	30.10
1000	0	0	0	0	0	0	0
1100	22.6933	20.8295	18.8064	15.9084	12.4597	8.9239	5.7635
1200	60.9429	57.1815	52.1774	44.0777	35.1893	25.483	15.5145
1300	104.5623	99.8408	90.7546	78.193	63.132	46.2983	28.4458
1400	148.6219	142.7285	132.0721	115.6129	93.7223	69.2814	42.3959
1500	188.1215	183.4274	170.7331	150.9771	123.5632	91.8748	56.2958
1600	224.3602	219.5726	205.6172	183.2577	151.2756	113.8925	69.1653
1700	256.9814	250.9128	236.5062	213.3493	177.4804	134.473	82.2609
1800	296.8265	290.3743	274.1795	245.3338	202.3336	153.1484	94.3884
1900	363.6486	356.3922	338.7672	311.498	262.8761	194.7182	109.7508
2000	388.4618	380.4692	363.0392	336.4477	290.5349	223.7325	138.9463

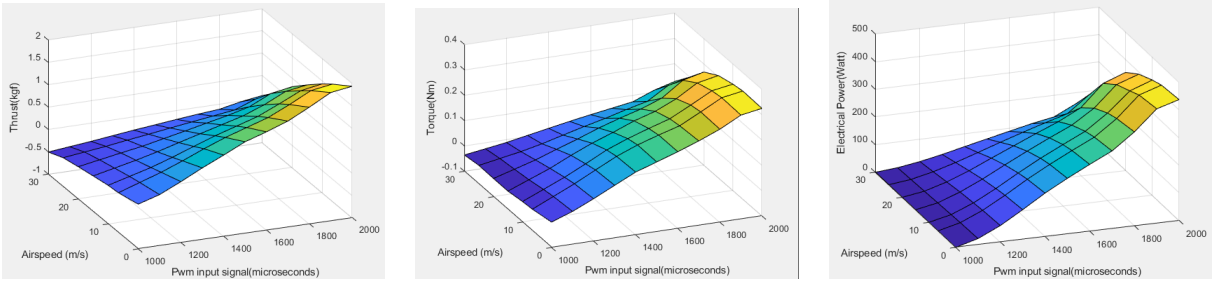

(a) F-01 (b) F-02 (c) F-03

Figure A.2: Rotor Static Response (a) Static Thrust and (b) Static Torque (c) Static Electrical Power measured of the propeller 12x6.

Table A.17: Rotor Static Thrust Response measured of the propeller 11x5.

Thrust(kgf) 11x5	Incoming Airflow Velocity (m/s)						
PWM(μs)	0.00	6.60	10.01	15.02	20.00	25.02	30.10
1000	0	-0.096856	-0.1144	-0.165	-0.2404	-0.2775	-0.3554
1100	0.15287	0.062498	0.015025	-0.063231	-0.14881	-0.21457	-0.32195
1200	0.38504	0.22185	0.14449	0.038574	-0.057247	-0.15159	-0.28849
1300	0.61029	0.40332	0.28865	0.14974	0.019565	-0.099197	-0.2517
1400	0.80105	0.58648	0.45224	0.2667	0.10328	-0.039504	-0.20806
1500	0.96716	0.74845	0.60134	0.38235	0.18679	0.011924	-0.1726
1600	1.1133	0.88861	0.73314	0.49222	0.26422	0.066525	-0.14176
1700	1.2444	1.0104	0.84828	0.5977	0.34518	0.12082	-0.11043
1800	1.4108	1.1642	0.99396	0.71546	0.42244	0.17165	-0.077022
1900	1.656	1.3965	1.216	0.93975	0.61063	0.28461	-0.04048
2000	1.7383	1.4682	1.29	1.017	0.68955	0.35893	0.030738

Table A.18: Rotor Static Torque Response measured of the propeller 11x5.

Torque (Nm) 11x5	Incoming Airflow Velocity (m/s)						
PWM(μs)	0.00	6.60	10.01	15.02	20.00	25.02	30.10
1000	0	-0.01599	-0.01682	-0.02453	-0.02648	-0.02878	-0.0269
1100	0.025146	0.01946	0.015308	0.0030431	-0.0062163	-0.01444	-0.019059
1200	0.059385	0.054913	0.047436	0.030612	0.014044	-9.662e-05	-0.011221
1300	0.092897	0.090611	0.08057	0.06126	0.037805	0.016645	-0.0017115
1400	0.1232	0.12289	0.11221	0.089374	0.0625	0.035514	0.009405
1500	0.14985	0.1484	0.13873	0.11548	0.085192	0.053245	0.020232
1600	0.16964	0.17199	0.16205	0.139	0.10565	0.06974	0.030621
1700	0.19125	0.19371	0.18242	0.16201	0.12573	0.085459	0.040641
1800	0.21779	0.22043	0.2084	0.18528	0.14483	0.099983	0.048805
1900	0.25715	0.26035	0.24896	0.23043	0.18819	0.13023	0.059862
2000	0.26981	0.27246	0.26323	0.24151	0.20535	0.14888	0.081269

Table A.19: Rotor Static Electrical Power Response measured of the propeller 11x5.

Power (Watt) 11x5	Incoming Airflow Velocity (m/s)						
PWM(μs)	0.00	6.60	10.01	15.02	20.00	25.02	30.10
1000	0	0	0	0	0	0	0
1100	22.1313	20.0545	18.2518	15.412	12.3303	9.4709	6.7257
1200	59.4273	54.891	50.7938	44.853	36.0867	27.5271	19.1067
1300	106.9722	99.312	92.9571	81.6516	66.8212	50.9782	35.0491
1400	157.1241	147.5942	139.2847	123.0206	102.6076	77.5149	53.6574
1500	200.7366	191.336	182.7808	162.9913	137.3079	104.5568	71.6232
1600	241.3037	231.7049	222.2345	201.1657	172.116	130.5251	89.51
1700	280.0788	270.3782	260.5344	237.4416	205.0408	155.16	107.1861
1800	339.2552	327.8012	316.7715	289.1604	245.5444	178.576	121.7168
1900	412.8075	402.9097	386.9902	364.5072	323.6219	238.8878	160.6334
2000	436.3797	429.0224	416.5808	392.3167	353.6916	265.5789	188.9174

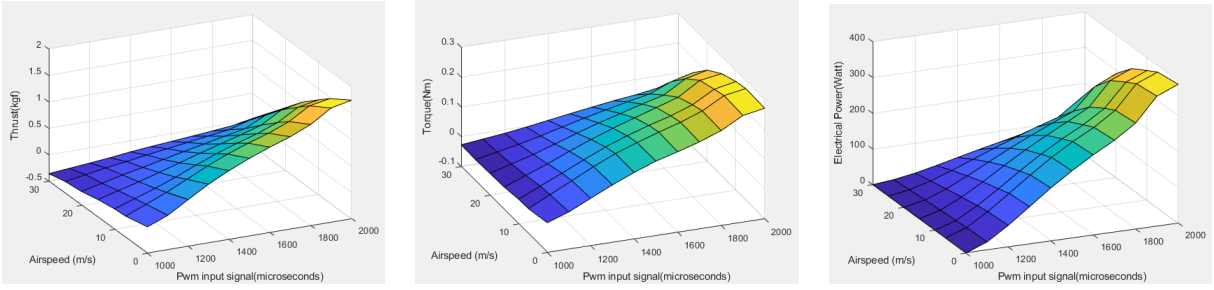

(a) F-01 (b) F-02 (c) F-03

Figure A.3: Rotor Static Response (a) Static Thrust and (b) Static Torque (c) Static Electrical Power measured of the propeller 11x5.